



**NRL Report 9188**

# **Atmospheric Aerosol Size Distributions and Optical Properties Found in the Marine Boundary Layer Over the Atlantic Ocean**

**WILLIAM A. HOPPEL, JAMES W. FITZGERALD,  
GLENDON M. FRICK, AND REGINALD E. LARSON**

*Atmospheric Physics Branch  
Space Science Division*

**EUGENE J. MACK**

*Advance Technology Center  
Arvin Calspan Corporation  
Buffalo, NY*

**June 30, 1989**



REPORT DOCUMENTATION PAGE				Form Approved OMB No. 0704-0188	
1a. REPORT SECURITY CLASSIFICATION <b>UNCLASSIFIED</b>			1b. RESTRICTIVE MARKINGS		
2a. SECURITY CLASSIFICATION AUTHORITY			3. DISTRIBUTION / AVAILABILITY OF REPORT		
2b. DECLASSIFICATION / DOWNGRADING SCHEDULE			Approved for public release; distribution unlimited.		
4. PERFORMING ORGANIZATION REPORT NUMBER(S) <b>NRL Report 9188</b>			5. MONITORING ORGANIZATION REPORT NUMBER(S)		
6a. NAME OF PERFORMING ORGANIZATION <b>Naval Research Laboratory</b>		6b. OFFICE SYMBOL (If applicable) <b>Code 4110</b>		7a. NAME OF MONITORING ORGANIZATION	
6c. ADDRESS (City, State, and ZIP Code) <b>Washington, DC 20375-5000</b>			7b. ADDRESS (City, State, and ZIP Code)		
8a. NAME OF FUNDING / SPONSORING ORGANIZATION <b>Office of Naval Research</b>		8b. OFFICE SYMBOL (If applicable)		9. PROCUREMENT INSTRUMENT IDENTIFICATION NUMBER	
8c. ADDRESS (City, State, and ZIP Code) <b>Arlington, VA 22217</b>			10. SOURCE OF FUNDING NUMBERS		
			PROGRAM ELEMENT NO. <b>61153N</b>	PROJECT NO. <b>RR-033-02-42</b>	WORK UNIT ACCESSION NO. <b>DN480-215</b>
11. TITLE (Include Security Classification) <b>Atmospheric Aerosol Size Distributions and Optical Properties Found in the Marine Boundary Layer Over the Atlantic Ocean</b>					
12. PERSONAL AUTHOR(S) <b>Hoppel, W. A., Fitzgerald, J. W., Frick, G. M., Larson, R. E., and Mack, E. J.</b>					
13a. TYPE OF REPORT <b>Interim</b>		13b. TIME COVERED FROM _____ TO _____		14. DATE OF REPORT (Year, Month, Day) <b>1989 June 30</b>	
15. PAGE COUNT <b>81</b>					
16. SUPPLEMENTARY NOTATION					
17. COSATI CODES			18. SUBJECT TERMS (Continue on reverse if necessary and identify by block number)		
FIELD	GROUP	SUB-GROUP			
19. ABSTRACT (Continue on reverse if necessary and identify by block number)					
<p>Measurements and analyses of the aerosol size distributions and optical properties found in the marine boundary layer during the 1983 USNS <i>Lynch</i> cruise from Charleston SC to Scotland via Canary Islands are presented. The data given in this report are the most extensive and accurate measurements of the submicron marine aerosol size distribution to date and are supplemented by extensive meteorological observations, balloon soundings, satellite coverage, calculated air mass trajectories, and aerosol chemistry. Eight detailed case studies of the size distribution which occurred under different meteorological conditions are presented and discussed in Sections 3 and 4. The data indicates that repeated cycling of marine boundary layer (MBL) air through nonprecipitating clouds which are usually present at the top of the MBL is a major factor in shaping the size distribution and that new particle formation by heteromolecular, homogeneous nucleation is the most likely mechanism which sustains the concentration of particles found below 0.04 <math>\mu\text{m}</math> radius.</p> <p style="text-align: right;">(Continues)</p>					
20. DISTRIBUTION / AVAILABILITY OF ABSTRACT <input checked="" type="checkbox"/> UNCLASSIFIED/UNLIMITED <input type="checkbox"/> SAME AS RPT. <input type="checkbox"/> DTIC USERS			21. ABSTRACT SECURITY CLASSIFICATION <b>UNCLASSIFIED</b>		
22a. NAME OF RESPONSIBLE INDIVIDUAL <b>G. Frick</b>			22b. TELEPHONE (Include Area Code) <b>(202) 767-3489</b>		22c. OFFICE SYMBOL <b>Code 4110</b>

19. ABSTRACT (Continued)

Calculations of the scattering and extinction coefficients and optical depth of the MBL as a function of wavelength directly from the measured size distribution and MBL vertical structure are compared to measured values of the scattering coefficient and optical depth. These measured and calculated optical properties correlate well throughout the cruise and the results give a relatively consistent picture of the relationship between the aerosol size distribution and E-M properties in the MBL.

## CONTENTS

GLOSSARY .....	v
1. INTRODUCTION .....	1
2. OVERVIEW OF CRUISE .....	2
2.1 Chronological Displays of Selected Data .....	4
2.2 Particle Concentration and Wind Speed Correlations .....	8
3. AEROSOL SIZE DISTRIBUTIONS: CASE STUDIES .....	9
3.1 Transition in the Size Distribution from Continental to Marine .....	9
3.2 Typical Background Distributions Found in the Remote Atlantic .....	12
3.3 Periods of Meteorological Transitions .....	13
3.4 Approach to the Canary Islands .....	18
3.5 Air Advecting Off the Iberian Peninsula .....	21
4. DISCUSSION OF MECHANISMS DETERMINING THE SIZE DISTRIBUTION .....	25
4.1 Surface Deposition .....	26
4.2 Coagulation .....	27
4.3 Gas-To-Particle Conversion .....	28
4.3.1 Condensational Growth .....	30
4.3.2 Nonprecipitating Cloud Cycles .....	31
4.4 Loss of Interstitial Particles to Cloud Droplets .....	34
4.5 Cumulative Removal Times .....	35
5. AEROSOL OPTICAL PROPERTIES .....	36
5.1 Aerosol Scattering Coefficient .....	36
5.1.1 Calculations of the Scattering Coefficient from the Particle Size Distribution .....	36
5.1.2 Spatial Variations .....	38
5.1.3 Wavelength Dependence .....	40
5.1.4 Wind Speed Dependence .....	42
5.2 Aerosol Optical Thickness .....	45
5.2.1 Method of Measurement .....	45
5.2.2 Spatial Variation and Wavelength Dependence .....	46
5.2.3 Comparison of Measured and Calculated Optical Thickness .....	49

6. CONCLUSIONS .....	53
7. ACKNOWLEDGMENTS .....	56
8. REFERENCES .....	56
APPENDIX A — Relationship Between the Various Representations of the Size Distribution .....	59
APPENDIX B — Comparison of Measurements with Different Instruments .....	61
APPENDIX C — CCN Supersaturation Spectra .....	69

## **GLOSSARY**

AMU	Atomic Mass Unit
ASAS	Active Scattering Aerosol Spectrometer
CCN	Cloud Condensation Nuclei
DMA	Differential Mobility Analyzer
DMS	Dimethyl Sulfide
EAA	Electrical Aerosol Analyzer
HSS	HSS, Inc.
MBL	Marine Boundary Layer
MRI	Meteorological Research Instruments, Inc.
MSA	Methane Sulfonic Acid
NOAA	National Oceanographic and Atmospheric Administration
PMS	Particle Measuring Systems, Inc.
PMTC	Pacific Missile Test Center
RH	Relative Humidity
TSI	Thermal Systems Inc.





# ATMOSPHERIC AEROSOL SIZE DISTRIBUTION AND OPTICAL PROPERTIES FOUND IN THE MARINE BOUNDARY LAYER OVER THE ATLANTIC OCEAN

## 1. INTRODUCTION

Atmospheric aerosols impact a number of disciplines within the atmospheric sciences: (a) Aerosols are responsible for the extinction of electromagnetic (E-M) radiation propagating through the atmosphere. Thus knowledge of the natural aerosol is of military importance in assessing and predicting atmospheric effects on any command, control, communications or surveillance systems that rely on E-M signals propagating through the atmosphere. Furthermore, aerosols affect the solar radiative transfer and are important in the study and prediction of climate changes. (b) Aerosols provide the nucleation sites on which cloud and fog droplets form and therefore determine the microstructure and optical properties of clouds. The variations in cloud microstructure (such as variations in the concentration and size of cloud droplets for the same liquid water content) are caused by the variations in the precursor aerosol. The geographical and temporal variations in cloud reflectivity and transmission are important factors in climate studies and in evaluating military systems performance. (c) Aerosols are intimately related to atmospheric chemistry. Most of the trace gases injected into the atmosphere by natural and anthropogenic processes pass through the particulate phase before being removed from the atmosphere. Globally, most of the submicron aerosol mass is the result of chemical reactions that convert trace gases to particulate matter within the atmosphere. (d) Remote sensing of the atmosphere using lidar depends on the backscatter signal off aerosols for the return signal. In continental air masses there is usually sufficient aerosol load to produce an adequate signal; however, in clean oceanic environments this may not always be the case.

The large number of submicron particles associated with urban pollution episodes and their relation to public health and welfare has resulted in a significant effort to study urban aerosols. No similar effort has ever been undertaken in the marine environment with the exception of some detailed investigations on the larger sea-salt particles ( $r > 0.5 \mu\text{m}$ ) generated at the sea surface (see for example, Monahan and Mac Niocailli, 1986).

The study reported here has been designed to investigate marine aerosols with emphasis on submicron particles. It is a continuation of the aerosol measurements made at a coastal site along the east coast of the United States (Hoppel et al., 1984) and aboard the USNS *Hayes* in air masses advecting off the east coast of the United States (Hoppel et al., 1983, 1985). These prior measurements that were made primarily in air masses dominated by continental influences have provided excellent data with which to contrast the aerosol found during our more recent cruises in the remote tropical Atlantic and Pacific.

The data presented in this report were taken during a transatlantic cruise aboard the USNS *Lynch* in March and April 1983. The cruise was dedicated to aerosol and marine boundary layer research and involved personnel from several institutions. This report deals primarily with measurements and interpretation of the aerosol size distribution and atmospheric optical properties, including a comparison of measured optical properties with those calculated from the aerosol data. In addition to the NRL data, extensive use is made of the meteorological observations and impactor data taken by

Calspan. Personnel from the Pacific Missile Test Center (PMTC) provided us with balloon soundings of temperature and relative humidity twice daily. These data were indispensable in determining the height of the marine boundary layer and the vertical humidity structure. The National Oceanic and Atmospheric Administration's (NOAA's) air mass trajectory analysis and aerosol chemistry (Parungo et al., 1984) was extremely helpful in interpreting our data. While the results of other participants on the cruise are used, where appropriate, to help interpret and support our data, this report is not intended to present data taken by other investigators.

The data acquired on this cruise have led to several important findings with regard to the role that nonprecipitating clouds play in shaping the size distribution and with regard to the possible source of new submicron particulate material in remote regions. Papers on these subjects have already been published (Hoppel et al., 1986; Hoppel, 1988; Hoppel and Frick, 1988). The pursuit of these investigations has delayed the completion of this report, which gives a more systematic presentation and analysis of the data taken during the 1983 cruise.

## 2. OVERVIEW OF CRUISE

The USNS *Lynch* sailed from Charleston, SC on 11 March 1983, and followed the track shown in Fig. 1, across the tropical North Atlantic to the Canary Islands. After 8 days in port at Las Palmas, the cruise continued on to Scotland and arrived there on 17 April.

The data presented in this report were taken with the instrumentation listed in Table 1.

The three noncommercial instruments listed in Table 1 are the NRL Differential Mobility Analyzer (DMA) (Hoppel et al., 1983), the Calspan Droplet Sampler (Hanley, et al., 1983) and the Radon Monitor (Larson, 1973). Appendix B gives a comparison of the measurements made with different size distribution instruments and a comparison of measurements made with the MRI and HSS nephelometers.

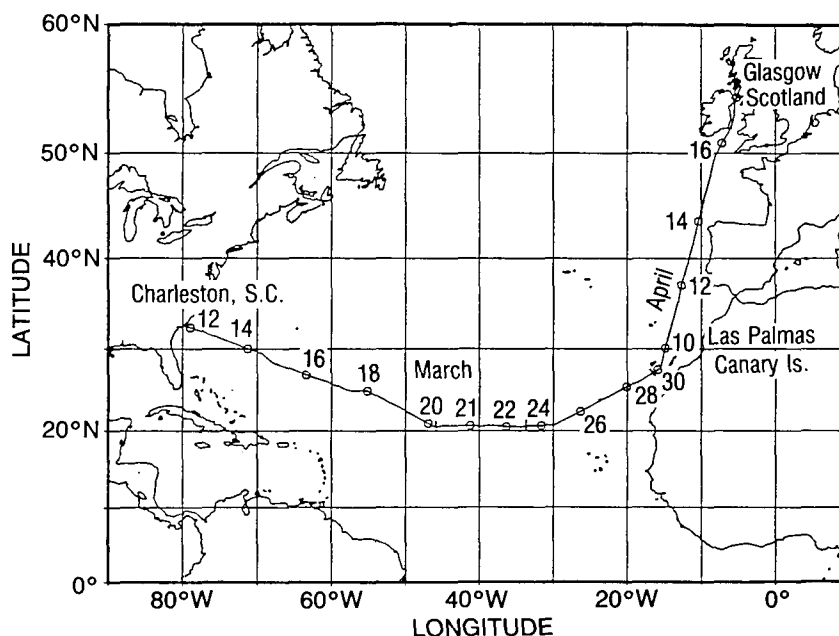


Fig. 1 — Map showing the 1983 Lynch cruise track

Table 1 — Instrumentation and Measured Parameters

Instrument	Parameter
1. NRL Differential Mobility Analyzer	Size Distribution ( $0.006 < r < 0.5 \mu\text{m}$ )
2. Optical Particle Counter (Particle Measuring Systems, Inc.) ASAS-300	Size Distribution ( $0.105 < r < 1.5 \mu\text{m}$ )
3. Calspan Droplet Impactor (gelatin replicator)	Drop Size Distribution ( $0.5 < r < 50 \mu\text{m}$ )
4. MRI Integrating Nephelometer (Wavelength, $0.55 \mu\text{m}$ )	Scattering Coefficient
5. HSS Nephelometer (Wavelength, $0.89 \mu\text{m}$ )	Scattering Coefficient
6. Gardner Particle Counter	Total Aerosol Concentration
7. Foxboro Temperature System (Four Sensors)	Sea Surface and Air Temperature
8. Sling Psychrometer	Wet and Dry Bulb Temperature
9. Automatic Radon Monitor	Atmospheric Radon Concentration
10. Volz Sun Photometer	Solar Intensity
11. Beckmann-Whitley System	Relative Wind Speed and Direction

Also, note that the differential mobility analyzer (DMA) size distributions given in this report were corrected in three respects, and therefore they do not agree exactly with the size distributions in our earlier reports. (a) Subsequent to the cruise, we have measured the diffusion loss in the DMA and charge neutralizer and have made a small correction in our raw data to account for diffusive loss. (b) Recently an extensive study (Hoppel and Frick, 1989) of the nonsymmetric charging characteristics of neutralizers showed that there was a 1.3 ratio of negatively charged particles to positively charged particles for the neutralizer used during this cruise. Since we measure the positively charged particles in our DMA, it means that our raw counts were about 15% below the mean of the positive and negative concentrations. We further corrected our raw counts by this factor. (c) The corrected raw data were then used to recalculate all the size distributions taken on our 1983 cruise. The inversion scheme now uses the charge distribution theory published by Hoppel and Frick (1986) for symmetric charging with 150 atomic mass unit (amu) ions. (The nonsymmetric nature of the charge was accounted for in (b) above.) In our earlier reports, the size distribution had been calculated from the DMA data assuming a Boltzmann charge distribution to determine the charged fractions. This latter correction decreased the number of particles in the smallest several channels and had negligible affect at radii above  $0.02 \mu\text{m}$ . The net effect of these corrections decreases the size distribution for the three smallest DMA channels ( $r = 0.006, 0.009, \text{ and } 0.013 \mu\text{m}$ ) by factors of 3.6, 1.8, and 1.2 respectively. The remaining channels are increased from 4% to 25%.

## 2.1 Chronological Displays of Selected Data

A chronological display of selected data gathered throughout the cruise is shown in Figs. 2 through 6. The ship's location corresponding to a given time can be obtained from Fig. 1. Figures 2 and 3 show the wind speed and direction during the two legs of the cruise. Absolute wind speed and direction were calculated from the ship's velocity, and the relative wind speed and direction were measured at 20 m height with the Beckmann-Whitley wind system mounted on the mast. The temperature and relative humidity, shown in Figs. 4 and 5, were taken hourly on the bow of the ship with a sling psychrometer. Also shown are the sea-surface temperatures taken every 2 h with bucket samples and the temperature at 20 m above the sea surface. Figure 6 shows the radon concentrations and the total aerosol concentration obtained by integrating the measured particle size distributions. Note that the aerosol concentration scale has been changed for the last leg of the cruise to accommodate the large concentrations encountered off the Iberian Coast. Since radon originates over land and decays with a 3.8 day half-life, it is a good indicator of the degree of continental influence remaining with the air mass. Comparisons of the scattering coefficients, as measured with the MRI and HSS nephelometers, and of the total aerosol concentrations obtained by integrating the size distribution and measured directly with a Gardner counter are given in Figs. 30 and 36, respectively. The data in Figs. 2 through 6 are helpful in interpreting the individual episodes discussed later in this report.

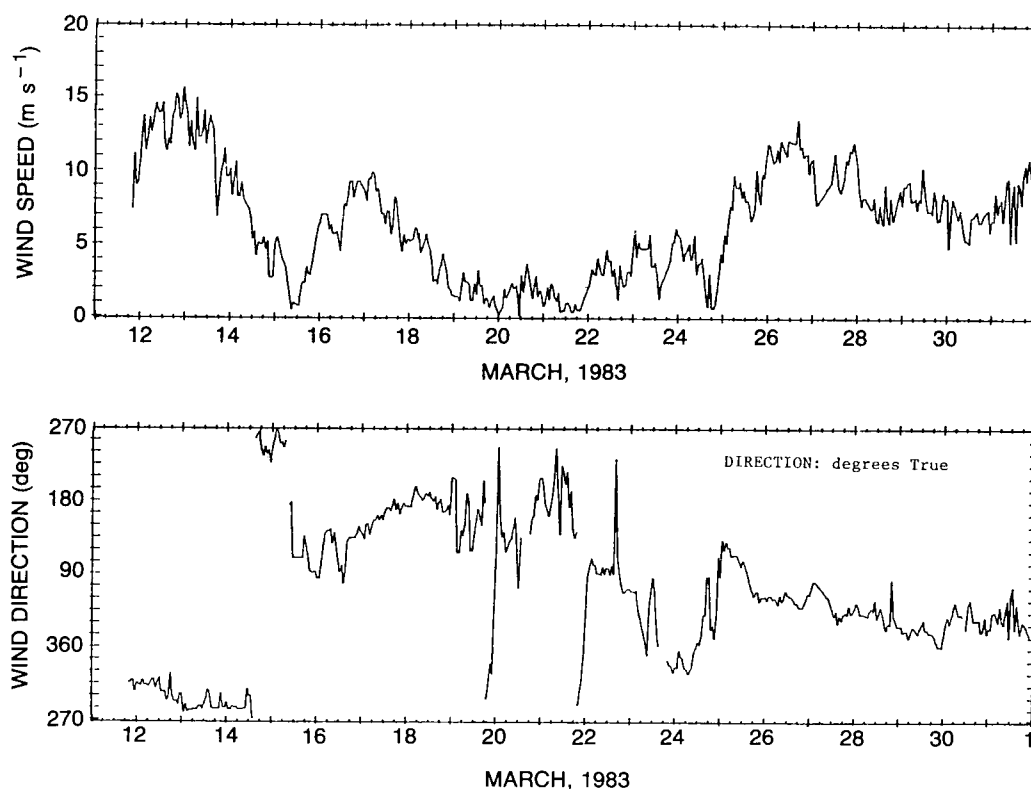


Fig. 2 — Chronological history of wind speed and direction for the Charleston SC to Canary Islands leg of the cruise

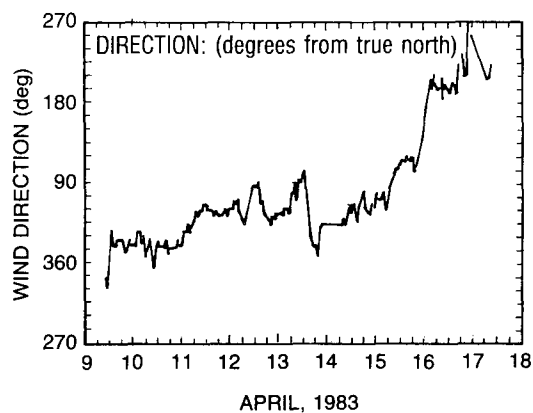
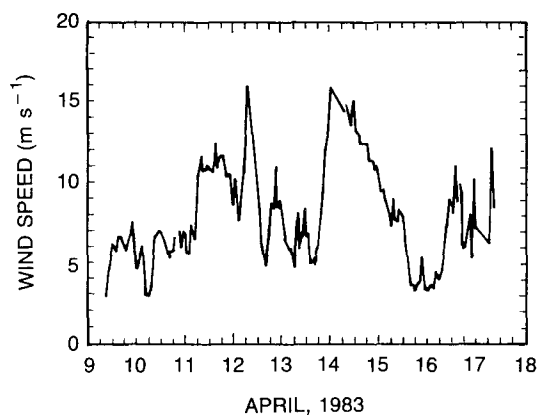


Fig. 3 — Chronological history of wind speed and direction for the Canary Islands to Scotland leg of the cruise

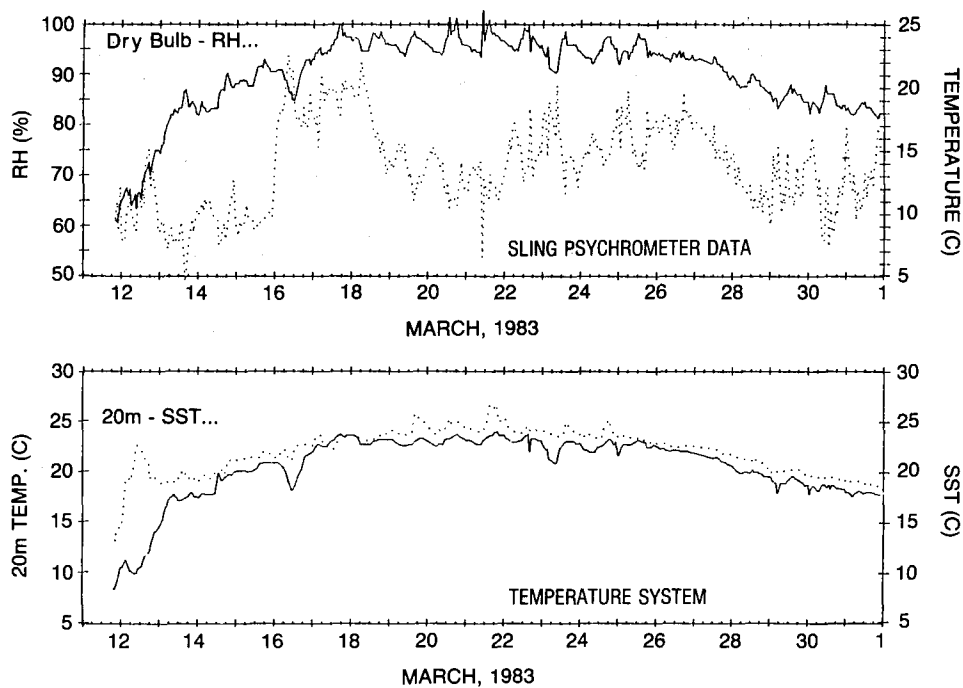


Fig. 4 — Chronological history of air temperature and relative humidity at deck height, the sea-surface temperature, and air temperature at 20 m above for the Charleston SC to Canary Islands leg of the cruise

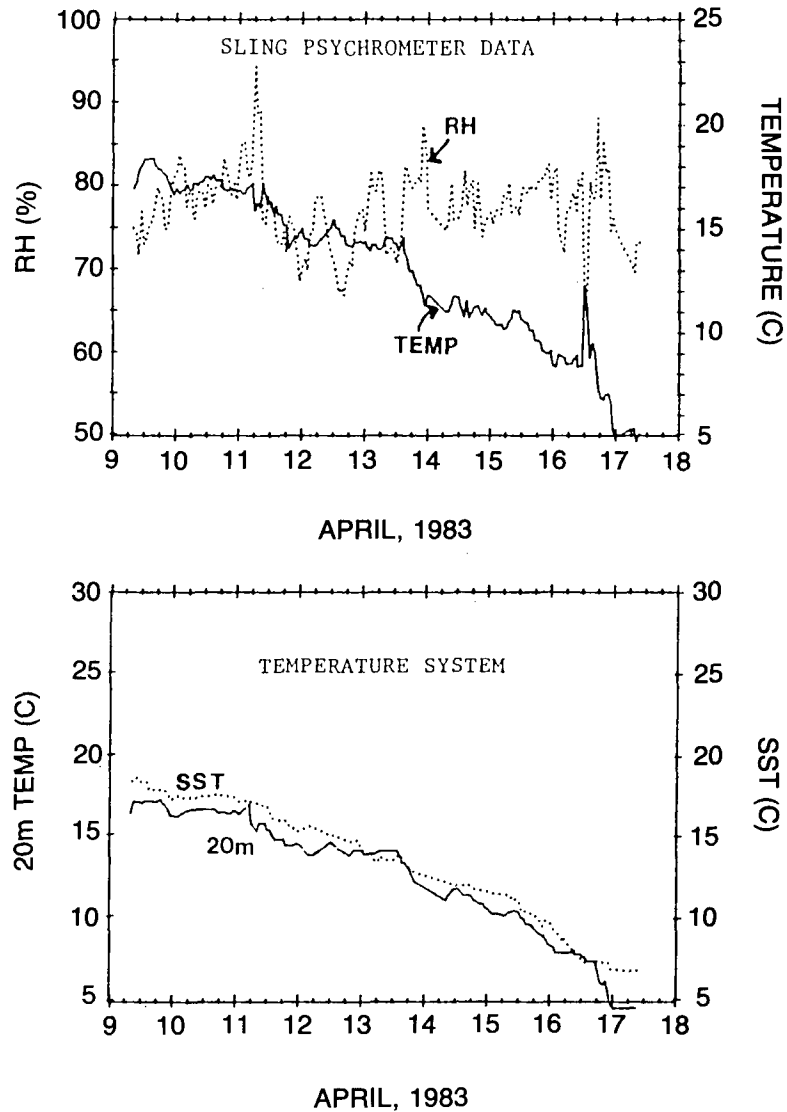


Fig. 5 — Chronological history of air temperature and relative humidity at deck height, the sea-surface temperature, and air temperature at 20 m for the Canary Islands to Scotland leg of the cruise

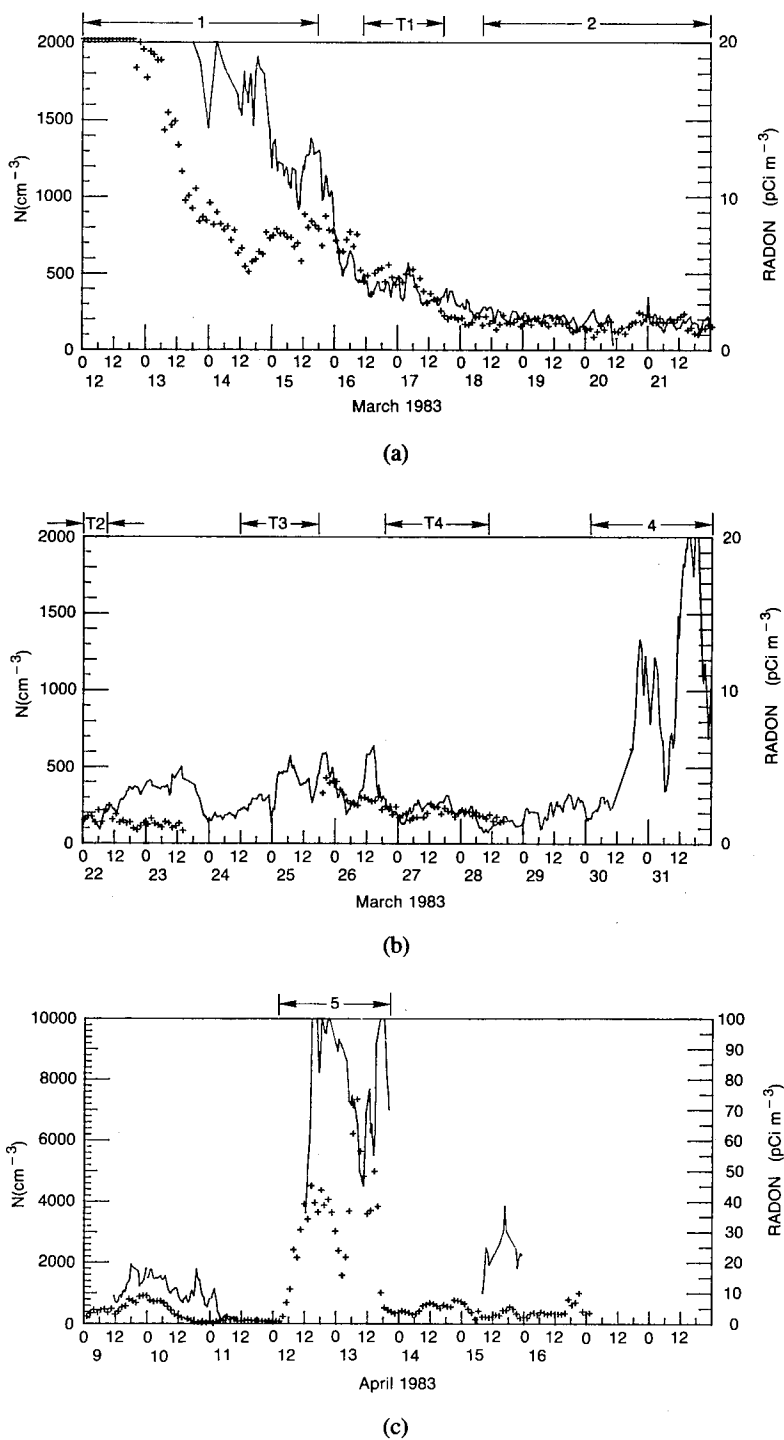


Fig. 6 — Chronological history of total aerosol (solid line) and radon (+) concentrations throughout the cruise

A vast amount of data (including approximately 1600 size distributions) were taken throughout the cruise. In the presentation of aerosol size distributions that follows, we limit the discussion to a number of episodes. The time periods of these episodes are shown at the top of Fig. 6. The first episode shows the evolution of the size distribution from continental to marine during the 4 days that follow the ship's departure from Charleston SC, when the ship was in the area where air advected off the east coast of the United States. The decay in the aerosol and radon concentrations are clearly evident in Fig. 6 as the air ages over the Atlantic. During the second period from 18 to 21 March, the ship was in the area where the air had a long history over the Atlantic, and the size distributions illustrate the characteristics of the background distributions measured over the remote tropical oceans. The episodes labeled T1 to T4 are periods during which changes in the size distributions were associated with known meteorological transitions. Episodes T1 and T3 are episodes when the passage of a meteorological disturbance brought air of African origin to the ship; whereas, episodes T2 and T4 are times when precipitation scavenging is believed to have played an important role in removing particles. Episode 4 is the period of time when the ship approached the Canary Islands under optimum conditions for observing the aerosol plume downwind of the islands against the clean marine background. Episode 5 is the period when the ship traveled along the west coast of the Iberian Peninsula and encountered air advecting directly off the coast. During this period, new particle formation was observed on two occasions.

## 2.2 Particle Concentration and Wind Speed Correlations

Correlation coefficients are a measure of the dependence of two variables upon each other and/or a common independent variable. For the data base of this cruise, variables can be considered relatively independent if the coefficient is less than about 0.3 and related if it is above about 0.5. (For example, see Young (1962) for a discussion of the significance of correlation coefficients.) The upper values in Table 2 give the correlation coefficients computed by using all valid data obtained on the Charleston to the Canary Islands leg of the cruise. The second value was computed after deleting data from the first two days of the cruise, when the air was dominated by continental influence and during episodes of high concentrations of African dust. The second value should be more indicative of the correlation between sea-salt aerosol and wind speed. The instantaneous wind speed as well as the wind speed associated with the air parcel during the previous few days plays a major role in the concentration of particles larger than  $0.5\ \mu\text{m}$  (Gathman, 1983). The wind histories used in Table 2 were determined from the average speed between 12-h segments of surface trajectory data, and independently by estimating winds from weather maps. Similar wind histories were obtained by both methods.

The correlation of particles greater than  $1\ \mu\text{m}$  with wind speed was high for the subset of data that excluded periods when continental air was known to have been present. The much lower correlation found during the cruise as a whole must be the result of substantial continental material found in the large size range when the air mass could be traced to the continents. This is consistent with the chemical analysis of particles throughout the cruise (Mack et al., 1986; and Parungo et al., 1984.)

The concentrations of particles in the largest two channels of the mobility analyzer ( $0.173$  and  $0.53\ \mu\text{m}$ ) were combined, as were the concentrations in the next five smaller channels ( $0.022$  to  $0.173\ \mu\text{m}$ ), and correlated with wind and the total aerosol concentration (Aitken nuclei). Neither the Aitken nuclei nor the mobility analyzer data were expected to correlate with wind, since most particles in this size range are of continental origin or produced in situ by gas-to-particle conversion. The excellent correlation between the mobility analyzer data and Aitken nuclei was expected, since the Aitken nuclei are dominated by small particles measured with the mobility analyzer.

Correlations between the wind speed and extinction are given later on in the report.



Table 2 — Correlation Coefficients Between Wind Speed and Particle Concentrations

	Impactor				Mobility Analyzer		Aitken Nuclei
	.5-1 $\mu$ m	1-2 $\mu$ m	2-5 $\mu$ m	5-9 $\mu$ m	Large	Small	
Wind 0-12 m s <sup>-1</sup>	.179	.346	.498	.507	.125	.094	.125
	.630	.659	.782	.644	.172	.137	.095
Wind 0-24 m s <sup>-1</sup>	.207	.408	.531	.494	.165	.077	
	.674	.736	.809	.666	.092	.126	
Mobility Analyzer (Large) (.173 - .53 $\mu$ m)	.207	.289	.403	.506			.321
	.346	.386	.445	.066			.839
Mobility Analyzer (Small) (.022 - .173 $\mu$ m)	-.037	.002	.063	.256			.884
	.241	.232	.312	.093			.929
Aitken Nuclei	.044	.045	-.065	.066	.321	.884	
	.342	.390	.380	.096	.839	.929	

### 3. AEROSOL SIZE DISTRIBUTIONS: CASE STUDIES

#### 3.1 Transition in the Size Distribution from Continental to Marine

The weather during the first four days of the trip was dominated by a strong low pressure system moving out to sea off the middle-Atlantic states. The night before sailing there were heavy rains and the skies were still overcast with high winds when the ship left Charleston SC and moved out into open seas at about 2100 GMT (1600 EST) on 11 March 1983. The strong counterclockwise circulation around the center of the low resulted in northwest winds of 15 m s<sup>-1</sup>. These were trailing winds, and it was necessary for the ship to turn periodically into the wind for about an hour to obtain air samples that were not contaminated by the ship's own exhaust. The time of this period is indicated as period 1 at the top of Fig. 6.

Curve 1 shown in Fig. 7 is the average of six size distributions taken between 2100 GMT on 11 March and 2200 on 12 March. The total aerosol concentration calculated from Curve 1 is about 5460 cm<sup>-3</sup>. During this period the skies were overcast with stratocumulus, and the radon count dropped from about 50 to 25 pCi m<sup>-3</sup>, thus confirming that 1 to 5 h earlier the air had been over land. Figure 8, Curve 1, shows the corresponding volume distribution, and Fig. 9 shows the back trajectory for this period of time. The volume distribution of particles with radii greater than 0.8  $\mu$ m is that obtained from the Calspan impactor data discussed in Appendix B. Because of the rapid change in the size distribution near the coast and the changing weather conditions, the six size distributions that were averaged to obtain Curve 1 were all significantly different. This is in contrast to the rest of the average size distributions given in this report, where we average only over periods where the size distribution remained nearly stationary over the averaging period. Curve 1 is given primarily to illustrate the larger features of the transition in the size distribution as the air leaves the continent.

Curve 2 is the average of 17 similar size distributions taken between 1100 and 2100 GMT on 14 March, giving a total particle concentration of 1920 cm<sup>-3</sup>. The wind was from the west and had decreased to 3 to 5 m s<sup>-1</sup>. It was no longer necessary for the ship to turn into the wind to obtain a valid sample, so sampling was performed continuously. Skies were nearly clear with only about 10%

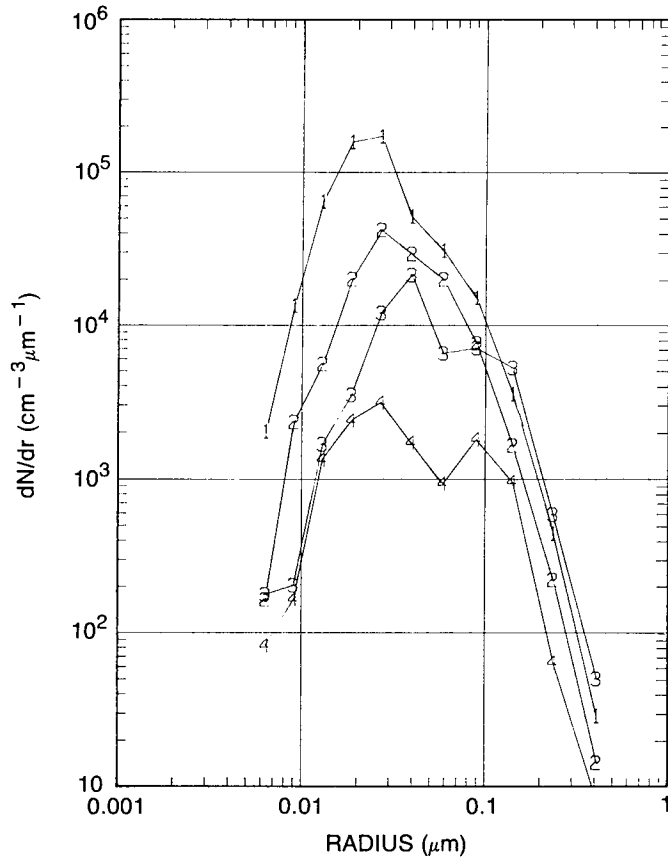
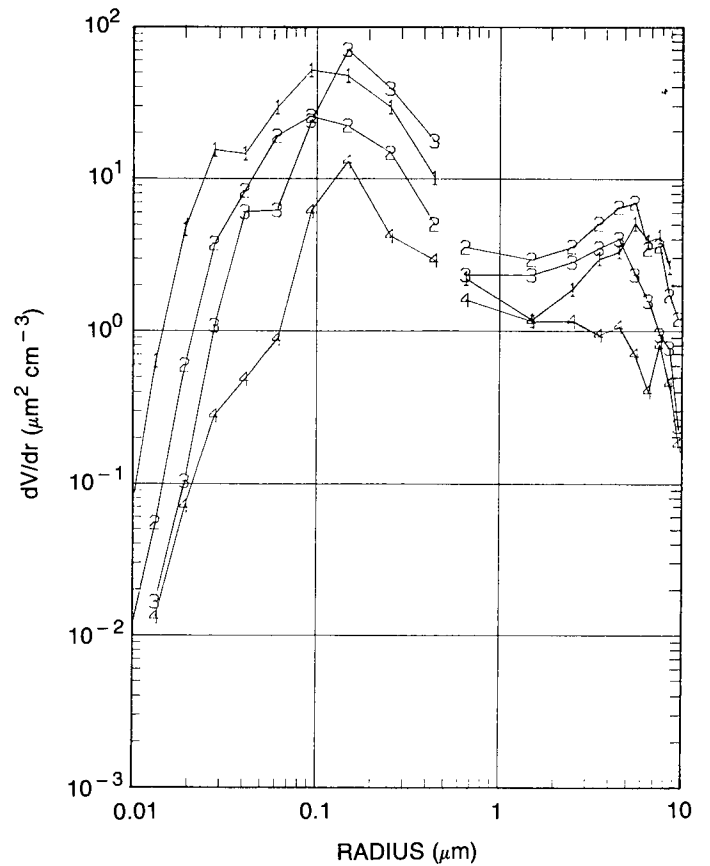


Fig. 7 — Transition in the size distribution from continental to marine. Curve 4 is a size distribution for air with a long history over the Atlantic

Fig. 8 — Volume distribution during the transition from continental to marine corresponding to size distributions shown in Fig. 7



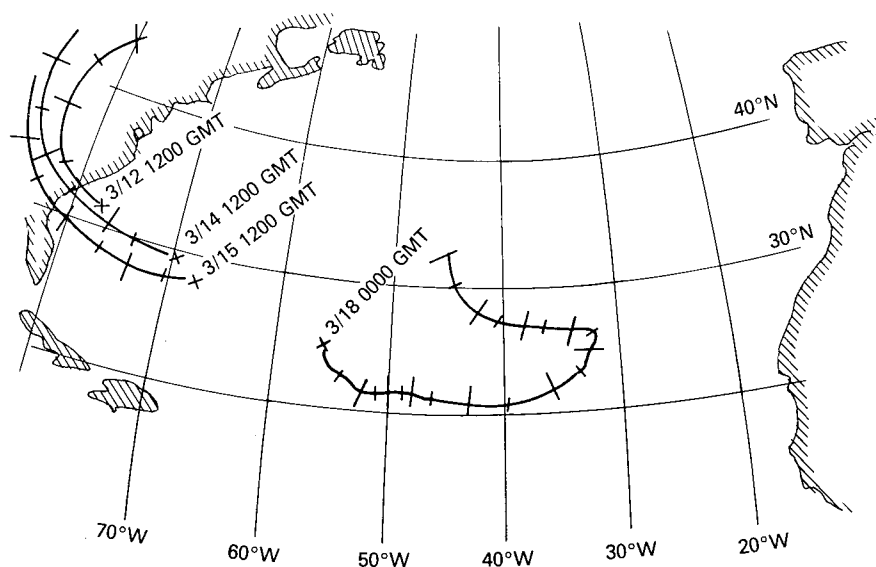


Fig. 9 — Back trajectories for the four size distributions shown in Figs. 7 and 8

cumulus cloud cover. The back trajectory for this period (Fig. 9) shows the air had been over the water for about 18 h. The radon concentration had dropped to  $7 \text{ pCi m}^{-3}$ . Satellite photographs (and air trajectories) indicate that the air came from a very clear area over Tennessee and behind the low pressure system. Balloon soundings showed a strong inversion at about 4500 ft with a maximum relative humidity of only 90% at the inversion. The surface relative humidities were between 50% and 60%, which are very low for the marine surface layer. From all indications the size distributions represented by Curve 2 were taken in a subsident air mass originating over the United States and advecting to the location of the ship along a trajectory free of clouds.

Curve 3 in Fig. 7 is the average of 14 similar size distributions taken on 15 March between 0930 and 1800 GMT. The total concentration is  $1325 \text{ cm}^{-3}$ . The local wind speed was only about  $3 \text{ m s}^{-1}$ , and the direction was variable but from the southern quadrant. The skies during this period were overcast with 80% to 100% alto and stratocumulus cloud coverage. The soundings showed a saturated region between 3800 and 5600 ft; it was capped by an inversion which was rising and broke up later in the day. (The following night there was rain.) Air trajectories (Fig. 9) indicate that the air passed over the Georgia and northern Florida coast 2.5 days earlier. The satellite photos show very little cloud coverage along the trajectory until March 15, when significant cloud coverage was observed by local observations and balloon soundings. The radon concentrations remained at about 7 to  $8 \text{ pCi m}^{-3}$  level during this period.

We believe that the hump at  $0.1 \mu\text{m}$ , which is evident in Curve 3, is associated with the effect of nonprecipitating clouds on the size distribution. This hump did not occur during the time period represented by Curve 2, when the air had traversed a cloud-free region between land and the measurement location. The possible effects of nonprecipitating clouds on the size distribution will be discussed later, but it will be alluded to throughout the presentation of the data as a possible cause for the frequently observed double-peaked distributions.

Figure 8, Curve 3, shows the volume distribution during this time period. The very low winds ( $< 3 \text{ m s}^{-1}$ ) during this period explain the low concentrations of particles greater than  $5 \mu\text{m}$ . The impactor data are used for the volume distribution at radii greater than  $0.8 \mu\text{m}$ ; Curves 2 and 3 are the average of three individual distributions taken during the specified time periods. The total volumes in the DMA size range for Curves 1 to 3 are  $12.0$ ,  $6.0$ , and  $14.5 \times 10^{-6} \text{ cm}^3 \text{ m}^{-3}$  respectively; the corresponding impactor volumes are  $27.5$ ,  $38.7$ , and  $21.0 \times 10^{-6} \text{ cm}^3 \text{ m}^{-3}$ .

### 3.2 Typical Background Distributions Found in the Remote Atlantic

During the night of 15 March and morning of 16 March a front passed over the ship, bringing rain and heavy overcast that lasted during most of March 16. After the passage of the disturbance, the local winds were from the southeast, and lasted several days with speeds generally below  $7 \text{ m s}^{-1}$ ; trajectory analysis in Fig. 9 shows that the air had been over water for many days. The radon concentration dropped to  $2 \text{ pCi m}^{-3}$ , which is the normal Atlantic marine background level. Figure 10 shows the composite of 49 size distributions taken during a 35 h period, from March 18, 0800 until March 19, 1900. The composite is presented to emphasize that all the size distributions during this time period exhibited the double-peaked characteristic. The average total aerosol concentration is about  $243 \text{ particles cm}^{-3}$ . The soundings during this period indicate that the strong inversion that was present on 13 to 15 March had disappeared and there were now multiple but weaker humidity inversions with higher humidities up to 10,000 ft. The cloud cover varied during this period. Throughout the day on 18 March there was about 85% coverage that consisted of cirrus, cumulus, and altostratus. On 19 March, however there was only about 20% cumulus coverage. Also, the double-peaked character of the size distributions appeared more pronounced on 18 March when the cloud cover was greater. The average of the composite is also shown as Curve 4 on Fig. 7 to compare the background marine size distribution with the series showing the transition from continental to marine.

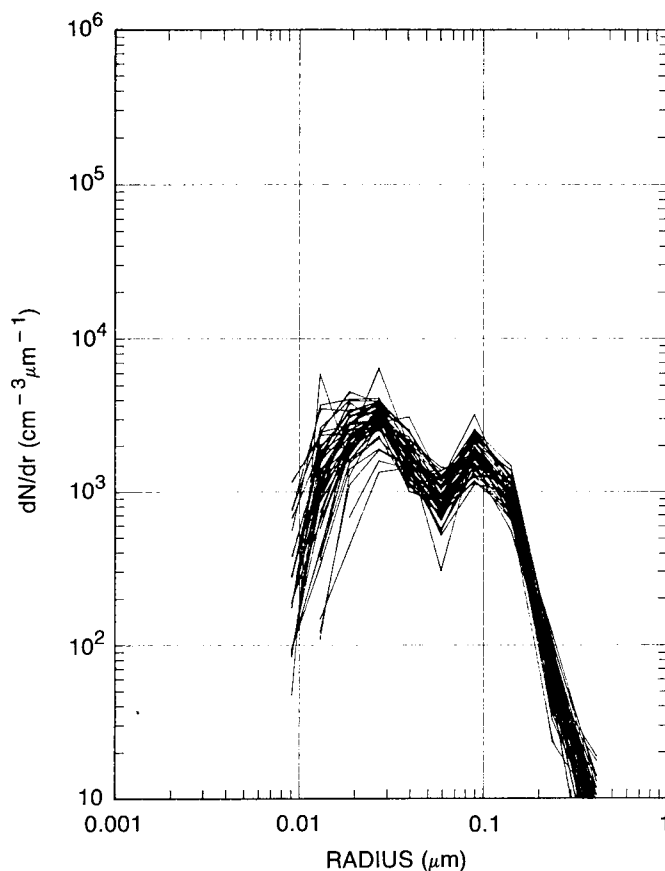


Fig. 10 — Composite of 49 size distributions taken during a 35-h period on March 18 and 19, typical of conditions when there was no continental influence

During the period from 18 to 21 March, the ship was under the influence of a subtropical high. During this period, the lower relative humidity in the marine boundary layer would suggest that drier air from above was subsiding. The size distributions shown in Fig. 10 are quite typical of the submicron size distributions measured during this 4-day period, indicated as period 2 at the top of Fig. 6.

The remote (tropical) Atlantic seems to have some mechanism that sustains the type size distribution shown in Fig. 10. As will be pointed out later, there were occasions when the shape of the size distribution changed, but these changes were associated with synoptic scale meteorological disturbances. After the passage of the disturbance and the return of air with a marine history, the submicron size distribution seemed to always recover its double-peaked characteristic.

Figure 8 (Curve 4) shows the volume distribution where the distribution of the larger particles is the average of four impactor data sets taken during this period. The volume of the particles with radius smaller than  $0.6 \mu\text{m}$  is  $2.27 \times 10^{-6} \text{ cm}^3 \text{ m}^{-3}$ , and the volume of the particles larger than  $0.7 \mu\text{m}$  is about  $8.4 \times 10^{-6} \text{ cm}^3 \text{ m}^{-3}$ .

### 3.3 Periods of Meteorological Transitions

On several occasions there were well defined changes in the meteorological conditions, and often they were accompanied by some precipitation. Since aerosols are removed by precipitation scavenging, data taken before and after rain in the same air mass would be extremely valuable. The rain episodes were usually associated with meteorological disturbances, and it is difficult to determine whether the changes in the size distribution were associated with the rain or a change in the air mass. The change in the size distribution during four transitional periods are discussed here (episodes T1 to T4 at the top of Fig. 6).

Case 1 - Late on 15 March the ship overtook a stagnating weak front. The skies were completely overcast, from 1400 GMT on 15 March until 0900 on 17 March with rain occurring much of the time from 0200 GMT until 1300 on 16 March. This event separated the two periods discussed above and marks the change from air that was influenced by North America to air of marine origin. The trajectories before and after this period (on March 15 and 18) are shown in Fig. 9. On March 17, the midlevel air-mass trajectory indicates that the air came from Africa about 8 days earlier.

Figure 11, Curve 1, shows the average of six size distributions taken between 0022 and 0245 GMT on 16 March before the ship encountered any rain but under overcast conditions, in air that most likely had some remnants of air from North America. Curve 2 shows the average of 14 size distributions taken between 1030 and 1945 GMT on the same day, after the rain (there was some light rain during the early portion of the data). The soundings at 2300 GMT on March 15 showed a saturated region from 2000 to 2700 ft with neutral stability and moisture up to at least 10,000 ft. The wind had shifted from west to southeast, and a large increase in relative humidity occurred late in the day on 15 March. The radon concentrations remained at about  $7 \mu\text{Ci m}^{-3}$  on 15 March but dropped slowly on March 16 and 17, reaching values of about  $2 \mu\text{Ci m}^{-3}$ , typical of pure marine air, by 18 March. The number of particles represented by Curves 1 and 2 are  $747$  and  $464 \text{ cm}^{-3}$  respectively. Curve 2 shows no sign of the double-peaked characteristic. Size distributions similar to Curve 2, but with somewhat less particles at radii less than  $0.03 \mu\text{m}$ , continued throughout the first half of the day on 17 March before slowly transitioning to a double-peaked size distribution (shown by Curve 4 of Fig. 7) on 18 March. The air encountered on 17 March could have originated over Africa, as suggested by Parungo et al. (1984), and/or it had passed over the Lesser Antilles, as suggested by Mack et al. (1986). Evidence of a continental influence is based upon the air mass trajectory calculations and on the chemical analysis of the larger particles, which shows an abundance of silicon and other continentally derived components. We interpret the observed transition in the size distribution to be the result of the changing air mass.

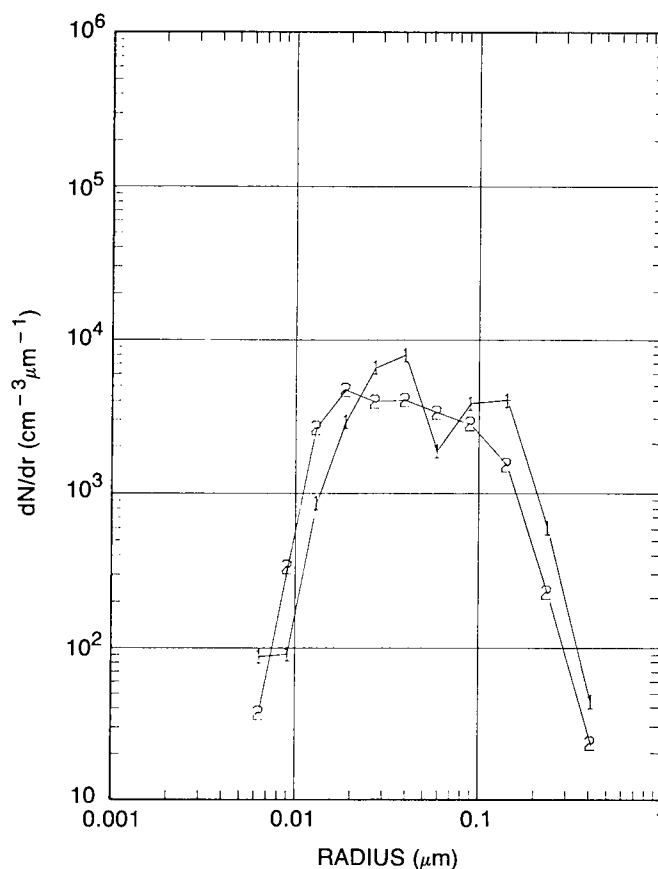


Fig. 11 — Change in the size distribution during transit through weak front with air that had land influence

Case 2 - Early on 22 March, the ship passed through a region of high thunderstorm activity (episode T2 in Fig. 6). The local winds went from southerly at about  $1 \text{ m s}^{-1}$  to easterly at about  $4 \text{ m s}^{-1}$  at the beginning of this period. The cloud cover was about 60% cumulus (Cu) and cumulonimbus (Cb). The weather map showed scant evidence of a front, but a line of Cb was discernible on the satellite photo in the vicinity of the ship. Curve 1 in Fig. 12 shows the average of seven size distributions between 0015 and 0403 GMT on March 22. During the night and early morning, there was frequent lightning in the area and the ship's radar showed regions of heavy precipitation around and north of the ship. After some rain at the location of the ship at about 0530, the size distribution shown by Curve 2 (average of two) was observed. This type size distribution lasted for only 1 h. The total number of particles in the two size distributions are  $186$  and  $96 \text{ cm}^{-3}$  respectively, and they were some of the lowest aerosol concentrations measured during the cruise. We interpret the low concentration in the second size distribution to be the result of precipitation scavenging in local thunderstorms.

Case 3 - During the period between 1200 GMT on 24 March and 1200 on 25 March, the ship passed through a region of a weak trough connected to a weak low north of the ship (episode T3 in Fig. 6). Air trajectories at mid and low levels indicate that the air was over Africa 7 days earlier. The fact that this air originated in the Sahara was reinforced by the detection of silicon (and other elements associated with continental dust) in particles of radius greater than  $2 \text{ μm}$  (Parungo et al., 1984). The radon counter was not functioning from midday on the 23rd until late on 25 March; however, the

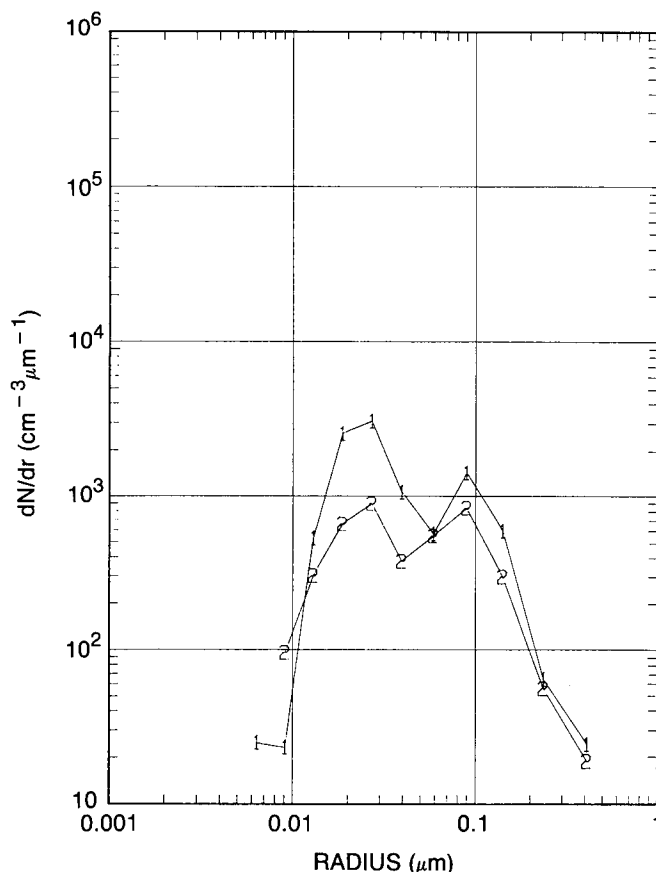


Fig. 12 — Decrease in size distribution caused by precipitation scavenging in local thunderstorms

radon concentration at 2000 on the 25th was about  $4 \text{ pCi m}^{-3}$ , which was more than twice the concentration measured during the period of 18 to 23 March, when the air was known to have a long trajectory over water. During the passage through the trough, the wind direction changed from northerly to easterly, and the wind speed increased from a few meters per second to about  $10 \text{ m s}^{-1}$ . The cloud cover went from clear, early on the 24th, to about 50% Cu and Cb coverage with isolated thunderstorms later in the day, to completely overcast skies with some light rain showers on 25 March. The skies remained overcast through the 26th.

Figures 13 and 14 show the change in the size and volume distributions during this time. Curve 1 is the average of 13 mobility analyzer and one impactor size distributions taken during the period between 0220 and 1000 GMT on 24 March just as the ship was entering the disturbed region. The winds were from the north with nearly clear skies early during the period with the appearance of Cb and distant rain late in the period. Curve 2 is the average of 13 mobility analyzers and one impactor size distribution taken between 1150 and 1930 GMT on 24 March. Again there were Cu and Cb with showers visible in the vicinity of the ship, and a definite change in the size distribution of submicron particles was observed.

Curve 3 is the average of 15 mobility analyzers and one impactor size distributions taken between 0530 and 1500 GMT on 25 March. The skies were overcast, and the wind had increased dramatically to about  $10 \text{ m s}^{-1}$  and was now from the east. Some light rain fell at the ship's location just prior and just after this period, with some light drizzle during the early part of the period. Though there was a significant increase in wind speed, the seas had not yet responded and there was no sea spray and only a few whitecaps. This, and the continentally derived elements found in the analysis of larger particles, indicates that the increase in the concentration of larger particles was due

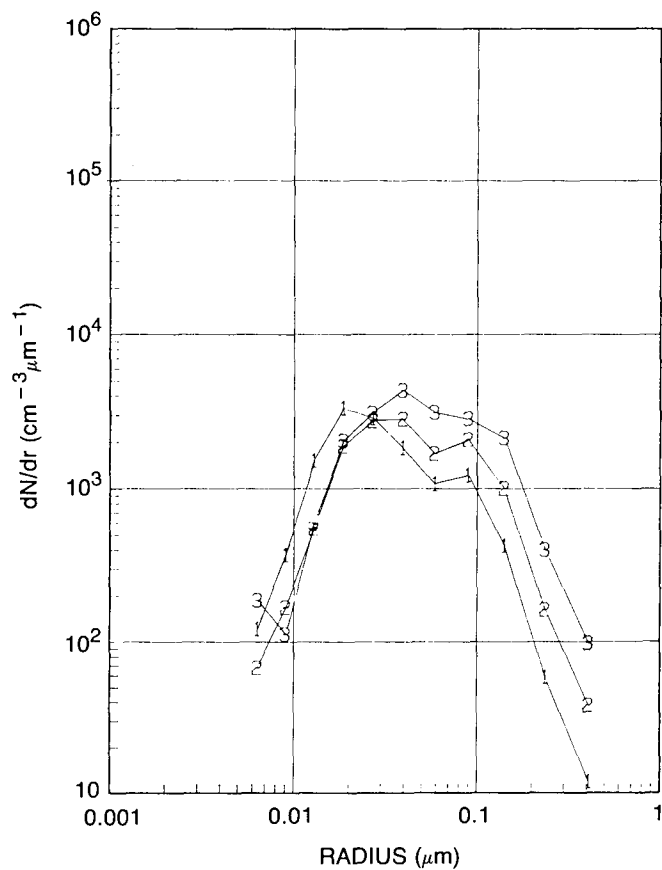
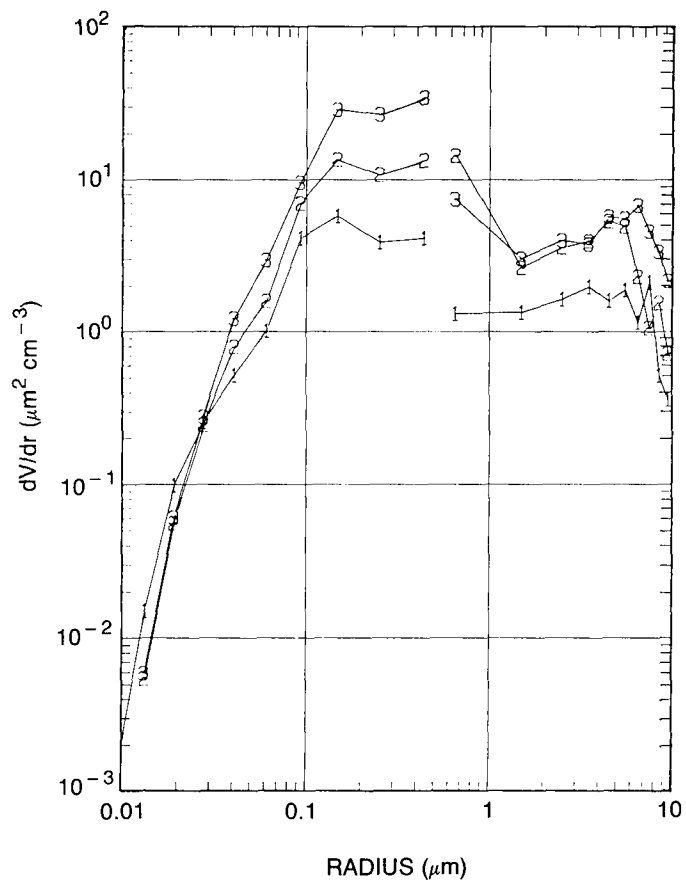


Fig. 13 — Change in the size distribution as the ship encountered a weak trough containing air of African origin

Fig. 14 — Volume distribution corresponding to the size distribution shown in Fig. 13





to the change in the air mass and not to locally generated sea-salt particles. The total concentration of submicron particles in these three size distributions are 196, 299, and  $506 \text{ cm}^{-3}$  respectively. The skies remained overcast, and by 1700 GMT the doubly peaked characteristic returned and was fully restored by 1900 GMT. The total concentration was higher (about  $500 \text{ cm}^{-3}$ ), with a larger peak at  $0.03 \mu\text{m}$ , also the number of large particles remained larger than those observed in Curve 4 of Fig. 7. The size distribution for the following day (26 March), as the air mass trajectory shifted back over the North Atlantic, is shown in Fig. 15, Curve 1.

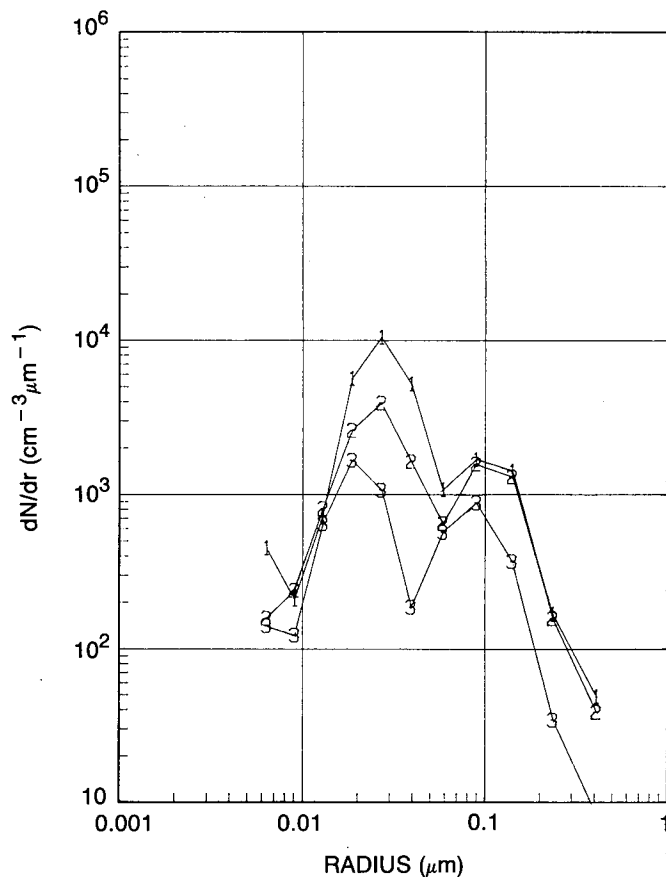


Fig. 15 — Curves 1 and 2 are size distributions taken in air which had passed in front of a cold front and had encountered no (recent) precipitation, whereas the size distribution represented by Curve 3 was taken in air which had passed through the cold front and encountered heavy precipitation three days prior to the measurement

The disappearance of the double-peaked characteristic in Figs. 11 and 13 lasted for only a few hours and occurred in air that was believed to have originated from the Sahara. On both of these occasions there was extensive cloud cover, thus they were exceptions to the more common observation that associated the double peak with the presence of nonprecipitating clouds.

The volume distributions for this period are shown in Fig. 14. The volumes in the submicron size range (mobility analyzer data) for the three curves are  $2.0$ ,  $5.5$ , and  $13.2 \times 10^{-6} \text{ cm}^3 \text{ m}^{-3}$  respectively, and the volumes for the impactor data are  $13.9$ ,  $40.5$ , and  $46.4 \times 10^{-6} \text{ cm}^3 \text{ m}^{-3}$ . There was a large increase in the measured and calculated scattering coefficient during this period as discussed in Section 5.1.2 and is shown in Fig. 30.

Case 4 - Curve 1 of Fig. 15 shows the average of 20 size distributions for the period 0500 to 1630 GMT on 26 March, well after the ship's passage through the area of the trough. The back trajectory indicates that the air came from the North Atlantic, passing near (but not over) the Iberian Peninsula 4 days before arriving at the ship and over (or near) the Canary Islands 2 days before arriving at the ship. Curve 2 is the average of 18 size distributions taken under similar conditions during the period from 1800 GMT on 26 March to 1200 on 27 March. After these 2 days (Curves 1 and 2), there was a significant change in the submicron size distribution to that shown in Curve 3, which is the average of 10 size distributions taken between 0850 and 1310 GMT on March 28. All three size distributions (Curves 1 to 3) occurred under similar local meteorological conditions with mostly overcast skies of stratocumulus and altocumulus with air trajectories that originated in the North Atlantic. The wind speeds were 10 to 15 m s<sup>-1</sup> from the northeast. The soundings for the three periods were similar and were characterized by a 300-m-thick (1000 ft) cloud layer capped by a strong inversion. The height of the inversion rose slowly during the 2 day period, from about 1000 to 1400 m. The total concentrations of submicron particles dropped dramatically, from about 438 to 273 and to 105 cm<sup>-3</sup> for the three curves. There was a significant difference in the weather conditions along the back trajectory of the air for the three periods. On 25 March a strong cold front extended from a low over Europe down across southern Spain and out over the Atlantic and connected to a high pressure ridge over the Atlantic. The back trajectory for Curve 3 was behind this cold front in a region of widespread precipitation 3 days before its arrival at the ship. The trajectories for the periods of Curves 1 and 2 were always in front of the cold front, and the weather maps indicated that the air had not encountered a significant amount of precipitation for at least 5 days before reaching the ship. We therefore believe that the very low concentrations represented by Curve 3 are associated with precipitation scavenging during passage through the cold front 3 days before arriving at the ship. If this interpretation is correct, then it follows that the size distribution had not recovered to the more typical submicron size distribution (such as Curve 2) in the intervening 3 days.

Figure 16 shows the corresponding volume distributions. The integrated submicron volumes for the 3 DMA curves are 6.6, 5.6, and  $1.4 \times 10^{-6}$  cm<sup>3</sup> m<sup>-3</sup> respectively. There was no impactor data taken during the first time period and only one sample each during the second and third periods. The total impactor volumes for Curves 2 and 3 are 46 and  $49 \times 10^{-6}$  cm<sup>3</sup> m<sup>-3</sup> respectively.

### 3.4 Approach to the Canary Islands

One of the most interesting periods of the 1983 cruise occurred when the ship approached the Canary Islands from the southwest, as shown by the dashed line in Fig. 17. Both radon measurements and back-trajectories indicate that the air had been over the ocean for at least 9 days prior to passing over the Canary Islands. Because the air was free of any continental influence, the effect of the islands on the size distribution could be clearly seen. The back-trajectory of the air arriving at the ship is shown in Fig. 17, where the positions of the air 12 and 24 h before are indicated by small and large tic marks on the trajectories. The aerosol plumes downwind of Tenerife (population 400,000) and Grand Canary (population 600,000) are clearly visible, as evidenced by the peaks in the solid curve on the graph at the bottom of Fig. 17. The dotted line gives the cloud cover as observed at the location of the ship. Downwind of Tenerife, the marine inversion was capped with a heavy stratus deck, and complete cloud cover was reported at the Tenerife weather station 12 h earlier. Figure 18 shows balloon soundings of temperature and relative humidity that indicate a stratus layer about 400 m thick with a base near 900 m. A boundary layer model that used the balloon sounding and measured sea-surface temperature data indicated that air from the surface would have mixed upward into the cloud deck in about 2 h, and it would be mixed throughout the boundary layer in about 6 h. This downwind mixing is undoubtedly further enhanced because the islands are mountainous. We therefore can assume that the air from the island had been mixed throughout the cloud and boundary layer before arriving at the ship 12 h later. Figure 17 shows that the increased aerosol concentration

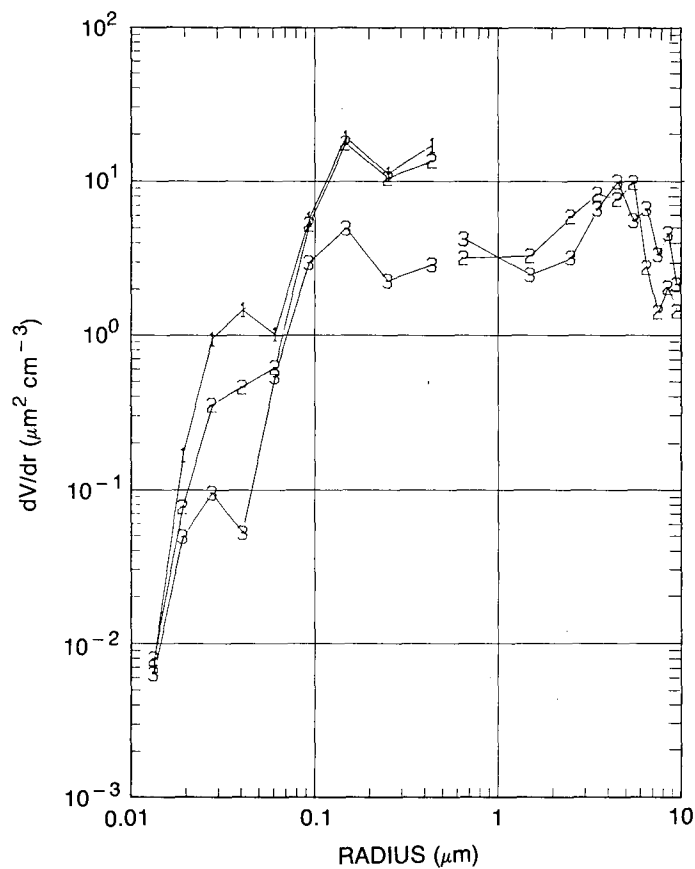
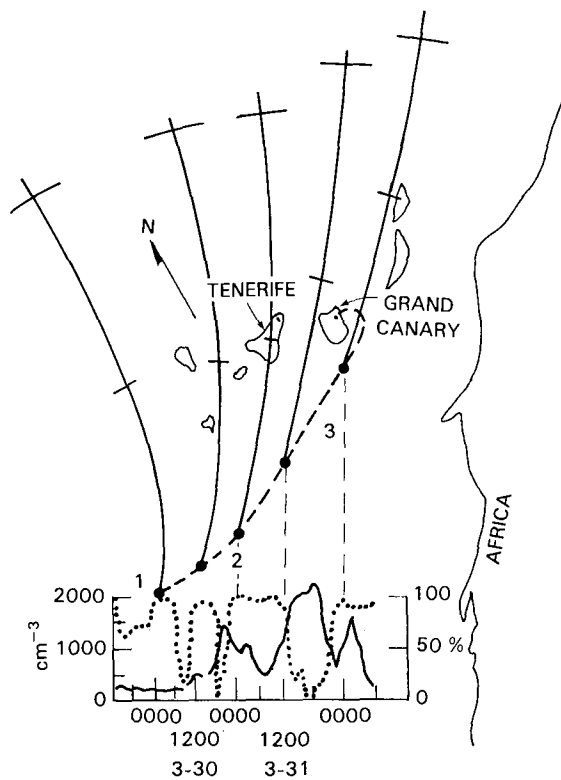
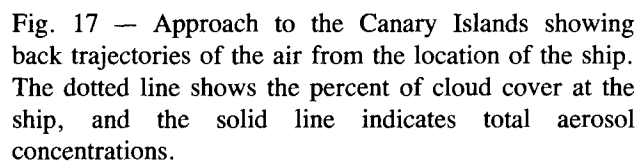


Fig. 16 — Volume distributions corresponding to the size distributions shown in Fig. 15



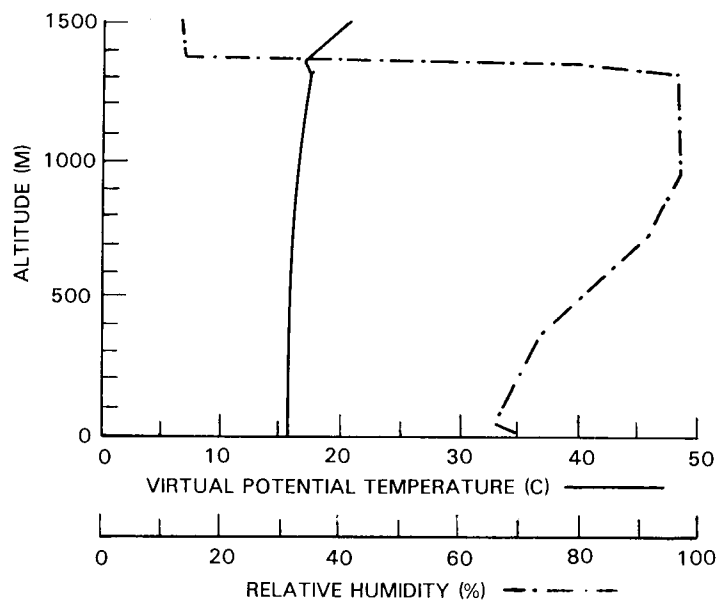


Fig. 18 — Temperature and relative humidity sounding downwind of Tenerife

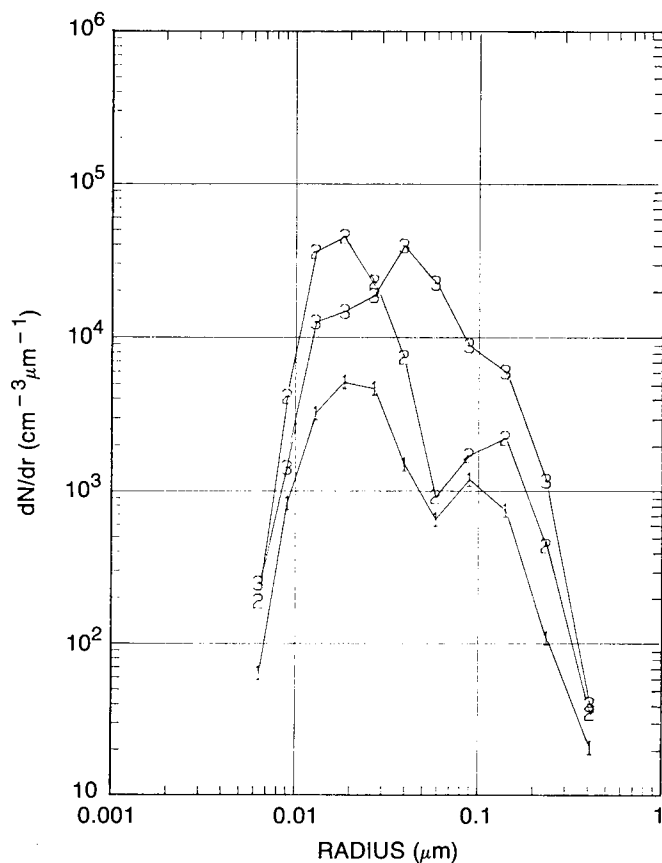


Fig. 19 — Curve 1 is the size distribution before the ship was downwind of the islands. Curve 2 was taken downwind of Tenerife during heavy overcast conditions. Curve 3 was taken downwind of Grand Canary Island under clear conditions.

downwind of Tenerife had a local minimum between two small peaks at 0100 GMT on 31 March. This local minimum was associated with drizzle reported at the ship. About 18 h later, when the ship was downwind of Grand Canary Island, the cloud cover had dissipated, and the observed cloud cover at the ship dropped below 20%, as shown by the dotted line in Fig. 17.

Figure 19 shows the size distributions observed during this period of time at the locations numbered along the ship's track. Curve 1 is the average of 19 distributions taken the night before the island influence was observed. Curve 2 is the average of 11 size distributions taken downwind of Tenerife between 1930 and 0345 GMT on 30 March, omitting a period when drizzle was reported at the ship (the air had traversed a heavy overcast region between the island and the ship). Curve 3 is the average of five distributions taken between 1500 and 1900 GMT downwind of Grand Canary Island in air that had traversed nearly cloudless skies (less than 30% cloud cover). In addition to traversing nearly cloudless skies, there was less time (4 to 8 h) to cycle surface air through the few clouds that did exist. Downwind of Grand Canary the double-peaked feature had disappeared. Downwind of Tenerife where the air was more polluted than in the remote tropical Atlantic, the peak occurred at a larger radius (about  $0.15\ \mu\text{m}$ ). If we assume that the peak at  $0.1\ \mu\text{m}$  is the residue of evaporated cloud droplets, then the larger size indicates a larger accumulation of material in the cloud droplet. The total number of particles in the three size distributions are 248, 1109, and  $2336\ \text{cm}^{-3}$ ; the numbers of particles under the peak at about  $0.1\ \mu\text{m}$  for the first and second curves are about 105 and  $260\ \text{cm}^{-3}$ ; and the total volumes are 3.3, 8.6, and  $19.8 \times 10^{-6}\ \text{cm}^3\ \text{m}^{-3}$  for particles smaller than  $0.6\ \mu\text{m}$ . As the ship moved upwind of Grand Canary, and just prior to arrival at Las Palmas, the distribution was similar to that shown by Curve 1.

### 3.5 Air Advecting Off the Iberian Peninsula

During the transit from the Canary Islands to Scotland the ship passed within 110 km of the Spanish coast. The ship's location as a function of time is shown in Fig. 20. Circulation around a high pressure system north of the ship and off the west coast of Ireland on 11 April produced winds from the northeast at  $10\ \text{m s}^{-1}$  causing high seas. Early on 12 April, there was a squall with winds of about  $16\ \text{m s}^{-1}$ . On 12 April the high moved eastward, and the wind at the ship came increasingly from off the west coast of Portugal. The skies were mostly sunny but hazy, which was caused by high overcast of cirrostratus with some altostratus. As the winds switched more to the east, the fetch to the coast caused the winds and seas to decrease. Size distributions with the mobility analyzer were obtained from about 2000 GMT on 12 April until about 2000 on 13 April. At this time the ship again encountered heavy seas as it emerged from the (wind) shadow of the Spanish coast.

The NOAA trajectory analysis used earlier was not available on this leg of the cruise, so the back trajectories shown on Fig. 20 were constructed from weather maps and local winds at the ship. The tic marks on the trajectories indicate 6-h intervals. It is clear from the trajectories and radon data that there was an increasing influence of land during the morning of the 12 April. The radon increased dramatically from 2 to  $20\ \text{pCi m}^{-3}$  as the air came increasingly from the direction of land. Subsequent variations in the radon concentrations above  $10\ \text{pCi m}^{-3}$  are most likely caused by the variations of the source strength and mixing over land. The hourly condensation nuclei concentrations measured with a Gardner counter and the total aerosol concentrations from the submicron size distributions are also shown along the ship's track. The total concentrations are more than an order of magnitude greater than those found earlier in the remote Atlantic.

A composite of the six size distributions measured at the ship between 0400 and 0700 GMT on 13 April are shown in Fig. 21. This air had been over land about 12-h earlier and had spent most of its 12-h journey from the coast in darkness. These size distributions are very similar to those observed in air masses advecting off the east coast of the United States under similar conditions (Hoppel et al., 1985). The average total concentration of these six size distributions is  $8000\ \text{cm}^{-3}$ . The

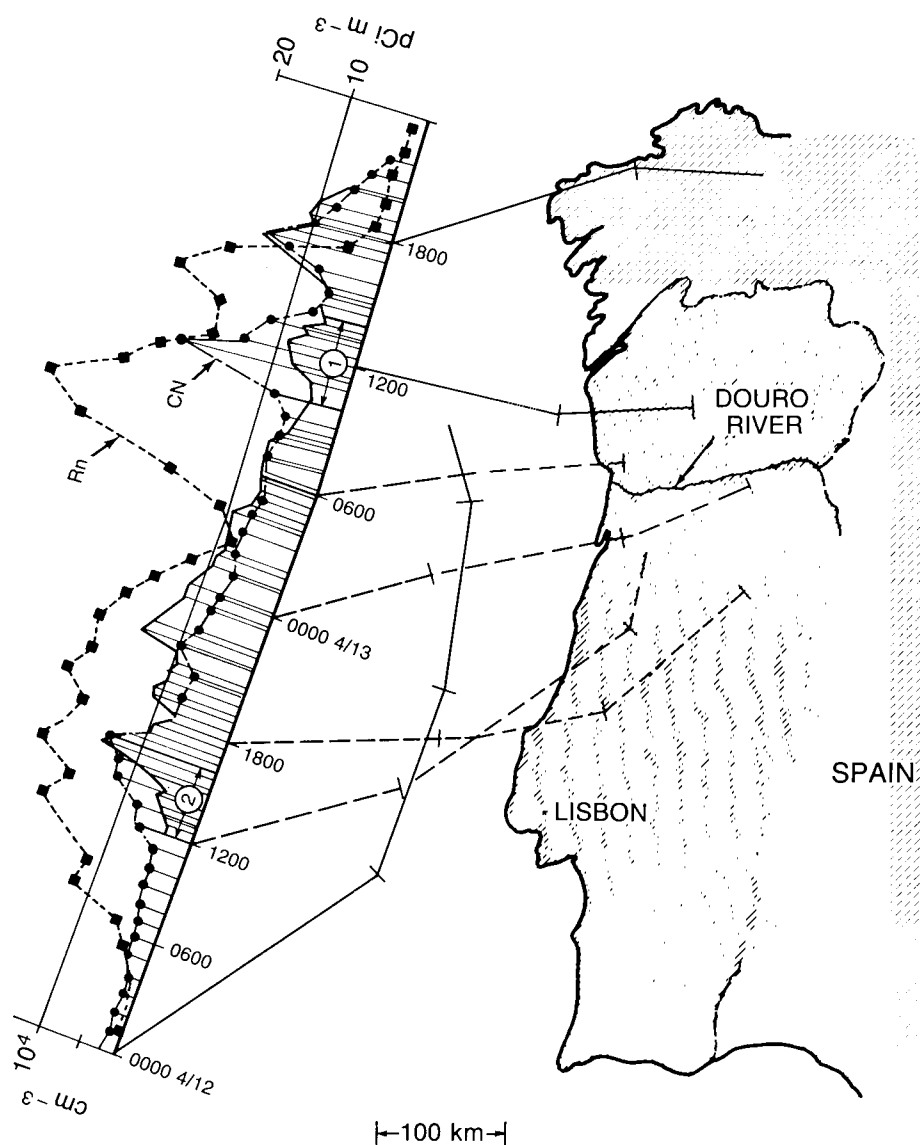


Fig. 20 — Back trajectories for air encountered off the Iberian Peninsula where the tic marks indicate 6-hour intervals. Radon concentrations (squares), CN concentrations (circles), and integrated aerosol concentrations (solid line) measured along the track of the ship are plotted. (Scales are linear.)

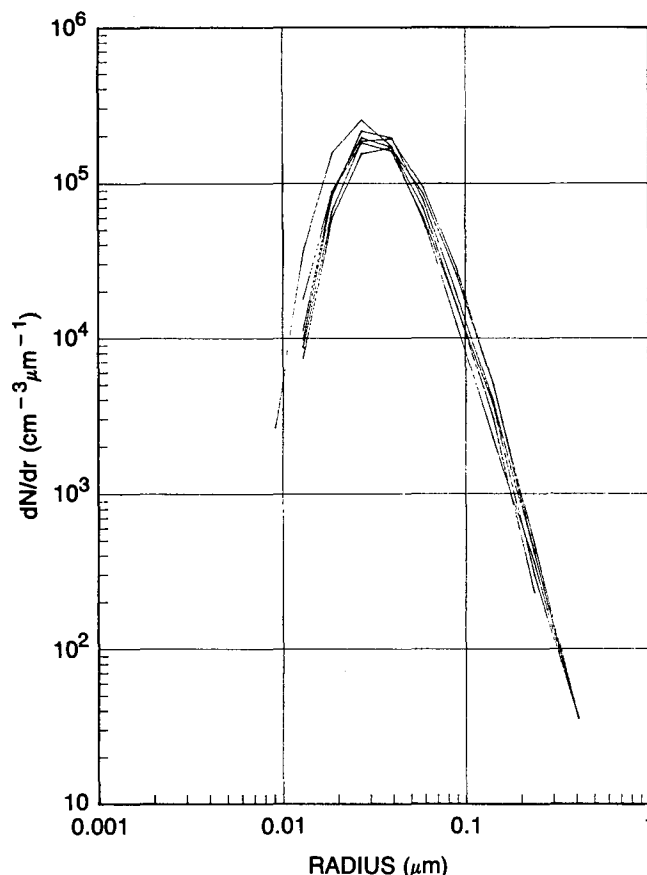


Fig. 21 — Composite of five size distributions taken between 0400 and 0700 GMT on April 13

size distributions have a single peak and a rapid decrease of particles smaller than about  $0.02 \mu\text{m}$ . The rapid decrease in concentration with decreasing size below  $0.02 \mu\text{m}$  is predicted (by coagulation theory) to occur in the time the air has been over water provided there is no new particle formation. In addition to coagulation, the slow growth of very small particles, caused by the condensation of nonvolatile reaction products, is an important mechanism for moving particles from the very small sizes into the intermediate portion of the submicron size distribution.

An increase in very small particles was observed during two periods. We believe these two periods were associated with homogeneous nucleation and growth of new particles from gas-phase reaction products. The times of occurrence of these two periods are shown in Fig. 20 by the two encircled numbers. Both occurred during midday in air that had been over water throughout the morning. On both occasions the concentrations of condensation nuclei measured with the Gardner counter exceeded the total concentration of particles measured with the mobility analyzer, thus indicating the existence of particles below the size range detected by the mobility analyzer.

The size distributions between 1020 and 1300 GMT on 13 April are shown in Fig. 22. These size distributions followed those shown in Fig. 21. Curve 1 is the average of two size distributions taken between 1020 and 1105 GMT, Curve 2 is the average of two distributions taken between 1110 and 1220 GMT, and Curve 3 is the average of two size distributions taken between 1225 and 1245 GMT. The six size distributions were reduced to three for clarity of display. If the six distributions are viewed individually, the same general evolution is apparent. The evolution of the distribution during the second event is shown in Fig. 23. In this case we had no size distributions just before the

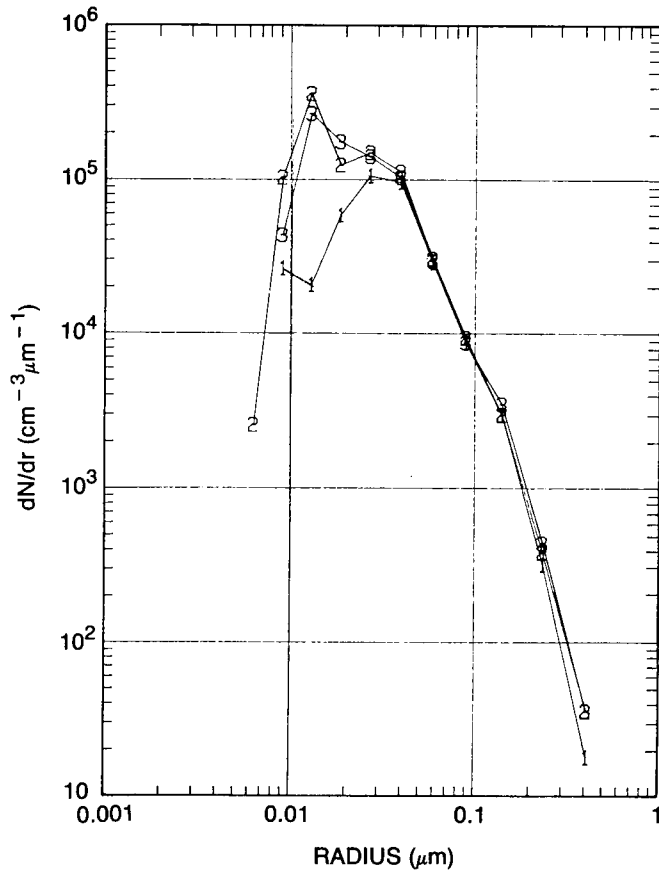
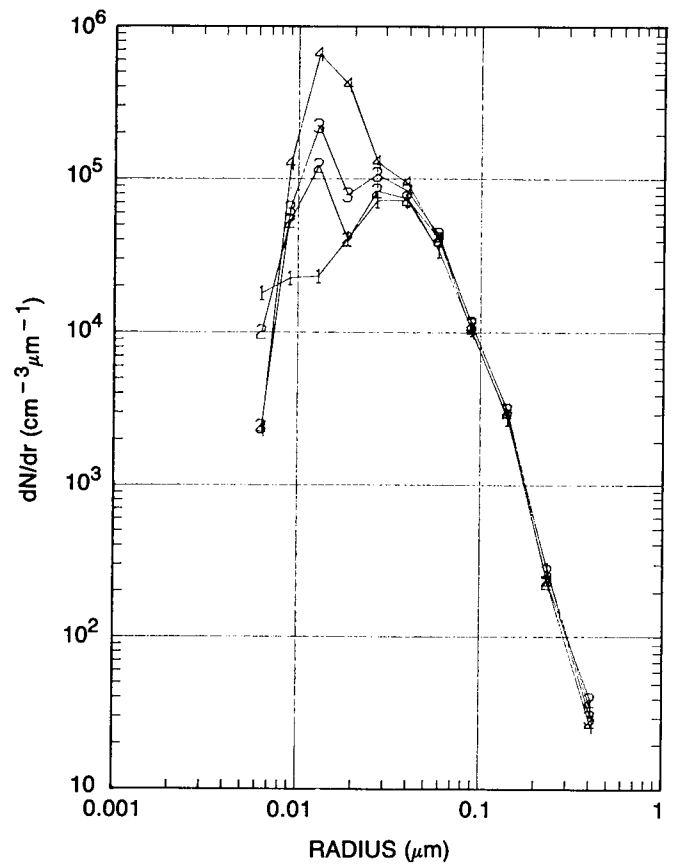


Fig. 22 — Evolution of the size distribution during period one (1020 to 1300 GMT on April 13.)

Fig. 23 — Evolution of the size distribution during period two (1150 to 1630 GMT on March 12).





event. Curve 1 is the average of two size distributions taken between 1155 and 1240 GMT on 12 March. Curve 2 is the average of two distributions taken between 1250 and 1330 GMT, Curve 3 is the average of two distributions taken between 1340 and 1425 GMT, and Curve 4 is the average of four size distributions taken between 1430 and 1625 GMT.

Since the two previous events occurred while the ship was close to land, a possible explanation might be that small particles encountered during these events were generated over land and advected to the location of the ship. However, this is unlikely because the air had been over water for 6 to 12 h, and coagulation calculations predict that particles in the 0.007 to 0.02  $\mu\text{m}$  size range would be greatly reduced below their continental levels during the 6- to 12-h period and that the resulting size distributions would resemble those shown in Fig. 21. Another reasonable speculation might be that the small particles were due to ship traffic along the coast. However, there were no visual sightings of ships upwind during these periods, and it has been our experience that small particles from exhaust plumes of ships give more erratic and transient readings than those observed during these two events. As will be discussed later, the evolution of the distribution observed during these two events is similar to what is expected (based on calculations and chamber experiments) for new particle formation and growth from gas phase reaction products. We therefore believe that during these periods we are observing spontaneous formation and growth of new particles directly from low volatility products formed by gas-phase reactions. Most likely, these reactions were photochemically induced, since they occurred in air that had spent the morning daylight hours over water.

#### 4. DISCUSSION OF MECHANISMS DETERMINING THE SIZE DISTRIBUTION

The size of an aerosol particle is a dynamic quantity that changes in response to a number of different processes acting on different time scales. In addition to the usual microscale aerosol mechanisms such as coagulation and condensational growth, larger scale atmospheric processes that involve atmospheric transport and the passage of the aerosol through nonprecipitating and precipitating cloud cycles have profound effects on the size distribution. An important goal of this work is to determine the relative importance of each mechanism as a function of particle size and time scale.

The change in the size distribution,  $n(r, x, t)$ , can be expressed as

$$\frac{\partial n}{\partial t} + \nabla \cdot J = Q(r, x, t) + \left( \frac{\partial n}{\partial t} \right)_{\text{coag}} + \left( \frac{\partial n}{\partial t} \right)_{\text{cond}} + \left( \frac{\partial n}{\partial t} \right)_{\text{cloud}} + \left( \frac{\partial n}{\partial t} \right)_{\text{precip scav}} \quad (1)$$

The size distribution is a function not only of the radius  $r$  but also of time  $t$  and position  $x$ .  $J$  is the flux per unit size interval given by

$$J = n v - n v_g$$

where

$v$  is the flow velocity

$v_g$  is the gravitational fall velocity

$Q$  is the rate at which particles are formed per unit volume per unit size interval.

The terms on the right represent the change in the size distribution because of coagulation, condensational growth, nonprecipitating cloud cycles, and loss by precipitation scavenging. The terms on the right do not involve spatial gradients. The general solution to Eq. (1) must be calculated numerically. The difficulties in obtaining realistic solutions to Eq. (1) are not simply those of representing

each process by the correct mathematical formulation and devising a stable computational algorithm. As will become apparent later, a more limiting factor is our lack of data as to the correct values of the empirically determined parameters that occur in the equations (such as nucleation rates, chemical conversion rates for condensable species, deposition velocities, and the frequency of passage of air through clouds.)

In this section each term in Eq. (1) will be considered individually, and an order-of-magnitude estimate of the *decay time* associated with each term will be calculated. The decay times are indicative of the time scale at which particles are removed but give little information about the rate at which particles enter a given size range, except by inference. If particles are observed in a given size range, then there must be a source of particles sufficient to sustain the observed concentrations against the removal process. In the following analyses, horizontal gradients and vertical structure will be neglected; we will consider changes in a vertical Lagrangian column of air moving with the mean wind speed. The time scales discussed will be representative of the remote ocean areas, and the numerical values given will be much different than they would be had the analysis been done for the continental case.

#### 4.1 Surface Deposition

Ignoring the right-hand side of Eq. (1) and integrating over a volume  $V$  gives

$$\frac{\partial}{\partial t} \int n(r) dV = - \int \nabla \cdot J dV = - \int J \cdot dS,$$

where the last term is obtained by using the divergence theorem. If the volume is taken to be a column of unit cross section  $\Delta S$  extending to the height  $H$  of the well-mixed layer, and if we further assume that horizontal gradients are negligible, then

$$\frac{\partial}{\partial t} \int n(r) dV = - n_g(r) v_g \Delta S$$

where  $v_g$  is the downward velocity at the surface, and  $n_g(r)$  is the size distribution at the surface. In keeping with the conventional concept of deposition velocity, we assume that the boundary layer is well mixed so that  $n(r)$  is uniform with height, and the velocity at the surface  $v_g$  is given by the empirically determined deposition velocity  $v_d$ , then

$$\left[ \frac{\partial n(r)}{\partial t} \right]_{\text{deposition}} = - \frac{v_d(r)}{H} n(r)$$

and

$$n(r) = n_o(r) \exp \left[ - \frac{v_d(r)}{H} t \right]. \quad (2)$$

The decay constant for deposition is therefore

$$\tau_d(r) = \frac{H}{v_d(r)}. \quad (3)$$

Figure 24 shows the decay constant for deposition found by using the deposition velocities over ocean surfaces given by Giorgi (1986; Fig. 4) for wind speeds of 1, 5, 10, and 20 m s<sup>-1</sup>. Except for particles with radii greater than 10  $\mu\text{m}$ , these decay times are much longer than those usually associated with aerosol lifetimes. We therefore conclude that under most conditions surface deposition is important only for particles with radii greater than  $\sim 5 \mu\text{m}$ .

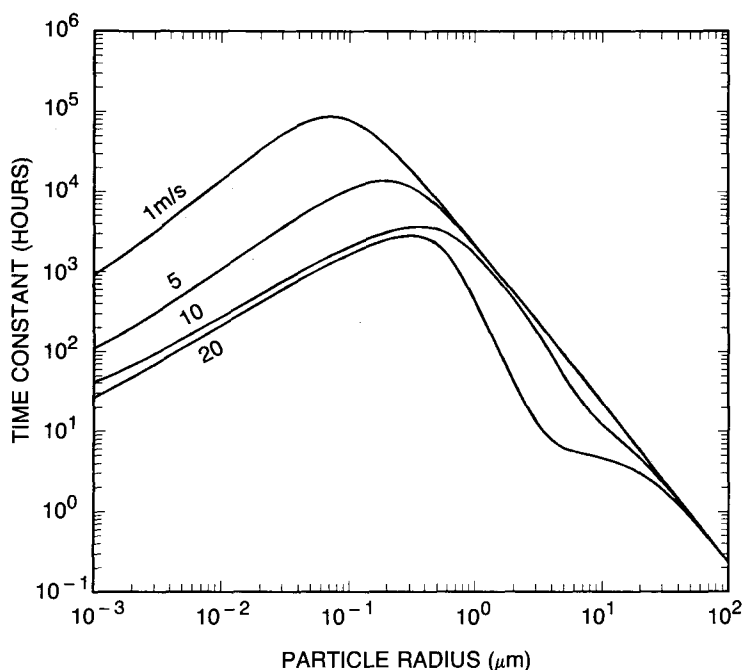


Fig. 24 — Decay constants for particle deposition on the ocean surface as a function of size and wind speed

## 4.2 Coagulation

Coagulation transfers mass from smaller sizes to larger sizes with no net loss of mass. Coagulation rates depend on the shape of the size distribution as well as the total aerosol concentration. Figure 25 plots the coagulation coefficient [following Fuchs (Twomey, 1978)] for various sizes of particles as a function of the smaller size particle. It is clear that the coagulation coefficient for a smaller particle combining with a larger particle is much greater than the coagulation coefficient for two particles of the same size.

If the loss of particles of a given size  $r$  due to coagulation with particles of all other radii  $\rho$  is considered, then the coagulative loss is given by

$$\left[ \frac{\partial n(r)}{\partial t} \right]_{\text{coag}} = - n(r) \int_0^\infty K(r, \rho) n(\rho) d\rho, \quad (4)$$

where  $K(r, \rho)$  is the coagulation coefficient, and the decay constant for a particle of radius  $r$  is

$$\tau_{\text{coag}} = \frac{1}{\int K(r, \rho) n(\rho) d\rho}.$$

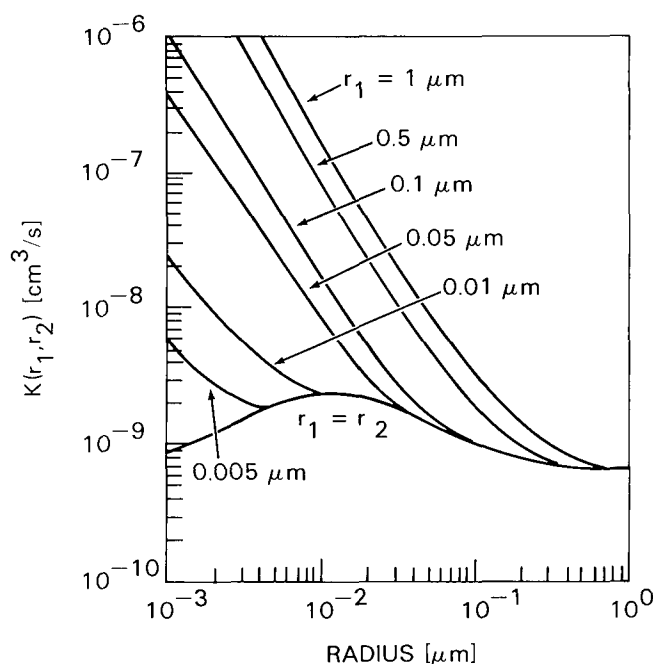


Fig. 25 — Coagulation coefficients for particles of the indicated radius with particles of smaller radii (abscissa)

To evaluate the decay constant, a particular size distribution must be chosen. The decay constant was evaluated for the size distribution shown by curve 4 of Fig. 7, which is typical of size distributions found in the remote Atlantic when continental influences are at a minimum. The decay constant for particles smaller than  $0.06 \mu\text{m}$  is shown in Fig. 26. Most coagulation events involve coagulation of particles of  $r < 0.05 \mu\text{m}$  with particles of  $r > 0.05 \mu\text{m}$ . This calculation was also carried out for size distributions found off the Iberian Peninsula (shown in Fig. 21). Because of the large number of particles, the coagulative decay times were about an order of magnitude faster (10 times faster at  $0.01 \mu\text{m}$  and 20 times faster at  $0.04 \mu\text{m}$ ). The coagulative time scale for particles smaller than  $0.1 \mu\text{m}$  is smaller than the deposition time scale even for the case of the remote tropical Atlantic. The effect of coagulation is to rapidly remove mass from the very small sizes and transfer it into the radius range from about  $0.05$  to  $0.2 \mu\text{m}$ . Because the mass of small particles is usually quite small, this transfer of mass to larger particles has only a small effect on the larger particles.

### 4.3 Gas-To-Particle Conversion

Trace gases are continually being injected into the atmosphere from natural and anthropogenic sources. These volatile gases are removed from the atmosphere after they undergo chemical reactions that convert them to less volatile compounds. Chemical reactions can occur either in the gas phase (for example, photochemical reactions) or by reactions subsequent to absorption on existing particles or cloud droplets. In most cases, trace gases will pass through the particulate phase before being removed by precipitation scavenging. If the gases are absorbed into cloud droplets and there undergo chemical transformation to less volatile material, then this material will end up as aerosol mass when the cloud evaporates. There are three mechanisms for converting gases to particulate matter. Trace gases can be converted in the gas phase to less volatile product that condense on existing particles causing growth of the existing population, or condense spontaneously to form new particles (homogeneous nucleation). Trace gases can also be absorbed into cloud droplets where they are converted to involatile compounds during the aqueous phase. The residue remaining after evaporation is an aerosol of increased mass.

It is clear that the relative importance of these three processes depends on the concentration, and chemical nature of the trace gases present in the atmosphere and the rate at which they react, either in

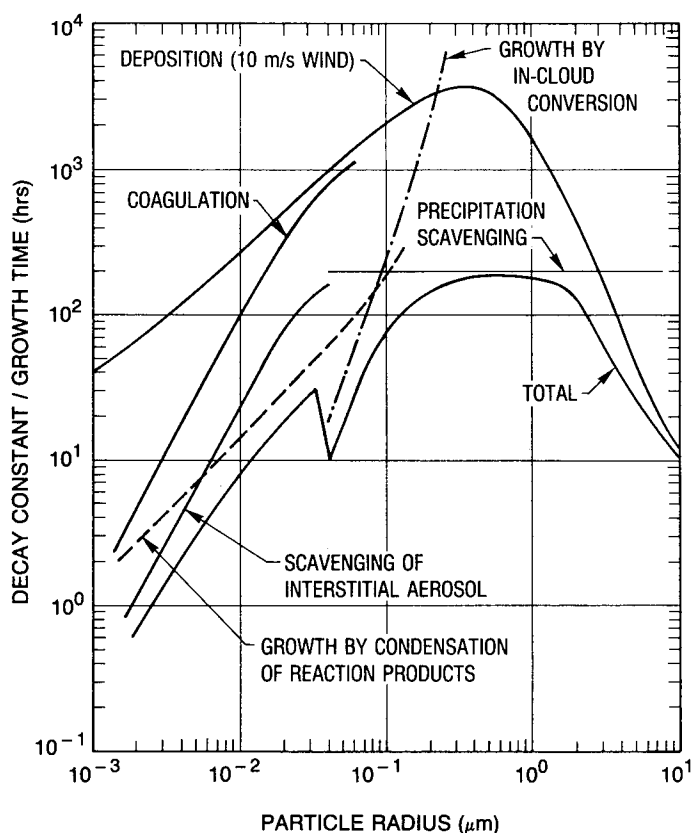


Fig. 26 — Decay constants and/or growth times for various aerosol removal mechanisms. The bottom line is the cumulative removal time.

the gaseous or the aqueous phase. It is well known that  $SO_2$  emitted into the atmosphere by anthropogenic sources is a source of sulfuric acid and sulfate particles in continental air. Excess non-sea-salt sulfate found in remote oceanic aerosol particles has led to the conclusion that there must also be an oceanic source of sulfate. A possible source of this sulfate is thought to be dimethyl sulfide (DMS).

The yearly global injection of DMS from the oceans is estimated by Andreae and Raemdonck (1983) and Andreae et al. (1985) to be  $40 \pm 20 \text{ Tg S yr}^{-1}$ , whereas Bates et al. (1987) estimates the global flux to be  $17 \text{ Tg S yr}^{-1}$ . In either case, DMS is clearly a significant portion of the global natural sulfur flux of 60 to 90  $\text{Tg S yr}^{-1}$  (Andreae et al., 1985). The natural and anthropogenic sources of sulfur are about equal, but most anthropogenic sulfur is emitted as  $SO_2$  over the continents of the northern hemisphere. The importance of DMS as a source of sulfur in remote oceanic regions must be relatively large and could account for most of the non-sea-salt sulfate in marine aerosols. Experiments by Hatakeyama et al. (1985) show that the photooxidation of DMS gives about 21%  $SO_2$ , and the remaining sulfur is converted to methane sulfonic acid (MSA). Experiments by the same authors also show that the photooxidation of DMS in humid air (relative humidity (RH) = 35%) containing 12 ppb DMS and 6 ppb NO produced large concentrations of particles in which MSA and sulfuric acid were detected. Experiments by Hoppel et al. (1987) show that oxidation of DMS ( $\sim 30 \text{ ppb}$ ) by simulated sunlight in a  $600 \text{ m}^{-3}$  chamber that had previously been flushed with filtered outside air initially produced a large number of very small particles ( $r < 0.005 \mu\text{m}$ ). New particle formation ceased after about 10 min, and the existing particles grew throughout the subsequent 8 h during which the air was irradiated. Growth ceased when the irradiation was turned off. In these chamber experiments, the concentration of DMS was much larger than that which exists in nature; how representative they are of the natural environment is unknown.

The water-sulfuric acid system has been explored by a number of investigators (Reiss, 1950; Mirable and Katz, 1974; Hoppel, 1975). At 80% RH, a sulfuric acid vapor pressure of  $10^{-16}$  atm is required to saturate the environment;  $10^{-10}$  atm is required to sufficiently supersaturate the environment for homogeneous nucleation to occur (Hoppel, 1975). At intermediate supersaturations, sulfuric acid solution will condense on existing particles. The MSA-water system has been investigated recently by Hoppel (1987) and shows that an MSA vapor pressure less than  $10^{-12}$  atm saturates the atmosphere at 80% RH, while about  $10^{-8}$  atm will cause homogeneous nucleation. It is clear that sulfuric acid has a greater nucleation potential than MSA has. Furthermore it has been experimentally observed that the nucleation threshold for sulfuric acid is even less when ammonia is present. (Presumably the particles formed are ammonium sulfate.) Once new embryos are formed, they grow slowly to sizes observable as condensation nuclei at a rate determined by the very low concentrations of the condensing species. It is not our purpose here to champion any particular reaction but to show that substances that have a high potential to nucleate new particles do exist in the marine environment. This is probably the source of the small particles observed over the oceans. Production of particles by homogeneous nucleation is discussed later in this report. To make a quantitative estimate of particle growth, we will assume that disintegration of DMS is the only source of convertible material and that all the sulfur is converted to MSA or sulfuric acid. For our estimates it will make little difference how the sulfur partitions between the two acids or if the acid is converted to sulfate, since all these products have about the same molecular weight.

If the flux of DMS is  $140 \mu\text{g S m}^{-2}$  per day (Bates et al., 1987), and if DMS is converted uniformly to a strong acid within a 1-km-thick marine boundary layer, then the volume production rate would be about  $0.14 \mu\text{g S m}^{-3}$  per day. If all the acid is converted to particulate matter, this would replenish  $1.4 \mu\text{g of S}$  ( $4.2 \mu\text{g of acid}$ )  $\text{m}^{-3}$  in 10 days. Our data taken in the remote tropical regions indicate that the mass loading of particles smaller than  $0.3 \mu\text{m}$  is typically in the  $1$  to  $4 \mu\text{g m}^{-3}$  range. Thus the DMS injected into the atmosphere is sufficient to sustain the observed aerosol load of small particles against removal, provided it is all converted to particulate matter.

#### 4.3.1 Condensational Growth

The change in the size distribution caused by the condensation of gas phase reaction products on the surface of existing particles is given by Friedlander (1977).

$$\left[ \frac{\partial n(r)}{\partial t} \right]_{\text{cond}} = - \frac{\partial}{\partial r} [n(r) f(r)] = - f(r) \frac{\partial n(r)}{\partial r} - n(r) \frac{\partial f(r)}{\partial r}, \quad (5)$$

where  $f(r)$  is the growth law ( $dr/dt$ ). The first term on the right represents the change in the size distribution because of its slope. For example if the slope is positive, more particles will grow out of a size interval  $dr$  than into the size interval (assuming the growth rates were constant across the interval). The last term represents the change in  $n(r)$  caused by any change in the growth law as a function of radius. Therefore, it is clear that a simple decay time as defined for coagulative loss and surface deposition does not exist for growth. However, we can define a *growth time* that would remove all particles in a given size bin and ignore the rate at which smaller particles grow into the bin. The magnitude of this growth time, when compared to the decay time, will indicate the relative importance of various mechanisms that remove particles from any given size range.

For condensational growth the growth law is given by

$$f(r) = \frac{dr}{dt} = \frac{D'(r)}{\rho_p r} [\rho(\infty) - \rho(r)], \quad (6)$$

where

$\rho(\infty)$  is the environmental vapor density of the condensing species and  
 $\rho(r)$  is the vapor density at the surface of the particle. (For a completely  
 involatile species  $\rho(r)=0$ .)

$\rho_p$  is the density of the particle

$D'(r)$  is the effective diffusion coefficient given by

$$D'(r) = \frac{D}{\frac{r}{r + \lambda} + \frac{4D}{r\bar{v}}}$$

where

$D$  is the diffusion coefficient for the condensing species,

$\lambda$  is its mean free path, and

$\bar{v}$  is the mean thermal velocity.

The effective diffusion coefficient accounts for the transition from the kinetic theory to the diffusion regime of condensation as the particle radius increases in size through the transition region ( $r \approx \lambda$ ). If the condensing species is produced at a continuous rate  $q$  by gas phase reactions in the atmosphere, then the environmental concentration is determined by a balance between the rate of mass production  $q$  and the rate of diffusion to existing particles:

$$q = 4 \pi \rho(\infty) \int D'(r) r n(r) dr$$

or

$$\rho(\infty) = \frac{q}{4 \pi \int D'(r) r n(r) dr} \quad (7)$$

By using the  $q$  obtained earlier for the rate at which DMS is converted to sulfate or methane sulfonate and the size distribution for remote tropical Atlantic aerosol, the vapor concentration  $\rho(\infty)$  and the growth time can be evaluated from Eqs. (6) and (7). The time required for a particle to grow from  $r$  to  $1.5r$  is shown by the dashed line in Fig. 26. The criteria of increasing the radius by 50% is arbitrary and taking a different value would, of course, change the curve shown in Fig. 26. We used the 50% increase because that is roughly the channel width used for the mobility analyzer, i.e. the growth time shown is approximately the time required for all the particles in one channel to grow into the next larger channel. The value of  $q$  used to calculate the growth rate was  $2.5 \times 10^{-18} \text{ g cm}^{-3} \text{ s}^{-1}$ , which is one half the volume production rate for conversion of DMS cited earlier. (The other half will be reserved for conversion in cloud processes.)

#### 4.3.2 Nonprecipitating Cloud Cycles

The source and persistence of the double-peaked size distributions observed in the remote tropical Atlantic was puzzling. Coagulation and condensational growth would tend to fill in the gap. Our initial hypothesis was that the peak at  $0.08 \mu\text{m}$  was caused by the generation of sea-salt particles at the sea surface, and the peak at  $0.03 \mu\text{m}$  was the result of small particles formed by gas-to-particle conversion. If this were the case, then the involatile sea-salt particles could be distinguished from the more volatile sulfates and nitrates by measuring the size distribution before and after passing the sample through a heated tube, as had been done previously for cloud condensation nuclei (CCN) by

Twomey (1968) and Dinger et al. (1970). During a subsequent cruise in 1984 aboard the NOAA Ship *Discoverer* in the remote tropical Pacific, size distributions were taken alternately with and without passing the air through a tube heated to 300° C. Similar double-peaked size distributions were observed without the preheater; however, less than 10% of the particles under both peaks (less than 0.3  $\mu\text{m}$  radius) were sufficiently involatile to be classed as sea-salt particles. An average of several size distributions taken in the intertropical convergence zone (ITCZ) between the Hawaiian Islands and Tahiti are shown in Fig. 27, along with the Atlantic double-peaked distributions. These Pacific size distributions were usually characterized by lower concentrations (150  $\text{cm}^{-3}$  compared to 250  $\text{cm}^{-3}$  for the tropical Atlantic), with the peak occurring at about 0.1  $\mu\text{m}$  compared to 0.08  $\mu\text{m}$  for those of the Atlantic cruise. More precipitation was encountered in this region of the Pacific than had been encountered in the Atlantic, and precipitation scavenging may have played a more important role. When the aerosol sample was passed through the heater, which in the laboratory had been shown to destroy sulfuric acid and sulfate aerosol but not sea-salt aerosol, at least 90% of all the particles measured with the DMA disappeared, thus indicating that they were not sea-salt particles. A possible explanation of this result, which still allows for an oceanic source, is that the sea-surface-generated aerosol is surface active material scavenged from the sea surface by rising bubbles (Blanchard, 1983). Most surface active material is quite volatile. Although the facilities available aboard ship were limited, we were able to construct an aerosol generator by forcing air through a ceramic frit covered with sea water. Filtered air flowing over the bubbling water carried the particles produced by the bursting bubbles to the DMA. The water used in this experiment was skimmed from the sea surface by crew members in a small boat several hundred meters from the ship. The size distributions produced by this generator for the cases when the sample was heated and unheated are shown in Fig. 28. Within the limits wherein we could maintain a constant generation rate over the measurement period, the heated and unheated samples were the same, thus indicating that the bubbling process was producing only involatile sea-salt particles. There are, of course, several criticisms of this experiment. Most important is that the water surface above the rising bubbles is more disturbed than the ocean surface and any surface active material may have been rapidly depleted. Nevertheless, we view the results of this experiment as one of a number of evidences that contribute to our conclusion that it is unlikely that the peak at about 0.1  $\mu\text{m}$  is generated by activity at the sea surface. A more likely explanation is that the minimum at about 0.05  $\mu\text{m}$  and peak at about 0.1  $\mu\text{m}$  is due to the action of cycling marine boundary layer air through nonprecipitating clouds that cap the marine boundary layer.

All cloud droplets are initially formed on a subset of aerosol particles that are called *cloud nuclei*. During the cloud phase, the droplets absorb trace gases and convert some of the gaseous material to particulate matter. In addition to chemical conversion of trace gases, the smaller unactivated interstitial aerosol diffuses to the cloud droplets, thus transferring mass from the smaller particles to the much larger cloud droplets. When the cloud droplets later evaporate, the resulting residue is larger than the original cloud nucleus on which the droplet formed. Averaged globally, the nonprecipitating cloud cycles repeat themselves 10 to 25 times before a precipitating cloud system develops (Pruppacher, 1986). Therefore, the aerosol is cycled through more than 10 nonprecipitating clouds (on the average) before the particles can be removed by precipitation scavenging.

Evidence supporting the nonprecipitating cloud hypothesis as the source of the double-peaked feature has been detailed by Hoppel et al. (1986) and includes (a) volatility measurements, discussed earlier, that show the particles under both peaks are much too volatile to be sea-salt; (b) case studies that show the double-peaked characteristic was associated with air that had passed through regions containing boundary layer clouds (see the Canary Island case study); (c) the minimum between the two peaks occurs in the radius range 0.04 to 0.07  $\mu\text{m}$ , from measured values of radius vs critical supersaturation (Fitzgerald and Hoppel, 1984), this would correspond to a critical supersaturation in the 0.1 to 0.4% range, which is in good agreement with expected cloud supersaturations; (d) the number of particles under the 0.09  $\mu\text{m}$  peak is in the 50 to 130  $\text{cm}^{-3}$  range, which is a reasonable



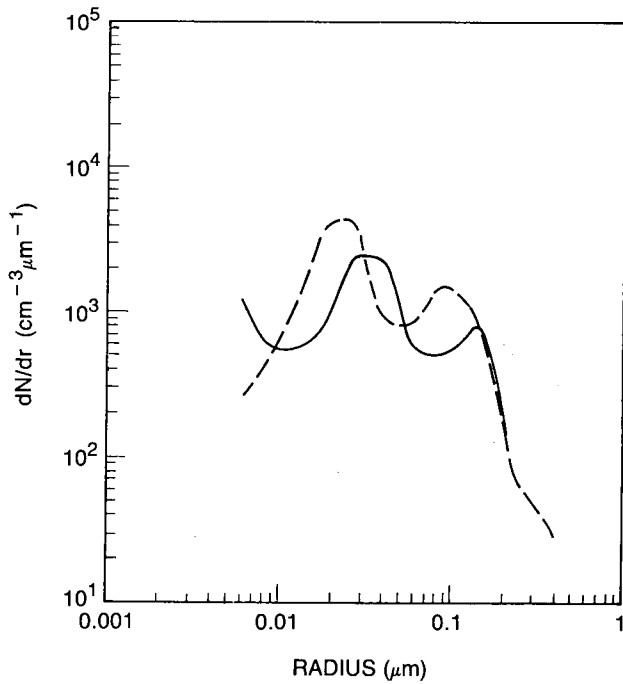
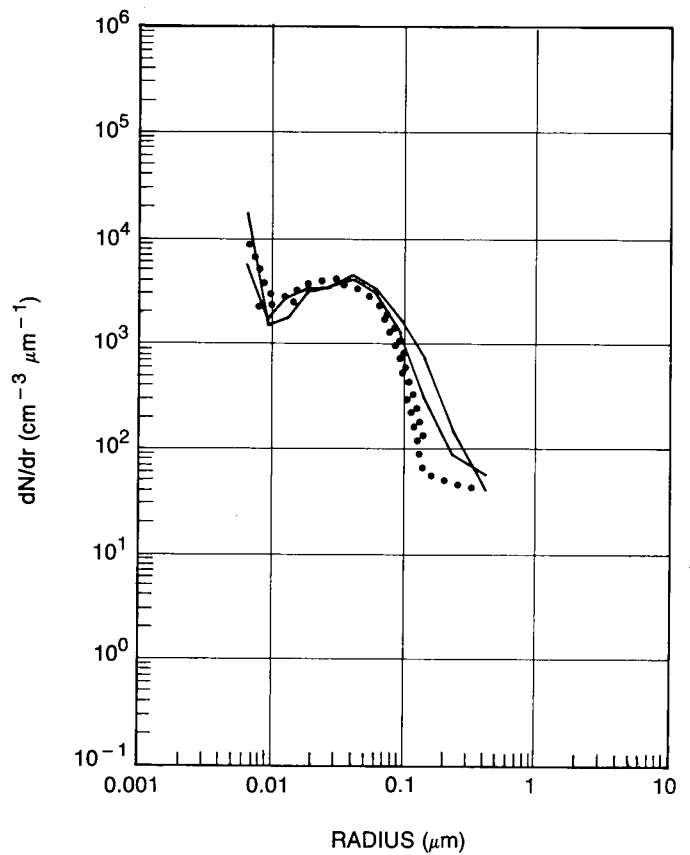


Fig. 27 — Comparison of size distributions observed in the tropical Atlantic are indicated by the dashed line, those observed in the remote tropical Pacific are represented by the solid line.

Fig. 28 — Size distribution produced by bubbling air through sea water. The solid line is unheated sample; dotted line is the heated sample.



number for cloud droplet concentrations in clouds, and (e) the source of convertible gases emanating from the sea surface is adequate to sustain the observed size distribution against removal mechanisms.

The rate at which particles grow out of a given size range during nonprecipitating cloud cycles can be estimated if the conversion rate of trace gases in the cloud phase is known. Cloud processes will only increase the mass of those particles that are large enough to act as cloud condensation nuclei (CCN) and each cloud droplet will convert approximately the same amount of material regardless of the original size of the CCN. This means that the smaller CCN will show a larger fractional increase in mass than larger CCN. The growth rate of residual mass in a single cloud droplet  $M_p$  is related to the total mass conversion rate  $dM/dt$  by

$$\frac{dM_p}{dt} = \frac{1}{Z} \frac{dM}{dt}$$

where  $Z$  is the total number of cloud droplets. The equivalent dry radius growth rate (radius when water is removed) is

$$\frac{dr}{dt} = \frac{1}{4 \pi \rho_p r^2 Z} \frac{dM}{dt}$$

where  $\rho_p$  is the density of the particle. Assuming a constant conversion rate, the time required for the radius of the dry aerosol (residue of cloud droplet) to increase its radius by 50% is given by

$$\tau_{50} = \frac{9.95 \rho_p Z}{dM/dt} r^3 \quad (8)$$

Assuming the in-cloud conversion rate to be  $2.5 \times 10^{18} \text{ g cm}^{-3} \text{ s}^{-1}$  (one-half of the DMS sulfur converted in the cloud phase), then the time required for the particle to increase its radius by 50% as calculated from Eq. (8) is shown by the dot-dashed line in Fig. 26. For the smallest CCN, estimated here to be  $0.04 \text{ } \mu\text{m}$  radius, growth by in-cloud conversion of trace gases in the liquid phase is the dominant removal process. The in-cloud conversion here is represented by a continuous process that we have assumed represents the average effect of passing the aerosol through nonprecipitating cloud cycles.

#### 4.4 Loss of Interstitial Particles to Cloud Droplets

Particles that are too small to act as CCN (interstitial particles) readily attach themselves to the large surface area provided by the cloud droplets during cloud cycles. This process, in which the interstitial particles diffuse to cloud droplets, is similar to coagulation already discussed, except now the collecting particles are the much larger cloud droplets. The loss of particles too small for activation ( $r < \text{about } 0.06 \text{ } \mu\text{m}$ ) can be written as

$$\frac{\partial n(r)}{\partial t} = - n(r) K(r,a)Z,$$

where  $Z$  is the concentration of cloud droplets,  $K(r,a)$  is the attachment coefficient for particles of radius  $r$  with cloud droplets having radius  $a$ . The time constant for loss of interstitial particles to cloud droplets is

$$\tau_{inter} = \frac{1}{K(r,a)Z}$$

The primary mechanisms for particle capture are Brownian diffusion of small particles to cloud droplets and gravitational collection of interstitial particles by larger cloud droplets as they fall slowly through the cloud. The attachment coefficients for the two mechanisms are

$$K(r, a) = 4\pi D(r)a \quad \text{for diffusion and}$$

$$K(r, a) = E(r)\pi a^2 V_r \quad \text{for gravitational settling}$$

where  $D(r)$  is the diffusion coefficient of the particle,  $V_r$  is the relative velocity between the particle and the cloud droplet, and  $E(r)$  is the collection efficiency that is assumed to be equal to 0.1 for all  $r$ . For particles smaller than the critical radius (unactivated), attachment by diffusion is more important than gravitational collection. If the cloud droplets are assumed to have a radius of about  $7 \mu\text{m}$  and a concentration of  $200 \text{ cm}^{-3}$  (liquid water content of  $0.3 \text{ g m}^{-3}$ ), and if we further assume that the aerosol spends 5% of its time in a cloud (corresponding to 5% of the marine boundary layer occupied by clouds), then the calculated time constant for loss of interstitial particles to cloud droplets is that shown in Fig. 26.

#### 4.5 Cumulative Removal Times

If the total time constant for removal  $\tau_{tot}$  is given by

$$\frac{1}{\tau_{tot}} = \sum_i \frac{1}{\tau_i},$$

and if we treat the 50% growth time for condensational growth and growth resulting from nonprecipitating clouds as a time constant, then the resulting decay time is shown by the heavy line in Fig. 26. Particles less than  $0.01 \mu\text{m}$  are removed primarily by condensational growth and interstitial cloud scavenging with a time constant of 1 to 10 h, and the mass is transferred to larger sizes. Particles with radii of  $0.02$  to  $0.03 \mu\text{m}$  have decay time constants on the order of one day. Those particles that are large enough ( $r > 0.05 \mu\text{m}$ ) to act as CCN during nonprecipitating cloud cycles pick up additional mass during the cloud phase, so that the smaller of the CCN with critical supersaturations corresponding to the supersaturation in the cloud grow rapidly out of that size range, causing the minimum in  $\tau_{tot}$ .

Precipitation scavenging is represented as a process that removes, with a time constant of 8 days, all particles large enough to be activated within the cloud. Precipitation scavenging is the only important removal process in the size range of about  $0.2$  to  $2 \mu\text{m}$ . For particles larger than  $5 \mu\text{m}$ , surface deposition is the important removal mechanism.

If the source of particles were the same at every size, then the cumulative removal time shown in Fig. 26 would approximate the shape of the size distribution. Since the observed size distributions fall off rapidly at radii above  $0.1 \mu\text{m}$ , the rate of particle formation at larger radii must be much smaller than at sizes below  $0.1 \mu\text{m}$ . Since smaller particles will not grow to sizes larger than about  $0.2 \mu\text{m}$ , either by condensation, coagulation, or cloud recycling, on a time scale important in the MBL, the larger sizes must originate at their observed size from the sea surface or over land. The (number) rate at which sea-surface particles are generated must, in the absence of high seas and strong winds, be much lower than the rate at which particles from the gas phase are formed. This interpretation is consistent with the observation that particles larger than  $0.5 \mu\text{m}$  exhibit a much higher correlation with wind speed than do particles smaller than  $0.5 \mu\text{m}$ , and are much less volatile.

It is important to remember that Fig. 26 assumes the size distribution observed in the remote tropical Atlantic. Use of a different size distribution, such as those observed off the west coast of the Iberian Peninsula, would result in a different cumulative curve from that shown. Most notably, the decay of small particles would be even more rapid because of the higher chemical conversion rates and increased rates of coagulation.

The results given in this section are order-of-magnitude estimates. A one-dimensional numerical model that solves Eq. (1) for all mechanisms acting simultaneously is under development at NRL and will result in a much better diagnostic and predictive tool with which to study and understand the dynamics of marine aerosols.

## 5. AEROSOL OPTICAL PROPERTIES

It is well known that absorption and scattering by aerosol particles in the atmosphere have an important effect on radiative transfer and the radiation budget of the earth. The aerosol optical thickness, being the vertically integrated value of attenuation caused by aerosols, is thus an important climate parameter. The aerosol scattering coefficient  $\beta_s$  near the surface is of obvious importance because of its relationship to visibility expressed by the Koschmieder formula:  $V = 3.91/\beta_s$ . In addition, the aerosol optical properties of the lower atmosphere affect the performance of optical and infrared sensors used in numerous military systems.

This section presents the results of measurements of aerosol optical thickness and the near-surface aerosol scattering coefficient made on the 1983 Atlantic cruise.

### 5.1 Aerosol Scattering Coefficient

#### 5.1.1 Calculations of the Scattering Coefficient from the Particle Size Distribution

In addition to the measurements of the scattering coefficient, aerosol scattering and extinction coefficients were also calculated from the particle size distributions measured on the transatlantic leg of the cruise. Scattering and extinction coefficients were calculated for 38 times between 1800 GMT on 13 March and 1000 GMT on 31 March, when both impactor and mobility analyzer particle size measurements were available.

The scattering coefficient is defined in terms of the particle size distribution by

$$\beta_s = \int_0^\infty \pi r^2 Q_s(m, r, \lambda) n(r) dr, \quad (9)$$

where  $Q_s$  is the Mie-theory scattering efficiency factor, and  $n(r) = dN/dr$  is the differential particle size distribution. The definition of the extinction coefficient  $\beta_e$  is identical to Eq. (9) except that  $Q_e$ , the extinction efficiency factor, replaces  $Q_s$ .  $Q_s$  and  $Q_e$  are functions of particle index of refraction  $m$  and wavelength  $\lambda$ .

The particle size distributions used to compute  $\beta_e$  and  $\beta_s$  were obtained by fitting a curve of the form

$$\ln [n(r)] = C_0 + C_1[\ln(r)] + C_2[\ln(r)]^2 + C_3[\ln(r)]^3 + \dots$$

to the measured values of  $dN/dr$  between 0.05 and 8.5  $\mu\text{m}$ . It was not necessary to fit the curve to data points below 0.05  $\mu\text{m}$  since the smallest particles make a negligible contribution to the scattering

and extinction at visible wavelengths. Since Eq. (9) cannot be integrated analytically, the particle size range was divided into 70 size intervals, and  $\beta_e$  was computed from

$$\beta_e = \sum_{i=1}^{70} \pi r_i^2 Q_e(m, r_i, \lambda) N_i, \quad (10)$$

where  $r_i$  is the midpoint radius of each size interval, and  $N_i$  is the number of particles in that interval. A Mie theory computer code developed by Dave (1968) was used to compute  $Q_s$  and  $Q_e$ .

The impactor samples particles outdoors, and it is assumed that it provides a particle size distribution at the ambient relative humidity. The mobility analyzer, on the other hand, measures the size distribution at a relative humidity less than ambient. The relative humidity in the mobility analyzer ranged from 11% to 27% below ambient. Thus, to calculate  $\beta_s$  and  $\beta_e$  for ambient relative humidity conditions, it was necessary to adjust the size of particles that were smaller than  $0.5 \mu\text{m}$ , to account for the difference between the mobility analyzer and ambient relative humidities. The adjustment was based on the model of equilibrium particle size as a function of relative humidity shown as curve 1 in Fig. 29. The ordinate is the ratio of particle radius at the indicated humidity to particle radius in dry state. This particle growth model assumes that 75% of the mass of the particles in dry state is water-soluble material, and 25% is insoluble material. The soluble material is assumed to behave like mixtures of ammonium sulfate and ammonium nitrate, as described by Hanel and Lehmann (1981). The effect of particle curvature on the growth curve is neglected, and curve 1 is applied to all particles irrespective of their size in dry state. This simplification is justified because the particle sizes for which the curvature effect is important contribute less than a few percent to the scattering and extinction coefficients at visible wavelengths.

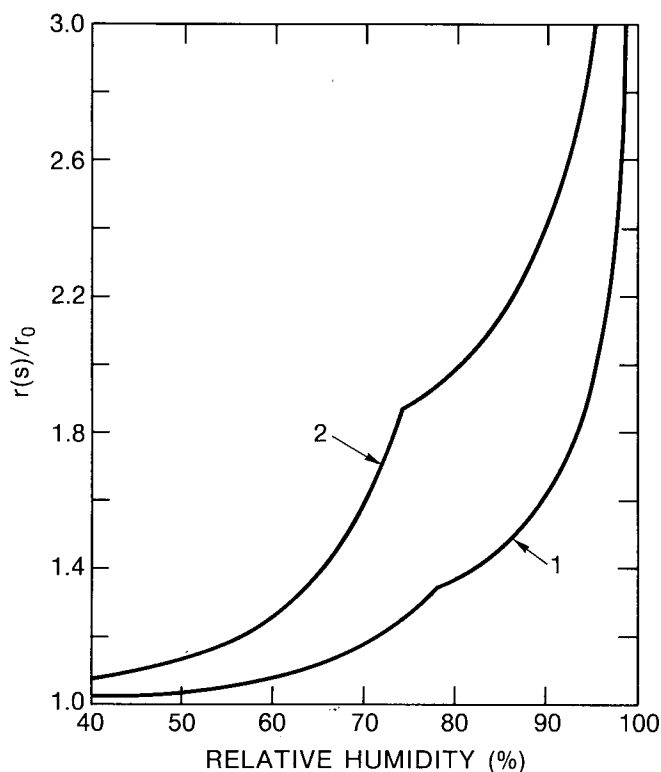


Fig. 29 — Ratio  $r/r_0$  of the radius of the wet to that of the dry particle as a function of relative humidity. Curve 1 is for particles with a radius  $< 0.5 \mu\text{m}$ . Curve 2 is the growth curve for sea spray aerosols (Hanel, 1976) and applies to particles that have a radius  $> 1.5 \mu\text{m}$ . The growth curve of intermediate-sized particles ( $0.5 \mu\text{m} < r < 1.5 \mu\text{m}$ ) is obtained by interpolating between curves 1 and 2.

The index of refraction of the particles must also be specified to calculate aerosol optical properties. The refractive index of particles at an ambient relative humidity  $S$  was computed from the expression (Hanel, 1968):

$$\begin{aligned} n(S) &= n_w + (n_o - n_w) \left[ \frac{r(S)}{r_o} \right]^{-3} \\ \kappa(S) &= \kappa_w + (\kappa_o - \kappa_w) \left[ \frac{r(S)}{r_o} \right]^{-3}, \end{aligned} \quad (11)$$

where the swelling factor  $r(S)/r_o$  is the ratio of particle size at humidity  $S$  to its size in dry state,  $n$  and  $\kappa$  are the real and imaginary parts of the index of refraction, and the subscripts  $w$  and  $o$  refer to water and the dry particle respectively. The swelling factor for particles smaller than  $0.5 \mu\text{m}$  is given by curve 1 in Fig. 29. Particles that have a radius larger than  $1.5 \mu\text{m}$  at the ambient relative humidity were assumed to be solution droplets formed on sea-salt nuclei. For these particles, the swelling factor is determined from curve 2 in Fig. 29, which is the growth curve for sea spray aerosols (Hanel, 1976). For relative humidity below 74%, curve 2 is the mean between the sea-spray aerosol growth curves for increasing and decreasing relative humidity. For  $r > 1.5 \mu\text{m}$ ,  $n_o$  and  $\kappa_o$  are the values for sea salt; for  $r < 0.5 \mu\text{m}$ ,  $n_o$  and  $\kappa_o$  were computed as

$$\begin{aligned} n_o &= 0.75n_{ws} + 0.25n_d \\ \kappa_o &= 0.75\kappa_{ws} + 0.25\kappa_d \end{aligned} \quad (12)$$

where the subscripts  $ws$  and  $d$  refer to water soluble and dustlike materials respectively. The index of refraction of water-soluble material, dustlike material, sea-salt, and water are taken from Shettle and Fenn (1979).

The swelling factor (growth curve) and index of refraction of particles in the range  $0.5$  to  $1.5 \mu\text{m}$  were assumed to vary with particle size and were determined by interpolating between the values for the larger and smaller particles. Thus, on the average, the properties of the intermediate-size particles became more and more like those of sea-salt as particle size approached  $1.5 \mu\text{m}$ .

### 5.1.2 Spatial Variations

Figure 30 shows the variations of the measured and calculated values of the aerosol scattering coefficient during the transatlantic leg of the cruise. HSS visiometer data are not included for the period from 2300 GMT on 15 March to 1400 GMT on 16 March because of the effects of precipitation, and for the period from 1200 to 2300 GMT on 26 March because the readings were affected by spray caused by the bow of the ship dipping into the waves. The Meteorological Research Instruments, Inc. (MRI) nephelometer was not operating from 1600 GMT on 15 March to 0200 GMT on 16 March. For clarity we have plotted the data at 4-h intervals. With the exception of the data for 15 March and for the period from about 1200 GMT on 26 March to 1200 GMT on 29 March, good tracking occurs between the HSS and MRI values, and between the measured and calculated values; all three values agree to within a factor of about 2.

A number of factors might have contributed to the large difference between the HSS and MRI values during the period of 26 to 29 March. First, as discussed in Appendix B, the windows of the HSS instrument were not cleaned from 1200 GMT on 26 March to 1500 GMT on 29 March. This

## ATLANTIC CRUISE

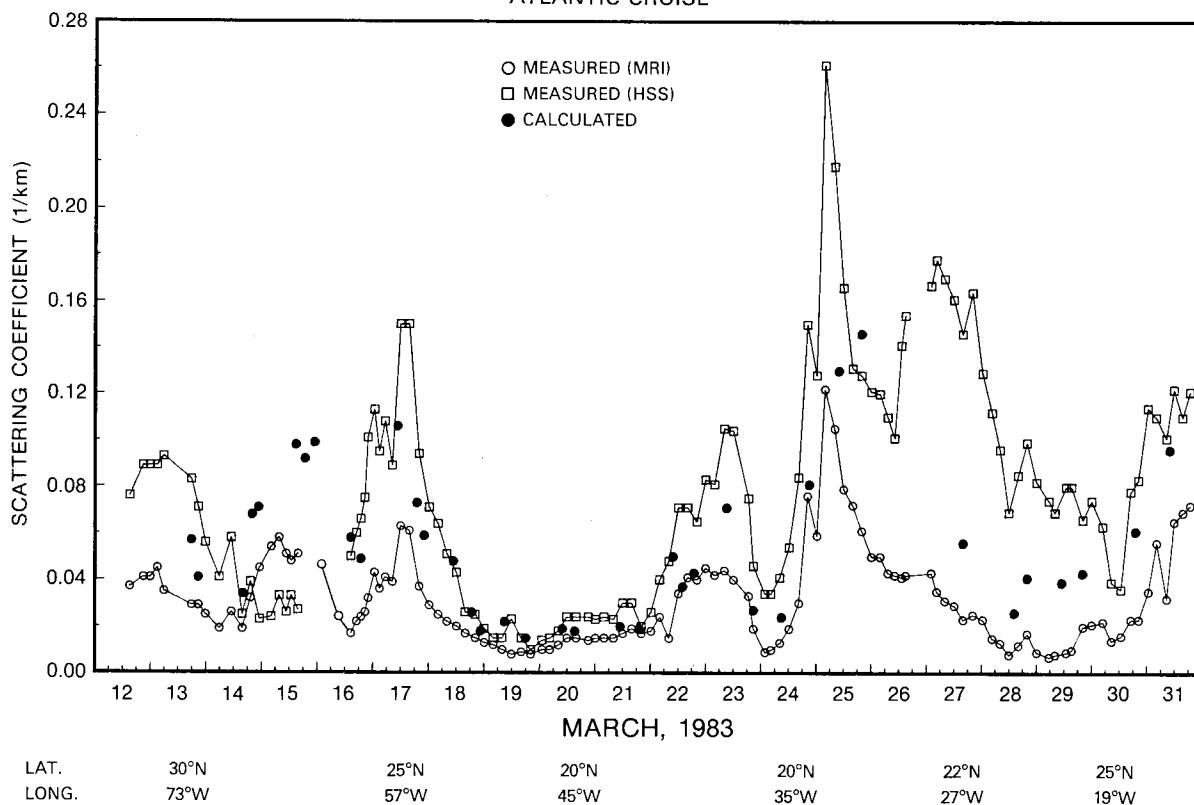


Fig. 30 — Variations of the measured and calculated values of the aerosol scattering coefficient during the transatlantic leg of the cruise

was a period of high winds and rough seas, and a significant coating of sea salt had accumulated on the windows of the HSS. When the instrument was recalibrated on 29 March, it was found that it read low by about 50%. To salvage these data, it was necessary to correct for the accumulation of deposit on the windows. This correction was made by using the observed wind speeds to estimate the rate at which the deposit built up over the 3 day period. However, in view of the large uncertainty in this estimate and the uncertainty of how the obscuring effect of the deposit varied with relative humidity, the accuracy of the corrected HSS readings is questionable.

A second factor that might have caused the corrected HSS to read too high during this period was the unusually weak wavelength dependence of the scattering coefficient. The primary calibration of the HSS, which uses a light source peaking at  $0.88 \mu\text{m}$ , was obtained by plotting its output voltage against the scattering coefficient measured with an MRI integrating nephelometer operating at  $0.475 \mu\text{m}$ . It is tacitly assumed by the manufacturer that this calibration is valid for all particle size distributions. However, since the variation of scattering coefficient with wavelength depends on the slope (shape) of the size distribution at the time of a given observation, it is possible that the HSS will overestimate or underestimate the scattering coefficient. This will depend on whether the particle size distribution at the time of a given observation is much flatter or steeper than those used in obtaining the primary calibration. The ratio of the scattering coefficient at a wavelength of  $0.475 \mu\text{m}$  to that at  $0.88 \mu\text{m}$  was calculated from the curve fits to the mobility analyzer and impactor size distribution data. The value of this ratio for the period 27 to 29 March (no impactor data were obtained on 26 March) ranged from 1.07 to 1.15. These were the lowest values of this ratio for the cruise. By contrast, the value of this ratio is about 1.8 for an aerosol having a Junge power-law size distribution ( $dN/dr \propto r^{-\nu}$ ) with  $\nu = 4$  (McCartney, 1976). This value of  $\nu$  is typical of continental hazes.

Further evidence that the accuracy of the HSS readings may depend on the particle size distribution is provided by the data of 15 March. Figure 30 shows that this was the only period of the cruise when the HSS read lower than the MRI. During this period the ratio of the scattering coefficient at  $0.475\ \mu\text{m}$  to that at  $0.88\ \mu\text{m}$  was in the range of 2.2 to 2.3, the highest values calculated on the cruise. If the accuracy of the HSS depended on the slope of the size distribution, one would expect a negative correlation between the ratio of HSS to MRI scattering coefficients and the ratio of the calculated scattering coefficient at  $0.475\ \mu\text{m}$  to that at  $0.88\ \mu\text{m}$ . The correlation coefficient between these two ratios was computed to be -0.60.

The spatial variation of the scattering coefficient is due to variations in the size distribution and chemical composition of the aerosol particles. These variations in aerosol properties result from changes in meteorological conditions such as relative humidity, wind speed, and air mass history, as well as from aerosol evolution caused by processes such as coagulation and condensation. From 13 to 14 March, the weather at the ship was influenced by the circulation around a departing low pressure center. During this period there was a dramatic decrease in the west-to-northwest flow from the continent, an advection of drier air, increased subsidence, and a decrease in particle continental character. The decrease in aerosol scattering during this period reflects these changes. On 15 March, the ship crossed the ridge line of the Bermuda high and entered the region of southeast trades. The period of the cruise within the subtropics, from about 15 to 27 March, did not have a continuous trade wind situation, but was characterized by transient subtropical disturbances (troughs) that greatly influenced the weather along the ship's route. Upper level troughs affected conditions at the ship between 16 to 18 March, on 22 March, and again between 25 and 26 March. These disturbed periods were characterized by an increase in low- and middle-level cloudiness, an increase in windspeed and relative humidity (see Figs. 2 and 4), and a less-well-defined boundary layer. Figure 30 shows that the aerosol scattering coefficient increased during these disturbed weather periods.

An analysis of air mass back-trajectories computed for the period 17 to 27 March (Parungo et al., 1984), shows that the air had transit times over water of at least 10 days before reaching the ship, except on 17, 23, and 25 March, during the periods of disturbed weather. The middle-level (850 mbar) trajectory for 1200 GMT on 23 March showed that the air had originated over northern Africa 9 days earlier. On 25 March, the 1200 GMT trajectory indicates that both the low-level (1000 mbar) and middle-level air originated over Africa 4 to 8 days earlier. While the trajectories for 17 March do not trace the air back to Africa, they do show that the air had passed over the Lesser Antilles several days earlier. Parungo et al. (1984) measured the size distribution and chemical composition of particles collected on these 3 days, and they found large increases in the concentration of particles larger than  $0.5\ \mu\text{m}$  radius and in the percentage of dustlike material (Si, Al, and Fe) contained in these particles. These aerosol measurements with the air trajectories provide strong evidence for continental influence on these days. The high values of the scattering coefficient on March 17, 23, and 25 coincide with the times of suspected continental influence in the vicinity of the ship.

Values of the scattering coefficient of about  $0.01\ \text{km}^{-1}$  measured on 19 to 20 March are probably typical of the values for the remote subtropical North Atlantic under conditions of a well-defined boundary layer, clean maritime air (i.e., air that has resided over the oceans for at least ten days), and low wind speeds.

### 5.1.3 Wavelength Dependence

Figure 31 is a composite of the 38 curves of calculated aerosol extinction coefficient vs wavelength. There seems to be a wide range in the dependence of extinction on wavelength. Some of the curves exhibit a weak dependence on wavelength, while others show a strong wavelength dependence over certain wavelength ranges. The variation of extinction with wavelength depends on



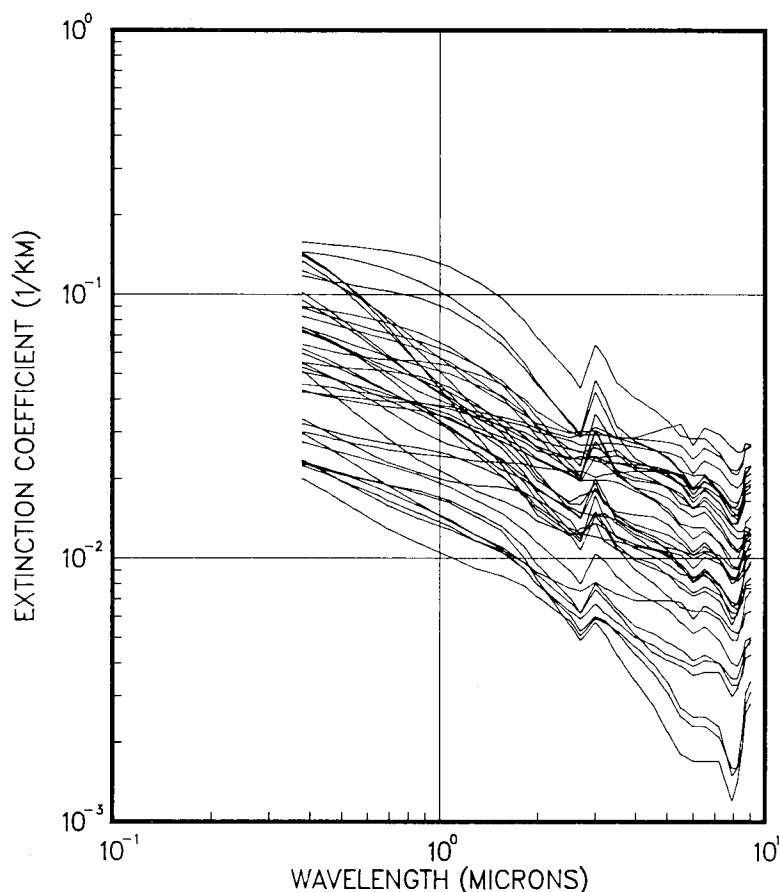


Fig. 31 — Composite of the 38 curves of calculated aerosol extinction coefficient vs wavelength

the size distribution and chemical composition of the particles. Particle composition determines the wavelength dependence of the index of refraction. Relative humidity affects the amount of water on the particles and thus affects their refractive index, as described in Eq. (11). The increase in the value of the extinction coefficient at 3.0 and 8.7  $\mu\text{m}$  wavelengths is caused by the changes in the refractive index of the particles at these wavelengths.

Figure 32 shows the variation of extinction with wavelength for 9 selected times. Each curve is representative of aerosol behavior over a period of at least 8 h. Curve 2, at 2300 GMT, 15 March shows the largest decrease in extinction over the wavelength range 0.5 to 2.0  $\mu\text{m}$ . The size distribution at this time had the steepest slope in the range of 0.2 to 2.0  $\mu\text{m}$  radius for any distribution measured on the cruise. Curve 5 exhibits the largest falloff in extinction above 2.0  $\mu\text{m}$  wavelength. The size distribution (similar to curve 4 in Fig. 7) from which this curve was calculated had the steepest slope above 1  $\mu\text{m}$  radius observed during the transatlantic portion of the cruise. The wind speeds for the 36 h before 1600 GMT on 20 March were less than about 2.0 m/s. Thus, curve 5 is probably typical of the variation of extinction with wavelength in the infrared during extended periods of low wind speeds over the remote subtropical Atlantic. In contrast to curves 2 and 5, curve 8 displays a weak dependence of extinction on wavelength. The weak dependence of extinction on wavelength reflects the effect on the particle size distribution of a significant increase in the number of particles larger than 2  $\mu\text{m}$  radius following 4 days of wind speeds in the range of 7 to 12 m/s.

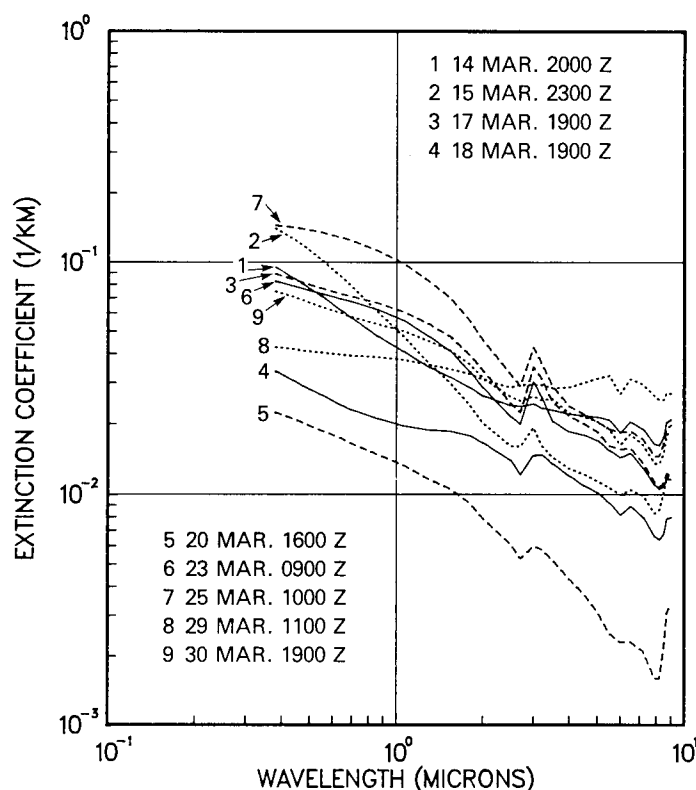


Fig. 32 — Calculated aerosol extinction as a function of wavelength for nine selected times

Table 3 lists the percent contributions to the calculated scattering coefficient at  $0.55 \mu\text{m}$  wavelength from particles in 4 size ranges. The relative contribution from different particle sizes depends on the particle size distribution. The contribution from particles smaller than  $0.15 \mu\text{m}$  was largest during the early part of the cruise, when the number of  $0.1 \mu\text{m}$  particles was the highest, and the slope of the distribution in the submicron size range was the steepest. The contribution from particles between  $0.15$  and  $0.5 \mu\text{m}$  ranged from 23% to 75%. The contribution from particles having  $<1.0 \mu\text{m}$  radius ranged from 7% to 63%. The unusually large contribution that giant-size particles made to the scattering at visible wavelengths on March 28 and 29 is due to the increase in the concentration of these particles, presumably as a result of high wind speeds.

#### 5.1.4 Wind Speed Dependence

Figure 33 shows the HSS scattering coefficient as a function of 12-h average wind speed. The HSS values plotted in Fig. 33 have been normalized to a relative humidity of 75% to eliminate the effect of relative humidity changes on the variability of the scattering coefficient. The normalization was accomplished by computing the aerosol scattering coefficient as a function of relative humidity based on the particle growth model shown in Fig. 29, and then multiplying the observed HSS value by the model-predicted ratio of the scattering coefficient at 75% RH to that at the ambient relative humidity. Values of the scattering coefficient at a wavelength of  $5.0 \mu\text{m}$ , as calculated from the particle size distributions, are plotted as a function of wind speed in Fig. 34. These values of the scattering coefficient have also been normalized to 75% relative humidity. Considerable scatter is seen in the data despite the removal of the effects of relative humidity variations. Much of this scatter can be attributed to variations in particle number densities because of the variations in air mass history, atmospheric stability, and boundary layer depth. Variations in the amount of clouds in the boundary layer, and hence variations in aerosol scavenging and modification by clouds, may also contribute to

Table 3 — Percent Contribution to the Scattering Coefficient  
at 0.55  $\mu\text{m}$  by Particles in Given Size Ranges

Date (March 1983)	Time (GMT)	Particle Radius Range ( $\mu\text{m}$ )			
		<0.15	0.15-0.5	0.5-1.0	>1.0
13	1800	10.3	49.9	8.2	31.6
	2100	10.8	54.0	10.4	24.8
14	1600	19.1	47.3	8.3	25.3
	2000	12.6	54.1	7.6	25.7
	2300	15.3	54.4	6.2	24.1
15	1500	14.0	74.0	4.7	7.3
	1900	11.8	70.6	5.8	11.8
	2300	11.0	70.8	7.7	10.5
16	1500	4.6	68.6	11.4	15.4
	1900	6.0	57.4	13.9	22.7
17	1100	2.2	44.3	30.0	23.5
	1900	2.8	45.2	25.3	26.7
	2200	4.3	48.1	18.5	29.1
18	1100	4.7	47.4	13.5	34.8
	1900	7.5	38.4	11.2	42.9
	2200	10.1	44.1	12.9	32.9
19	0900	8.9	55.1	12.9	23.1
	1800	11.2	47.8	13.7	27.3
20	1000	6.0	55.3	16.4	22.3
	1600	8.0	53.4	17.2	21.4
21	1100	6.7	44.7	23.9	24.7
	1900	6.0	52.5	24.6	16.9
22	1000	3.2	45.9	30.5	20.4
	1400	5.3	42.6	29.0	23.1
	1900	5.9	56.1	18.4	19.6
23	0900	2.7	46.9	27.5	22.9
	2100	6.4	37.7	21.8	34.1
24	0900	5.0	45.9	20.9	28.2
	2100	2.7	52.0	25.5	19.8
25	1000	2.5	57.8	22.6	17.1
	2000	2.3	44.4	28.4	24.9
27	1600	4.7	32.0	24.3	39.0
28	1400	4.3	24.1	8.6	63.0
	2000	2.8	33.4	12.3	51.5
29	1100	2.4	23.4	13.3	60.9
	2000	4.7	48.1	15.1	32.1
30	1900	6.6	45.0	18.5	29.9

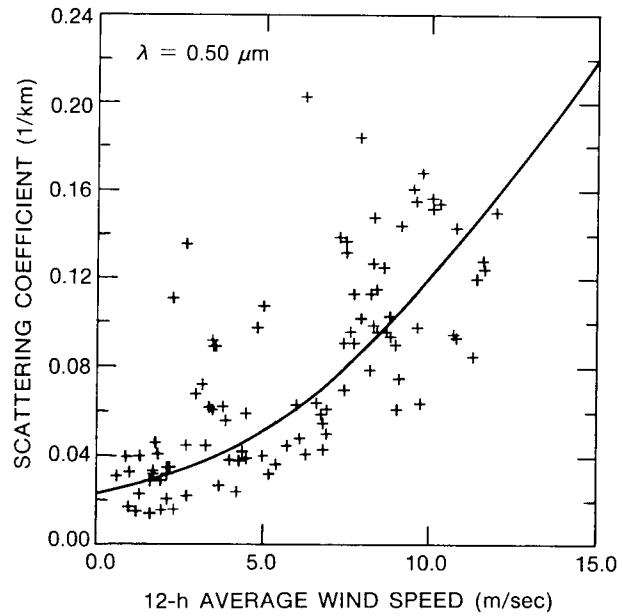


Fig. 33 — HSS scattering coefficient as a function of 12-h average wind speed. HSS values have been normalized to a relative humidity of 75%.

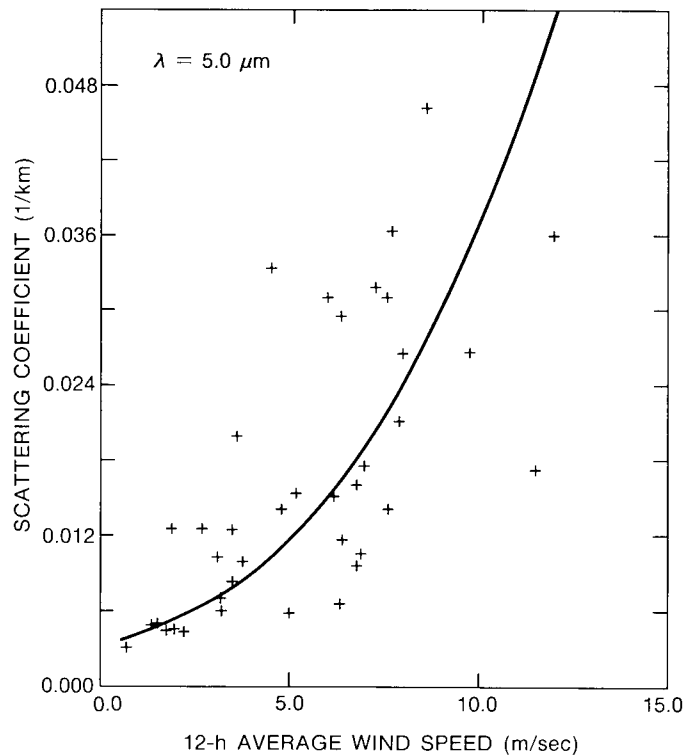


Fig. 34 — Calculated scattering coefficient at a wavelength of  $5.0 \mu\text{m}$  as a function of 12-h average wind speed

the scatter. Despite the scatter in the data, a dependence of the scattering coefficient on wind speed is clearly evident. The curves in Figs. 33 and 34 are eyeball fits through the data points and are an approximate description of the variation of the scattering coefficient caused by the wind speed changes alone. The data also indicate that the scattering coefficient for infrared radiation has a stronger dependence on wind speed than does the scattering coefficient at visible wavelengths. This suggests that the aerosol production mechanisms associated with the action of wind on the sea surface result in a greater percentage increase in the number of larger ( $r > 1.0 \mu m$ ) particles than in the number of particles smaller than  $0.5 \mu m$ .

It is important to bear in mind that the curves in Figs. 33 and 34 are just estimates of the true variation of the scattering coefficient with wind speed that would be observed if all other meteorological conditions were constant while wind speed varied. These curves could depart significantly from the true relation between scattering coefficient and wind speed if, for instance, the range of meteorological conditions (e.g., air mass type or stability) prevailing at the time of high wind speeds was significantly different from the range of conditions at low wind speeds.

## 5.2 Aerosol Optical Thickness

### 5.2.1 Method of Measurement

Aerosol optical thickness is the vertical integral of the aerosol extinction coefficient from the surface to the top of the atmosphere, and it is defined by

$$\tau_a(\lambda) = \int_0^{\infty} \beta_e(\lambda, z) dz. \quad (13)$$

Optical thickness was measured with a Volz portable multiwavelength sun photometer. The instrument is sighted at the sun and measures the direct solar irradiance in carefully selected narrow spectral intervals. The principle of operation of the sun photometer is based on Beer's law:

$$I(\lambda) = I_o(\lambda) \exp [-\tau(\lambda)M], \quad (14)$$

where

- $I(\lambda)$  is the observed intensity of solar radiation at wavelength  $\lambda$ ,
- $M$  is the relative air mass at solar zenith angle  $\phi$ , approximated by secant  $\phi$ ,
- $I_o(\lambda)$  is the instrument calibration and is the value of solar intensity the instrument would measure at the top of the atmosphere,

and

- $\tau(\lambda)$  is the total optical thickness due to aerosol particles and gases.
- $\tau(\lambda)$  may be expressed as

$$\tau(\lambda) = \tau_a(\lambda) + \tau_r \left[ \frac{P}{1013} \right] + \tau_o + \tau_g, \quad (15)$$

where

- $\tau_r$  is the Rayleigh optical thickness at a sea level pressure of 1013 mbar,
- $P$  is atmospheric pressure,
- $\tau_o$  is the ozone optical thickness

and

$\tau_g$  is the optical thickness caused by absorption of solar irradiation by minor atmospheric gases, notably  $NO_2$ .

The error incurred in the approximation  $M = \secant \phi$  is less than 4% for  $\phi < 80^\circ$  and is negligible at small zenith angles. Combining Eqs. (14) and (15) gives

$$\tau_a(\lambda) = \frac{-1}{M} \ln(I/I_o) - \tau_R \left[ \frac{P}{1013} \right] - \tau_o - \tau_g \quad (16)$$

The values of  $\tau_R$  at the sun photometer wavelengths were taken from Frohlich and Shaw (1980). In the absence of independent observations of the vertical content of ozone, we used the typical midlatitude value of  $\tau_o = 0.0092$  and  $0.021$  at  $\lambda = 0.50$  and  $0.64 \mu m$ , respectively. Ozone absorption can be neglected at  $0.44$  and  $0.88 \mu m$  wavelengths. Further, since the measurements were made over the oceans we assumed that  $\tau_g = 0$ .

The sun photometer used on this cruise was a four-wavelength instrument with filters centered at  $0.44$ ,  $0.50$ ,  $0.64$  and  $0.88 \mu m$ . The bandwidth at halfpeak transmittance was less than  $0.02 \mu m$  for all filters.

The sun photometer was calibrated by the Langley method using data collected during the cruise on days with clear skies or only small amounts of scattered cumulus clouds. In the Langley method, a straight line is fitted to a plot of  $\ln[I(\lambda)]$  vs  $M$  for each wavelength. Extrapolation of these lines to  $M = 0$  yields the calibration value  $I_o(\lambda)$  for each wavelength. The calibration values used to compute aerosol optical thickness from Eq. (16) were obtained by averaging the  $I_o(\lambda)$  values from three Langley plots. As discussed by d'Almeida et al. (1983), only those Langley plots should be accepted that have a strong linearity as expressed as a correlation coefficient between  $\ln[I(\lambda)]$  and  $M$  greater than  $0.99$ . Figure 35 shows the Langley plots constructed from the sun photometer measurements made during the Atlantic cruise. These plots exhibit a correlation coefficient greater than  $0.993$ .

The measured value of the aerosol optical thickness is the sum of tropospheric and stratospheric components. The normal background value of the stratospheric aerosol optical thickness is sufficiently small that little error is usually incurred in assuming that the tropospheric aerosol optical thickness is equal to the total measured aerosol optical thickness. However, since the measurements were made during the period of March 1983, when the stratospheric component was considerably enhanced above its background level because of the eruption of the El Chichon volcano in late March and early April 1982, and since our primary interest is in the tropospheric component of the optical thickness, it was necessary to estimate the El Chichon contribution and subtract it from the measured optical thickness. Sun photometer measurements of the spectral optical thickness of the El Chichon eruption cloud in the stratosphere were made on NASA aircraft flights in late April and early May 1983 (Spinhirne and King, 1985). Based on these measurements, the stratospheric aerosol optical thickness at the time and latitudes of the cruise was estimated to be independent of wavelength in the visible part of the spectrum, and to range from  $0.08$  at  $30^\circ N$ , to  $0.07$  at  $20^\circ N$ .

### 5.2.2 Spatial Variation and Wavelength Dependence

Figure 36 shows the spatial variation of the tropospheric component of the aerosol optical thickness at each of the sun photometer wavelengths. The values plotted for each day are the average of from 3 to 9 hourly readings, except for that of 29 March, when only one reading was obtained (at 2200 GMT). Sun photometer measurements were made whenever possible. The cloud cover precluded measurements to be taken during the periods of 15 to 18 March and 25 to 28 March. The

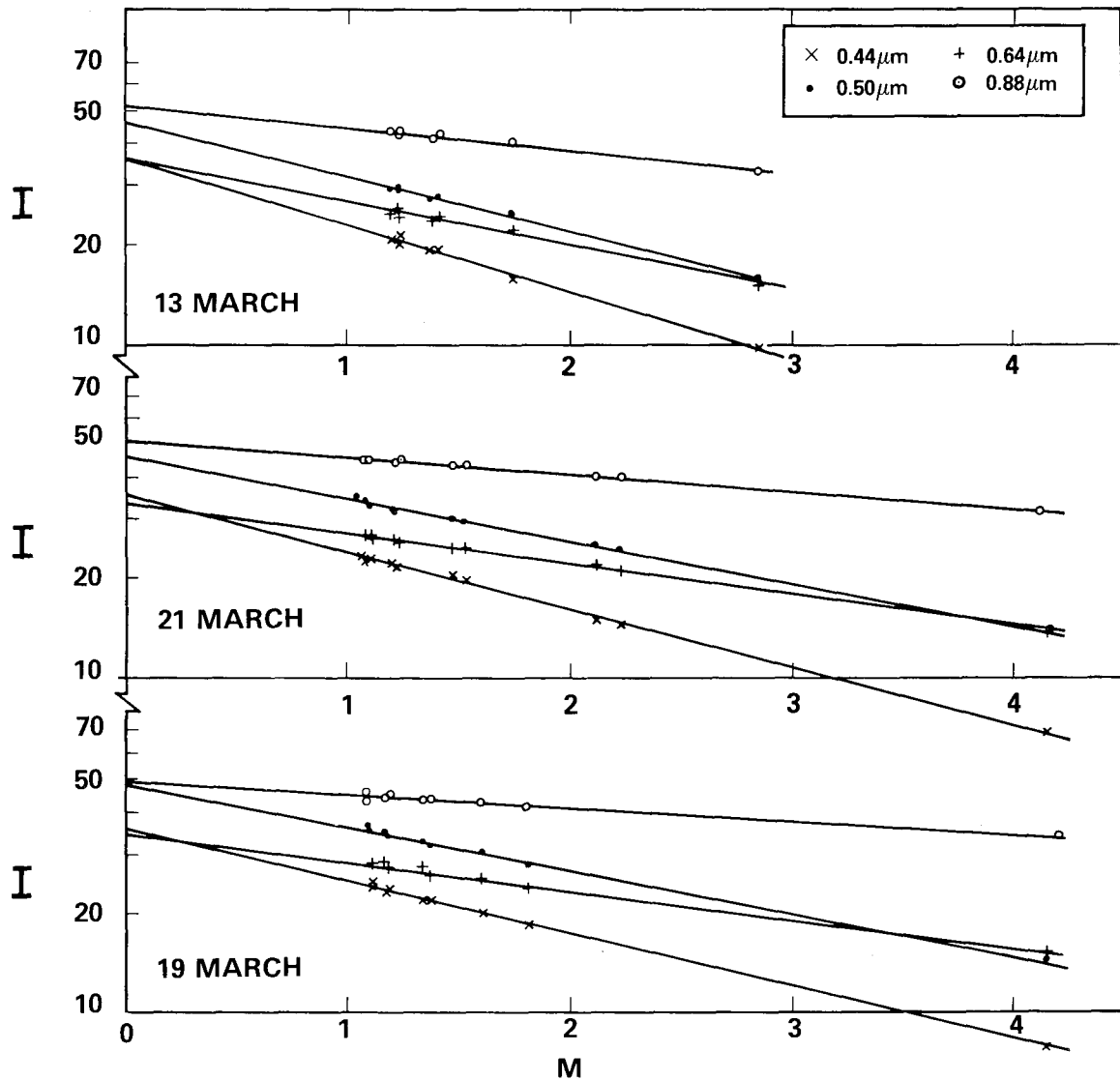


Fig. 35 — Langley plots constructed from sun photometer measurements made on the Atlantic cruise,  $M$  is the secant of the zenith angle.

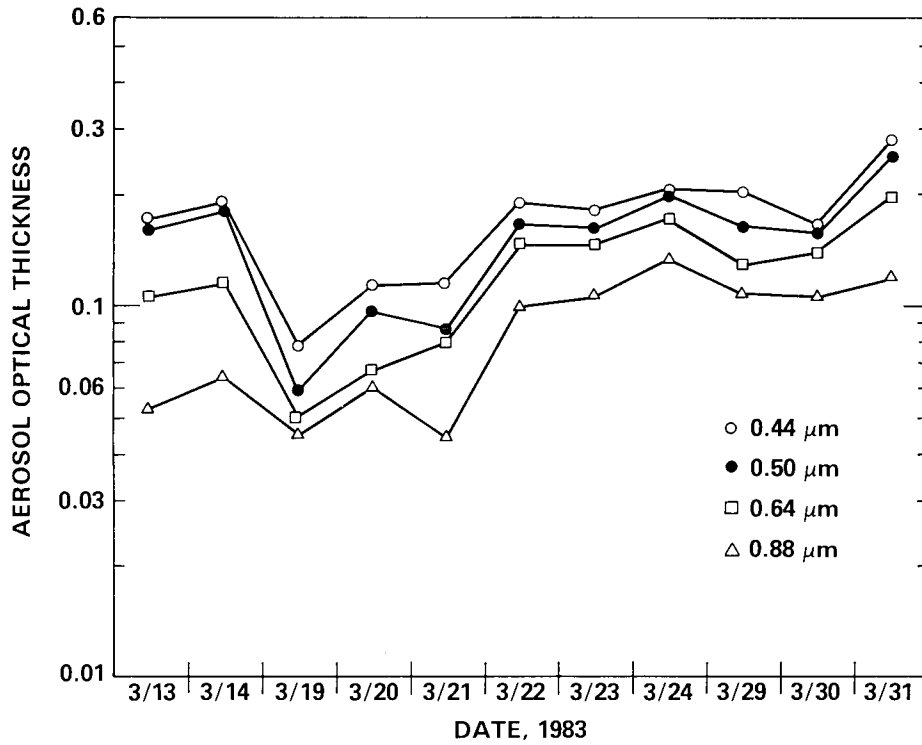


Fig. 36 — Variation of the tropospheric component of the aerosol optical thickness along the ship's track

calibration values obtained from the Langley plots of the cruise data were used to compute the optical thicknesses. The lowest values of  $\tau_a$  were measured between March 19 and 21. This was a period of low wind speeds and clean maritime air, as indicated by the air mass back trajectories that showed the air had resided over the ocean for at least 9 days. The lowest values of the aerosol scattering coefficient were also recorded during this period.

The dependence of  $\tau_a$  on wavelength in the visible and near-infrared spectral range can often be accurately described by the power-law expression (Angstrom, 1964)

$$\tau_a(\lambda) = \beta\lambda^{-\alpha}, \quad (17)$$

where wavelength is given in microns and  $\beta$  is the value of  $\tau_a$  at  $\lambda = 1 \mu\text{m}$ .  $\alpha$  and  $\beta$  are referred to as the Angstrom parameters. The exponent  $\alpha$  is closely related to the slope of the particle size distribution at radii greater than  $0.1 \mu\text{m}$  (Bullrich, 1964). Since the wavelength dependence of  $\tau_a$  is frequently described in the literature in terms of the Angstrom parameters, we calculated a least squares fit of Eq. (17) to the mean values of  $\tau_a(\lambda)$  vs  $\lambda$  for each day for which there was data. The spatial variation of the Angstrom parameters is shown in Fig. 37. The highest values of  $\alpha$  occurred on March 13 and 14 when the air flow was off the east coast of the United States. The slope of the particle size distribution in the range  $0.2$  to  $1.0 \mu\text{m}$  radius was steeper on 13 and 14 March than it was on any other day when optical thickness measurements were made, and it is consistent with the high values of the Angstrom exponent.

The average values of  $\alpha$  and  $\beta$  for the remote Atlantic (defined here as the portion of the cruise from 19 to 29 March) are 0.84 and 0.08, respectively. Tomasi and Prodi (1982) measured aerosol optical thickness over equatorial areas of the Indian Ocean northeast of the Seychelles islands in January and February, 1979, and they reported average values of  $\alpha$  and  $\beta$  of 0.60 and 0.19. Thus, in the



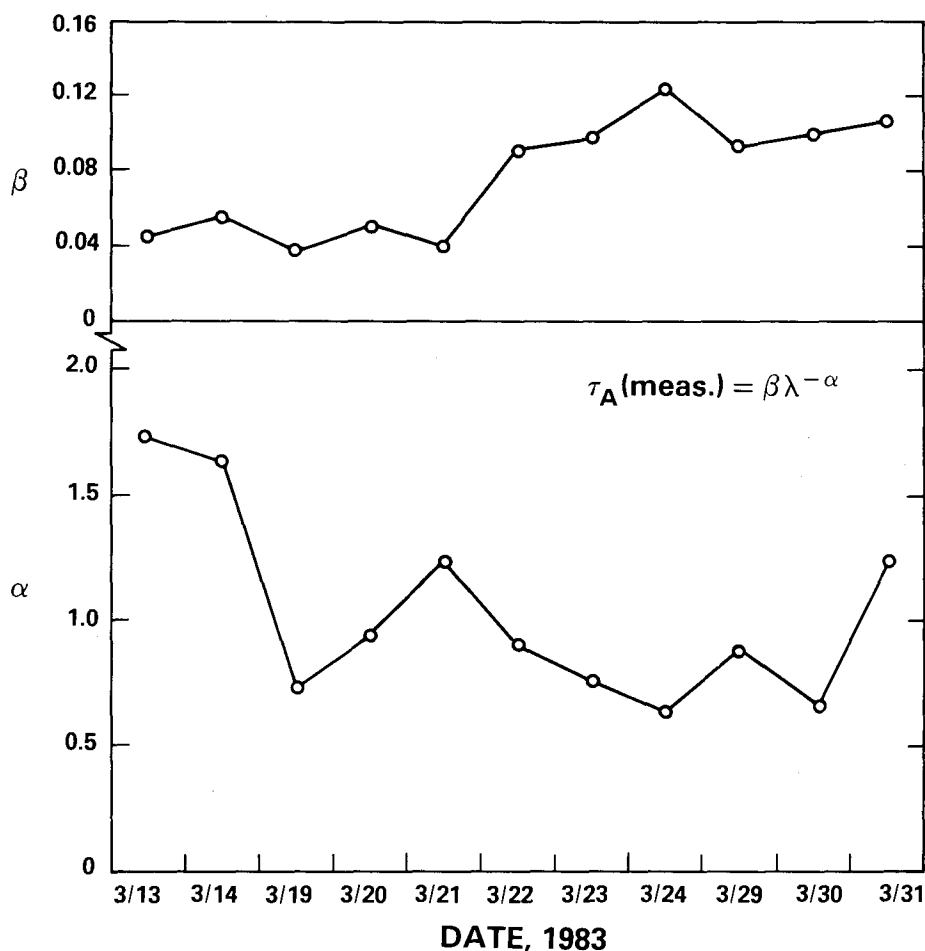


Fig. 37 — Variation of the Angstrom parameters  $\alpha$  and  $\beta$  along the ship's track

mean, the values of  $\tau_a$  measured in the remote subtropical areas of the North Atlantic on this cruise are about half as large as those measured over the Indian Ocean by Tomasi and Prodi (1982).

Our primary interest is in the value of  $\tau_a$  at a wavelength of  $0.5 \mu\text{m}$ . Figure 38 shows the spatial variation of  $\tau_a$  at  $\lambda = 0.5 \mu\text{m}$  in greater detail than in Fig. 36. Although readings were taken hourly on a number of days, values are plotted at intervals of 2 h for clarity. A range of values of  $\tau_a$  is plotted for each time. The high values were computed by using the sun photometer calibration values obtained from the Langley plots of the cruise data. The low values were computed by using calibration values determined by the manufacturer, who recalibrated the instrument several months after the cruise. Thus, we feel confident that the correct values of  $\tau_a$  at  $\lambda = 0.5 \mu\text{m}$  lie within the range shown.

### 5.2.3 Comparison of Measured and Calculated Optical Thickness

It is generally believed that the marine boundary layer makes the major contribution to the tropospheric optical thickness over the Atlantic, except during episodes of Saharan dust transport. It is instructive, therefore, to compare the measured tropospheric optical thickness with the calculated optical thickness of the boundary layer. It is of particular interest to determine if the observed variation in the measured optical thickness can be explained by variations in the height and relative humidity of the boundary layer along with variations in the aerosol scattering (or extinction) coefficient at the surface.

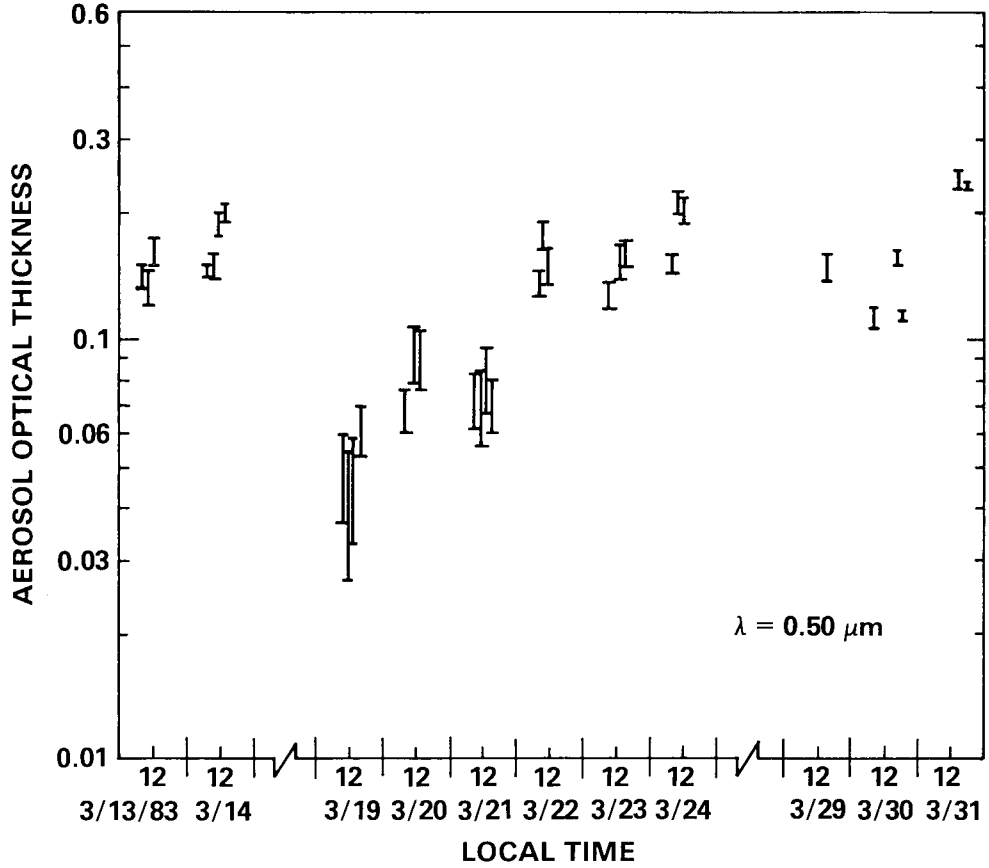


Fig. 38 — Variation of the aerosol optical thickness,  $\tau_a$ , at a wavelength of  $0.5 \mu\text{m}$ . The vertical bars show the range in  $\tau_a$  due to the uncertainty in the sun photometer calibration at this wavelength.

The aerosol optical thickness of the boundary layer is defined by

$$\tau_{a,B} = \int_{z_0}^H \beta_e(z) dz, \quad (18)$$

where  $H$  is the height of the boundary layer and  $z_0$  ( $\approx 10$  m) is the height of the shipboard observations. For the calculations, we express  $\tau_{a,B}$  as

$$\tau_{a,B} = \beta_e(z_0) \int_{z_0}^H \left[ \frac{\beta_e(z)}{\beta_e(z_0)} \right] dz, \quad (19)$$

where  $\beta_e(z_0)$  is the value of  $\beta_e$  at  $z = z_0$ . Thus,  $\tau_{a,B}$  is the product of the extinction coefficient at the surface and the integral of the normalized extinction coefficient,  $\beta_e(z)/\beta_e(z_0)$ , over the depth of the boundary layer. The vertical profile of  $\beta_e(z)/\beta_e(z_0)$  is determined by the profile of relative humidity, the concentration of particles as a function of height, and the dependence of particle size and refractive index on relative humidity.

Because of the variable weather conditions during the Atlantic crossing, the boundary layer varied from being well defined, with the relative humidity decreasing sharply from its peak value to below 30% over a distance of 15 to 30 m at the base of the overlying inversion, to being less well

defined with the relative humidity decreasing from its peak value to 50% over a distance of 600 m. For these calculations, we define the top of the boundary layer to be the height at which the relative humidity decreases to its value at the surface after reaching its peak value.

The vertical profiles of  $\beta_e(z)/\beta_e(z_0)$  needed to calculate  $\tau_{a,B}$  were determined by combining the profiles of relative humidity from the soundings with the calculated values of aerosol extinction as a function of relative humidity. Aerosol extinction as a function of relative humidity was calculated from the measured aerosol size distribution at the surface and the model of particle size and refractive index as a function of relative humidity already described in Section 5.1.1. The atmosphere was assumed to be well mixed from the surface up to the height of maximum relative humidity, and total particle concentrations were assumed to be constant with height, i.e., the aerosol size distribution at a fixed relative humidity was assumed to be independent of height in this portion of the boundary layer. However, between the height of maximum relative humidity and the top of the boundary layer, particle concentrations were arbitrarily assumed to decrease linearly with height to 50% of the surface concentrations at the top. Figure 39 shows several of the computed profiles of the normalized extinction coefficient. The integral in Eq. (19), which we denote by  $\zeta$ , was evaluated from the profiles of  $\beta_e(z)/\beta_e(z_0)$ . Thus,  $\tau_{a,B} = \beta_e(z_0)\zeta$ . The values of  $\beta_e(z_0)$  at  $\lambda = 0.50 \mu\text{m}$  were obtained by multiplying the measured values of  $\beta_s(z_0)$  at a wavelength dependence of  $\lambda_1$  by the ratio  $\beta_e(\lambda = 0.50)/\beta_s(\lambda = \lambda_1)$ . This ratio was determined from Mie-theory calculations of the wavelength dependence of  $\beta_s$  and  $\beta_e$  by using the measured particle size distributions at the surface.  $\lambda_1 = 0.475 \mu\text{m}$  for the HSS visibility meter and  $0.55 \mu\text{m}$  for the MRI integrating nephelometer. Although the HSS uses a light source at  $0.88 \mu\text{m}$ , it was calibrated against a nephelometer operating at  $\lambda = 0.475 \mu\text{m}$  and is assumed to give  $\beta_s$  at  $0.475 \mu\text{m}$ .

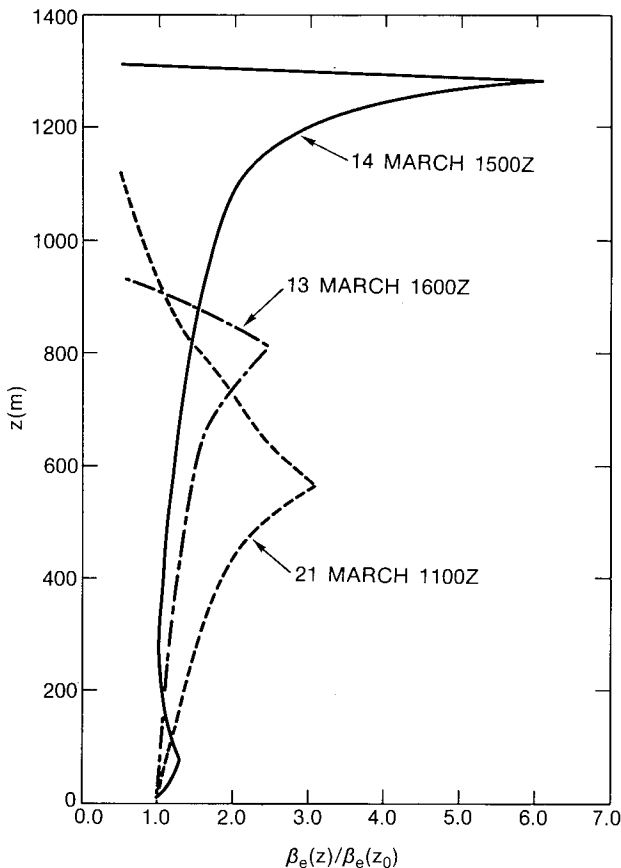


Fig. 39 — The computed profile of the normalized extinction coefficient,  $\beta_e(z)/\beta_e(z_0)$ , for three selected times

Values of  $\tau_{a,B}$  were calculated for 14 times between 13 and 30 March, when the optical thickness was measured within about 1 h of a radiosonde ascent. Also,  $\tau_{a,B}$  was calculated once on March 30 and again on March 31, when the elapsed time between the sun photometer measurement and the sounding was more than 2 h.

Table 4 lists each time  $\tau_{a,B}$  was calculated, the measured values of  $\tau_a$  at these times, the time of the nearest sounding, the boundary layer heights, the calculated values of  $\zeta$ , and the measured values of  $\beta_s(z_o)$ .

Figure 40 is a plot of the variation of  $\tau_a$  and  $\tau_{a,B}$  along the cruise track. Note that the measured and computed values of optical thickness track each other quite well. The correlation coefficient between  $\tau_a$  and  $\tau_{a,B}$  is 0.85 when HSS data are used to calculate  $\tau_{a,B}$  and 0.82 when MRI data are used. These results indicate that the spatial variation in the aerosol optical thickness of the troposphere over the subtropical Atlantic can be accounted for, to a large degree, by the combined effect of spatial variations in the depth, relative humidity, and aerosol characteristics of the boundary layer. Although there is a good correlation between the spatial variation of  $\tau_a$  and  $\tau_{a,B}$ , there is a significant discrepancy in the absolute magnitude of computed and measured optical thicknesses. The measured value of  $\tau_a$  is about twice the value of  $\tau_{a,B}$  computed from the HSS scattering coefficients and three to four times the value of  $\tau_{a,B}$  computed from the MRI values of the scattering coefficient.

Table 4 — Values of  $H$ ,  $\zeta$  and  $\beta_s(z_o)$  at the Times for Which the Boundary Layer Optical Thickness Was Computed

Date (March 1983)	Time of Sounding (GMT)	Time of $\tau_a$ (meas) (GMT)	$\tau_a$ (meas)	H (km)	$\zeta$ (km)	$\beta_s(z_o)$ ( $\text{km}^{-1}$ )	
						$\beta_s(\text{MRI})$	$\beta_s(\text{HSS})$
13	1528	1600	0.133	0.95	1.32	0.030	0.085
14	1455	1500	0.150	1.32	2.09	0.018	0.024
	1948	2005	0.197	1.50	2.70	0.032	0.042
19	1512	1500	0.041	0.65	0.88	0.012	0.021
	1833	1800	0.050	0.70	0.92	0.008	0.014
20	1254	1400	0.091	1.30	1.95	0.014	0.026
	1617	1600	0.190	1.10	1.85	0.015	0.025
21	0943	1100	0.066	1.05	1.75	0.015	0.027
	1548	1600	0.080		1.351.68	0.019	0.029
22	0948	1100	0.157	0.95	1.44	0.030	0.062
23	1459	1500	0.153	0.65	0.89	0.038	0.086
	1802	1700	0.160	0.70	0.99	0.034	0.070
24	1454	1417	0.201	1.25	1.74	0.020	0.055
30	0930 <sup>a</sup>	0930	0.113	1.60	2.17	0.012	0.030
	1720 <sup>b</sup>	1720	0.157	1.25	1.97	0.022	0.071
31	1455 <sup>c</sup>	1455	0.240	0.90	1.32	0.071	0.118

<sup>a</sup>Humidity profile at 0930 GMT estimated from soundings at 1024 GMT.

<sup>b</sup>Humidity profile at 1720 GMT estimated from soundings at 1437 and 2003 GMT.

<sup>c</sup>Humidity profile at 1455 GMT estimated from sounding at 0845 GMT and from and from observed change from overcast to mostly clear skies.

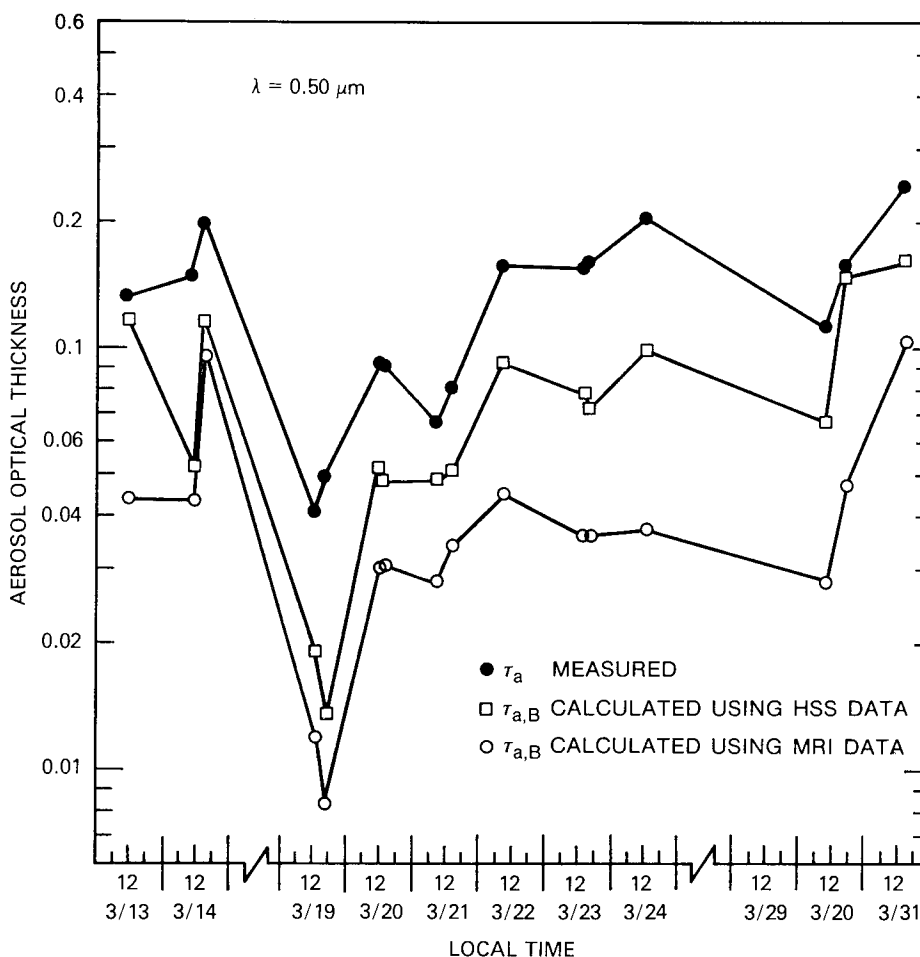


Fig. 40 — Comparison of the spatial variations of the measured tropospheric aerosol optical thickness,  $\tau_a$ , and the calculated optical thickness of the boundary layer,  $\tau_{a,B}$ , at a wavelength of  $0.5 \mu\text{m}$

There are several possible explanations for the discrepancy between the measured and computed optical thicknesses. First, there may have been a significant contribution to the optical thickness from the region of the troposphere above the boundary layer. However, this contribution would have to be highly correlated with the boundary layer optical thickness to explain the good correlation between the measured optical thickness and the calculated optical thickness of the boundary layer. A second possibility is that we have underestimated the El Chichon stratospheric contribution. This contribution, however, is independent of the boundary layer conditions. The use of a higher value for the stratospheric contribution would result in a poorer correlation between the measured optical thickness and  $\tau_{a,B}$ . A third explanation for the discrepancy is the occurrence of systematic errors in the measured values of the aerosol scattering coefficient at the surface.

## 6. CONCLUSIONS

The measured size distributions presented in this report are, to our knowledge, the most extensive and accurate measurements of the size distribution of submicron particles in the marine environment to date. The size distributions were supplemented by measurements of aerosol scattering coefficient and optical depth, extensive meteorological observations, balloon soundings, satellite coverage, calculated air mass trajectories, and aerosol chemistry. This support made it possible to correlate

changes in the size distribution with meteorological history, thus arriving at some unique interpretations of the mechanisms responsible for shaping the size distribution. Eight detailed case studies of the evolution in the size distributions that occurred under different meteorological conditions were presented, and possible mechanisms responsible for the changes were discussed in Section 4. Some of the more important observations and conclusions are the following.

1. As an air mass moves off the continents in the absence of clouds or precipitation, there is a rapid decay of small particles ( $r < 0.05 \mu\text{m}$ ) because of coagulation and growth by condensation of nonvolatile gas-phase reaction products on the small particles. This creates a size distribution with a strong peak (accumulation mode) in the  $0.05$  to  $0.08 \mu\text{m}$  radius range. The size distribution of these particles will often be modified by nonprecipitating clouds in the marine boundary layer before they are eventually removed by precipitation scavenging.

2. The cycling of aerosols through nonprecipitating clouds that are frequently present at the top of the marine boundary layer is a major factor in shaping the submicron aerosol size distribution. This cycling through clouds results in the repeated formation and evaporation of cloud droplets that form on the subset of particles called cloud condensation nuclei (CCN). During the cloud stage, trace gases are absorbed into the droplets where some are chemically converted into nonvolatile material that remains as part of the CCN after evaporation of the water. Also, a significant fraction of the smaller interstitial particles are captured by the cloud droplets, thus resulting in a decrease in the particles too small to be CCN. These processes cause an increase in the mass of CCN, and a minimum in the size distribution at the radius that separates interstitial and CCN portions of the size distribution.

3. The *background aerosol* found in the remote tropical MBL is not aged continental aerosol, but it is maintained by in situ formation of new particulate matter from the gas phase. (Particles larger than about  $0.5 \mu\text{m}$  are, of course, largely sea-salt aerosols generated at the sea surface.)

4. To maintain the small size portion of the size distribution ( $r < 0.05 \mu\text{m}$ ), there must be a source of small particles in the marine boundary layer (MBL). These particles are probably formed by heteromolecular homogeneous nucleation (or nucleation on cluster ions) at an average rate of 10 to 100 particles  $\text{cm}^{-3} \text{ day}^{-1}$  in the remote tropics. The exact chemistry of the nucleating species is unknown but undoubtedly involves gas-phase reaction products of very low volatility (such as  $\text{H}_2\text{SO}_4$ , MSA, and  $(\text{NH}_4)_2\text{SO}_4$ ). These small particles subsequently grow by condensation of additional gas-phase reaction products. There are known reaction pathways that lead from volatile gases of marine origin, such as DMS and  $\text{H}_2\text{S}$ , to species of low volatility.

5. A possible picture of the average life cycle of small marine particles in the remote tropics might be the following. New particles form at very small sizes at a rate of 10 to 100  $\text{cm}^{-3}$  per day. They grow to about  $0.04 \mu\text{m}$  in several days, at which time they become CCN and are cloud droplets during cloud cycles. On the average they participate in 10 to 20 nonprecipitating cloud cycles over a 3- to 10-day period, during which they grow to a size of about  $0.1 \mu\text{m}$  before being removed by precipitation scavenging in a rain cloud.

The particle size distributions were used to calculate the aerosol scattering and extinction coefficients in the MBL and, together with the soundings of relative humidity, were also used to calculate aerosol optical depth. These calculated values were then compared with measured values of the scattering coefficient and optical depth. An analysis of the measured and calculated aerosol optical properties leads to the following conclusions.

1. In general, measured and calculated values of the scattering coefficient track quite well. The calculated values are higher than the readings from the MRI integrating nephelometer but agree to within a factor of 2. The scattering coefficients measured with the HSS forward-scattering instrument correlated well with both the MRI and calculated values, except for periods when the wavelength dependence of the scattering coefficient was significantly weaker or stronger than the average. This leads us to conclude that the accuracy of the HSS readings depends on the particle size distribution and that the HSS will overestimate or underestimate the scattering coefficient depending on whether the slope of the size distribution at the time is significantly flatter or steeper than the slope of the size distribution(s) used to obtain the instrument's primary calibration. Variations in the scattering coefficient along the ship's track can be explained by changes in meteorological conditions and air mass history. At low wind speeds, the scattering coefficient in air that has resided over the ocean for at least 10 days is about  $0.01 \text{ km}^{-1}$ .

2. The calculated dependence of the aerosol extinction coefficient on wavelength ranged from weak to strong, depending on the relative concentration of large to small particles. The ratio of the extinction coefficient at  $0.5 \text{ }\mu\text{m}$  wavelength to that at  $8 \text{ }\mu\text{m}$  ranged from 13.5 following 36 h of wind speeds below  $2.0 \text{ m s}^{-1}$  to 1.5 following 4 days of wind speeds in the range of 7 to  $12 \text{ m s}^{-1}$ .

3. The contribution to the scattering coefficient at  $0.55 \text{ }\mu\text{m}$  from particles larger than  $1.0 \text{ }\mu\text{m}$  ranged from about 10% to 60%.

4. When the effects of relative humidity fluctuations on the variability of the scattering coefficient were removed by normalizing the values to a constant relative humidity, the scattering coefficients at visible and infrared wavelengths showed a significant dependence on wind speed. In the mean, the scattering coefficient at  $0.5 \text{ }\mu\text{m}$  wavelength increased by about a factor of 5 with an increase in the 12-h average wind speed from 2 to  $12 \text{ m s}^{-1}$ . The calculated scattering coefficient at  $5.0 \text{ }\mu\text{m}$  increased by a factor of 10 over the same range of wind speed.

5. The measured values of tropospheric optical thickness ranged from 0.04 to 0.25 at a wavelength of  $0.5 \text{ }\mu\text{m}$ . The Angstrom power law,  $\tau_a(\lambda) = \beta\lambda^{-\alpha}$ , was used to describe the wavelength dependence of the aerosol optical thickness. The exponent  $\alpha$ , which is directly related to the slope of the particle size distribution, was found to be higher near the east coast of the United States than over the remote areas of the Atlantic. The average values of  $\alpha$  and  $\beta$  for the transatlantic portion of the cruise were 1.03 and 0.075, respectively.

6. The optical thickness of the boundary layer was calculated from the value of the scattering coefficient at the surface and the boundary layer height and relative humidity profile obtained from balloon soundings. We assumed that the boundary layer was well mixed and that aerosol concentrations were constant with height in the boundary layer. The optical thickness of the boundary layer was found to track the variation of the tropospheric optical thickness quite well. The correlation of spatial variation of the optical depth of the troposphere over the Atlantic Ocean can, to a large degree, be accounted for by variations in aerosol extinction in the boundary layer. This, of course, would not be true during the times when dust comes from the Sahara. Although there was a high correlation between changes in the optical thickness of the troposphere over the ocean and changes in the optical thickness of the boundary layer, the troposphere optical thickness was a factor of about 2 higher than the boundary layer optical thickness if the HSS values of the scattering coefficient at the surface are used to calculate the latter and a factor of about 4 higher if the MRI scattering values are used. At present it is difficult to explain how the measured and calculated optical thicknesses could be so highly correlated yet differ in magnitude by so much.

## 7. ACKNOWLEDGMENTS

This report is dedicated to the memory of Eugene J. Mack (1942-1986) who died suddenly on 18 October 1986. Gene participated in the 1983 cruise that is reported here as well as in a number of previous research cruises sponsored by NRL and other Navy organizations.

Gene was the head of the Atmospheric Sciences Section at Calspan Corporation where he worked on a number of Navy contracts that supported research on fog physics, aerosol physics, atmospheric chemistry, and general meteorology. Over the years since the early 1970s, the work he directed was supported by the Office of Naval Research, Naval Research Lab, Naval Air Command, Naval Ocean Systems Command, Naval Environmental Prediction Research Facility, and the Navy Postgraduate School.

Gene was a hard worker whose vast field of experience had given him outstanding insight into meteorological processes. He was personable, cooperative, and had a good sense of humor. He is sorely missed by his friends at NRL, his wife, his four children, his colleagues at Calspan, and many others.

We thank Roger Helvey for providing the balloon soundings that were extremely useful in establishing the depth of the marine boundary layer and the thickness of the stratus cloud decks when they were present. We also thank Joyce Harris of the NOAA for the trajectory analysis used to establish the history of the air mass encountered during the cruise.

Partial support for this research was provided by ONR, Code 12, Dr. Paul Twitchell.

## 8. REFERENCES

- Andreae, M.O. and H. Raemdonck, (1983), "Dimethylsulfide in the surface ocean and the marine atmosphere: A global view," *Science*, **221**, 744-747.
- Andreae, M.O., R. Ferek, F. Bermond, K.P. Byrd, R.T. Engstrom, S. Hardin, P.D. Houmers, F. LeMarrec, and H. Raemdonck, (1985), "Dimethylsulfide in the marine atmosphere," *J. Geophys. Res.*, **90**, 12891-12900.
- Angstrom, A., (1964) "The parameters of atmospheric turbidity," *Tellus*, **16**, 64-75.
- Bates, T.S., J.D. Cline, R.H. Gammon, and S.R. Kelley-Hanson, (1987) "Regional and seasonal variations in the flux of oceanic dimethylsulfide to the atmosphere," *J. Geophys. Res.*, **92**, 2930-2938.
- Blanchard, D.C., (1983), "The production, distribution, and bacterial enrichment of the sea-salt aerosol," In *Air-Sea Exchange of Gases and Particles* Ed. P.S. Liss and George Slinn. NATO ASI Series C. Mathematical and Physical Sciences No. 10E. D. Reidel Publ. Co.
- Bullrich, K., (1964), "Scattered radiation in the atmosphere and the natural aerosol," *Advances in Geophysics*, **10**, 99-200.
- d'Almeida, G.A., R. Jaenicke, P. Roggendorf, and D. Richter, (1983), "New sunphotometer for network operation. *Appl. Opt.*, **22**, 3796-3801.
- Dave, J.V., (1968), "Subroutines for computing the parameters of electromagnetic radiation scattered by a sphere," IBM Palo Alto Scientific Center Report 320-3237.
- Dinger, J.E., H.B. Howell, and T.A. Wojciechowski, (1970), "On the source and composition of cloud condensation nuclei in the subsident air mass over the North Atlantic. *J. Atmos. Sci.*, **27**, 791-797.
- Fitzgerald, J.W., (1973), "Dependence of the supersaturation spectrum of CCN on aerosol size distribution and composition," *J. Atmos. Sci.*, **30**, 628-634.



- Fitzgerald, J.W. and W.A. Hoppel, (1982), "Measurement of the relationship between the dry size and critical supersaturation of natural aerosol particles," *Idojaras* (J. Hungarian Meteor. Service), **86**, pp. 242-248.
- Fitzgerald, J.W. and W.A. Hoppel, (1984), "Equilibrium size of atmospheric particles as a function of relative humidity: calculations based on measured aerosol properties," In *Hygroscopic Aerosols*, L. Ruhnke and A. Deepak (Eds.), A. Deepak Publishing, Hampton, VA.
- Fitzgerald, J.W., W.A. Hoppel, and M.A. Vietti, (1982), "The size and scattering coefficient of urban aerosol particles at Washington, DC as a function of relative humidity," *J. Atmos. Sci.*, **39**, 1838-1852.
- Friedlander, S.K. (1977), *Smoke, dust and haze*. Wiley-Interscience, New York.
- Frohlich, C. and G.E. Shaw, (1980), "New determination of Rayleigh scattering in the terrestrial atmosphere," *Appl. Opt.*, **19**, 1773-1775.
- Gathman, S.G., (1983), "Optical properties of the marine aerosol as predicted by the Navy aerosol model," *Optical Engineering*, **22**, 57-62.
- Giorgi, F., (1986), "A particle dry-deposition parameterization scheme for use in tracer transport models," *J. Geophys. Res.*, **91**, 9794-9806.
- Hanel, G., (1968), "The real part of the mean complex refractive index and the mean density of samples of atmospheric aerosol particles," *Tellus*, **20**, 371-379.
- Hanel, G., (1976), "The properties of atmospheric aerosol particles as functions of the relative humidity at thermodynamic equilibrium with the surrounding moist air," Eds. Landsberg and Mieghem, Academic Press, New York *Advances in Geophysics*, **19**, 77-188.
- Hanel, G. and M. Lehmann, (1981), "Equilibrium size of aerosol particles and relative humidity: New experimental data from various aerosol types and their treatment for cloud physics applications," *Contrib. Atmos. Phys.*, **54**, 57-71.
- Hatakeyama, S., K. Izumi, and H. Akimoto, (1985), "Yield of SO<sub>2</sub> and formation of aerosol in the photo-oxidation of DMS under atmospheric conditions," *Atmos. Environment*, **19**, 135-141.
- Hoppel, W.A., (1975), "Growth of condensation nuclei by heteromolecular condensation," *J. Rech. Atmos.*, **9**, 167-180.
- Hoppel, W.A., (1979), "Measurement of the size distribution and CCN supersaturation spectrum of submicron aerosols over the ocean," *J. Atmos. Sci.*, **36**, 2006-2015.
- Hoppel, W.A., (1987), "Nucleation in the MSA-water vapor system," *Atmospheric Environment*, **21**, 2703-2709.
- Hoppel, W.A., (1988), "The role of nonprecipitating cloud cycles and gas-to-particle conversion in the maintenance of the submicron aerosol size distribution over the tropical oceans," *Aerosols and Climate*. Ed. P. Hobbs and P. McCormick, 9-19.
- Hoppel, W.A. and G.M. Frick, (1986), "Ion-Aerosol Attachment Coefficients and the Steady-State Charge Distribution on Aerosols in a Bipolar Ion Environment," *Aerosol Science and Technology*, **5**, 1-21.
- Hoppel, W.A. and G.M. Frick, (1988), "Evidences of particle formation by homogeneous nucleation over the oceans," *Atmospheric Nucleation*. Ed. P.E. Wagner and G. Vali. Springer-Verlag, *Lecture Notes in Physics* series, 241-244.
- Hoppel, W.A. and G.M. Frick, (1989), "The nonequilibrium character of the aerosol charge distribution produced by neutralizers," Accepted for publication in *Aerosol Science and Technology*.
- Hoppel, W.A., G.M. Frick, and R.E. Larson, (1986), "Effect of nonprecipitating clouds on the aerosol size distribution in the marine boundary layer," *Geophys. Res. Lett.*, **13**, 125-128.
- Hoppel, W.A., J.W. Fitzgerald, and R.E. Larson, (1983), "Measurement of atmospheric aerosols: Experimental methods and results of measurements off the east coast of the United States," NRL Report 8703 (NTIS-ADA-130998).
- Hoppel, W.A., J.W. Fitzgerald, and R.E. Larson, (1985) "Aerosol size distributions in air masses advecting off the east coast of the United States," *J. Geophys. Res.*, **90**, 2365-2379.

- Hoppel, W.A., J.W. Fitzgerald, G.M. Frick, R.E. Larson, and B.J. Wattle, (1987), "Preliminary investigation of the role that DMS and cloud cycles play in the formation of the aerosol size distribution," NRL Report 9032 (NTIS-ADA-185002).
- Hoppel, W.A., R.E. Larson, and M.A. Vietti, (1984), "Aerosol size distributions at a site on the east coast of the United States," *Atmos. Environment*, **18**, 1613-1621.
- Junge, C.E. (1963), *Air Chemistry and Radioactivity*, Academic Press, New York.
- Larson, R.E., (1973), "Measurement of radioactive aerosols using thin plastic scintillators," *Nuc. Inst. and Meth.*, **108**, 467-470.
- Mack, E.J., B.J. Wattle, C.W. Rogers, (1980), "Fog Characteristics at Otis AFB, Massachusetts," Calspan Report No. 6655-M-1, Oct 1980.
- Mack, E.J., C.W. Rogers, and B.J. Wattle, (1986), "Marine aerosol characteristics in the subtropical North Atlantic and at North American coastal sites," Calspan Report No. 6890-M-1, December 1986. Arvin/Calspan Advanced Technology Center, P.O. Box 400, Buffalo, NY 14225.
- McCartney, E.J., (1976), *Optics of the Atmosphere*, Wiley, New York. 408pp.
- Mirabel, P. and J.L. Katz, (1974), "Binary homogeneous nucleation as a mechanism for the formation of aerosols," *J. Chem. Phys.*, **60**, 1138-1144.
- Monahan, E.C. and G. Mac Niocaill (eds.), (1986), *Oceanic whitecaps and their role in air-sea exchange processes*, D. Reidel, Galway Univ. Press. 294 pp.
- Parungo, F., J. Harris, B. Rosenwasser, and L. Ruhnke, (1984), "Analyses of aerosol and precipitation samples collected during a transatlantic research cruise," NOAA Tech. Memorandum ERL ESG-5.
- Pinnick, R.G. and H.S. Auvermann, (1979), "Response characteristics of Knollenberg light-scattering aerosol counters," *J. Aerosol Sci.*, **10**, 55-74.
- Pruppacher, H.R. and J.D. Klett, (1978), *Microphysics of Clouds and Precipitation*, D. Reidel, Boston.
- Pruppacher, H.R., (1986), "The role of cloud physics in atmospheric multiphase systems: ten basic statements," *Chemistry of Multiphase Atmospheric Systems*, Ed. W. Jaeschke, NATO ASI series, Springer-Verlag, Berlin.
- Reiss, H., (1950), "The kinetics of phase transitions in binary systems," *J. Chem. Phys.*, **18**, 840-848.
- Shettle, E.P. and R.W. Fenn, (1979), "Models for the aerosols of the lower atmosphere and the effects of humidity variations on their optical properties," Air Force Geophysics Laboratory Report TR-79-0214.
- Spinhirne, J.D. and M.D. King, (1985), "Latitudinal variation of spectral optical thickness and columnar size distribution of the El Chichon aerosol layer," *J. Geophys. Res.*, **90**, 10607-10619.
- Tomasi, C. and F. Prodi, (1982), "Measurements of atmospheric turbidity and vertical mass loading of particulate matter in marine environments (Red Sea, Indian Ocean, Somalian Coast)," *J. Geophys. Res.*, **87**, 1279-1286.
- Twomey, S., (1968), "On the composition of cloud nuclei in the northern United States," *J. Rech. Atmos.*, **3**, 281-285.
- Twomey, S., (1977), *Atmospheric Aerosols*, Elsevier, New York.
- Young, H.D., (1962), *Statistical Treatment of Experimental Data*. McGraw-Hill Book Company, New York, pp. 126-132.

## Appendix A

### RELATIONSHIP BETWEEN THE VARIOUS REPRESENTATIONS OF THE SIZE DISTRIBUTION

The most desirable way to exhibit the size distribution depends upon the application. In this report both the number and volume distributions are used. The number distribution  $n(r)$  is defined as the number of particles  $dN$  per unit radius  $dr$ .

$$n(r) = \frac{dN}{dr},$$

whereas the volume distribution is the amount of particulate volume per unit radius

$$\frac{dV}{dr} = \frac{4}{3} \pi r^3 \frac{dN}{dr} = \frac{4}{3} \pi r^3 n(r).$$

The volume distribution gives much more weight to the larger sizes and is, of course, related to the mass distribution ( $dM/dr$ ) through the density of the particle ( $dM/dr = \rho_p dV/dr$ ).

If these distributions are plotted as a function of radius on a linear plot, then the areas under the curves are related to the total number of particles, the total particulate volume, and total particulate mass, respectively.

Because of the large range in particle radius and concentration at different radii found in the atmosphere, the size distribution is usually plotted logarithmically.

The size distribution defined by the number of particles per unit of  $\log r$  is also commonly used.

$$\frac{dN}{d \left[ \log \left( \frac{r}{r_o} \right) \right]} = 2.30 r \frac{dN}{dr} = 2.30 r n(r),$$

where  $r_o$  is a constant.

To obtain  $dN/d(\log r)$  from  $n(r)$ , it is necessary to multiply  $n(r)$  by  $2.30 r$  (at each  $r$ ). If  $dN/d(\log r)$  is plotted against  $r$  on a log-linear graph, then the area under the curve is proportional to the number of particles. However,  $dN/d(\log r)$  is usually plotted logarithmically to compress the large range of  $dN/d(\log r)$  into a reasonable ordinate range. Likewise, the particulate volume distribution can be written as

$$\frac{dV}{d(\log r)} = 2.30 r \frac{dV}{dr} = 2.30 \frac{4}{3} \pi r^4 n(r).$$

The size distribution of atmospheric particles between about 0.05 to 5  $\mu\text{m}$  has often been approximated by the Junge (1963) size distribution given by

$$\frac{dN}{dr} \propto r^{-4}.$$

When this is the case,  $dN/d(\log r) \propto r^{-3}$ ,  $dV/dr \propto r^{-1}$ , and  $dV/d(\log r) \propto \text{constant}$ . The first three representations of the Junge distribution will have a decreasing absolute slope; the last one is constant with radius. It is clear that fewer ordinate decades are necessary to plot the latter distributions, if indeed the size distribution follows the Junge hypothesis.

Of the size distributions discussed above,  $n(r)$  gives the greatest emphasis to the smallest particles. We have chosen to plot  $n(r)$  for two reasons: (1) in this report the emphasis is on small particles, and  $n(r)$  gives the greatest weight to small particles; and (2) all our previous measurements have been presented in terms of  $n(r)$ , thus it is easy to compare these results with our earlier measurements.

In Section 3 we have also made extensive use of the volume distribution so that the structure at larger sizes could also be observed.

## Appendix B

### COMPARISON OF MEASUREMENTS WITH DIFFERENT INSTRUMENTS

During the 1983 cruise, a number of instruments were claimed to measure the same physical quantities. This is a desirable situation that invariably leads to a better understanding of the meaning and accuracy of the measurements. However, it does complicate the analysis since discrepancies must be understood, and the selection of one measurement over another must be justified. In this appendix we compare the measurements of the size distribution made with several different instruments, the aerosol scattering coefficient with two different instruments, and the total aerosol concentrations as measured with the Gardner counter and as obtained by integrating the size distribution.

#### B.1 Comparison of Size Distribution Measurements

*Instrumentation* — Size distribution data were obtained with five different instruments operating over the particle size range from 0.006 to 10  $\mu\text{m}$  radius. The NRL differential mobility analyzer (DMA) and Calspan's Thermal Systems Inc. (TSI), electrical aerosol analyzer (EAA) operated in the smallest size range ( $0.006 \mu\text{m} < r < 0.5 \mu\text{m}$ ). These instruments use the differences in the electrical mobilities of the particles to determine their size. The Particle Measurement Systems (PMS), Active Scattering Aerosol Spectrometer (ASAS), Model 300 and Calspan's Royco Particle Monitor size particles by their scattered light. Both instruments use near-forward scattering angles and have a double-valued region for which different size particles give the same response; however, the Royco uses white light and has only five channels, whereas the ASAS uses a He-Ne laser, has four partially overlapping ranges of 15 channels each and is claimed to cover the range from 0.0075 to 1.5  $\mu\text{m}$  radius. The Calspan impactor data spanned the range from  $r < 1.0 \mu\text{m}$  to  $r = 16 \mu\text{m}$  in even increments of 1.0  $\mu\text{m}$ . The droplet concentrations were corrected for the impactor collection efficiency. However since the smallest channel ( $r < 1.0 \mu\text{m}$ ) has no specified cutoff and has a collection efficiency almost 40 times less than that of the next larger interval, the accuracy in the smallest interval is poor. The number of particles with radius greater than 10  $\mu\text{m}$  was very small, and for the most part these data were not included in the analysis because of the poor counting statistics.

*Calibration of the PMS-ASAS* — The size of particles measured with the PMS ASAS did not agree with the size measured with the NRL DMA, so we elected to accept the NRL DMA as a standard against which to calibrate the ASAS. Because of the simplicity of the physical principles under which the DMA operates, and because it may be used as a particle classifier, transmitting only those particles that fall within a small mobility interval, we feel this is justified. The ASAS (fitted with the factory-supplied calibration insert) was placed in-line between the outlet of the DMA and the inlet of the associated thermal gradient chamber (which grows the particles large enough to be counted by an optical particle counter). Figure B1 is an example of data obtained from this comparison; the transmitted size and concentrations from the DMA are represented by the horizontal line near the top of the figure. The PMS ASAS data lie below the flat line representing the DMA transmitted radius interval and concentration. The transmission function of the DMA has a triangular shape as is observed by the PMS. The small peak at the lower right are the doubly charged particles of larger sizes. Calibration of the ASAS consisted of shifting the assignment of the size range from those of the factory calibrations shown, so that the peak was centered within the size range of the DMA channel. The factory calibration was performed with only two or three sizes of latex polystyrene spheres (1.59 refractive index). This calibration affected only the sizing and not the counting of the ASAS. No attempt

to check the calibration of the measured concentration (effective sampling volume) of the ASAS was made at this time. Particles used for the calibration include room air, particles formed by the irradiation of filtered room air with ultraviolet light, and particles produced by bubbling air through solutions of  $NaCl$ ,  $NH_4Cl$ , and  $K_2SO_4$ . The last three substances have refractive indices varying from 1.5 to 1.64. Very little refractive index dependence of ASAS sizing on these various materials was found in the size range of the comparison ( $r < 0.5 \mu m$ ). However, theory (Pinnick and Auvermann, 1979) predicts only a weak refractive index dependence over the index range used here for particles with radii less than  $0.4 \mu m$ . For larger sizes, the theory predicts a multivalued calibration curve, and this may contribute to the increased scatter of data at radii larger than about  $0.5 \mu m$ .

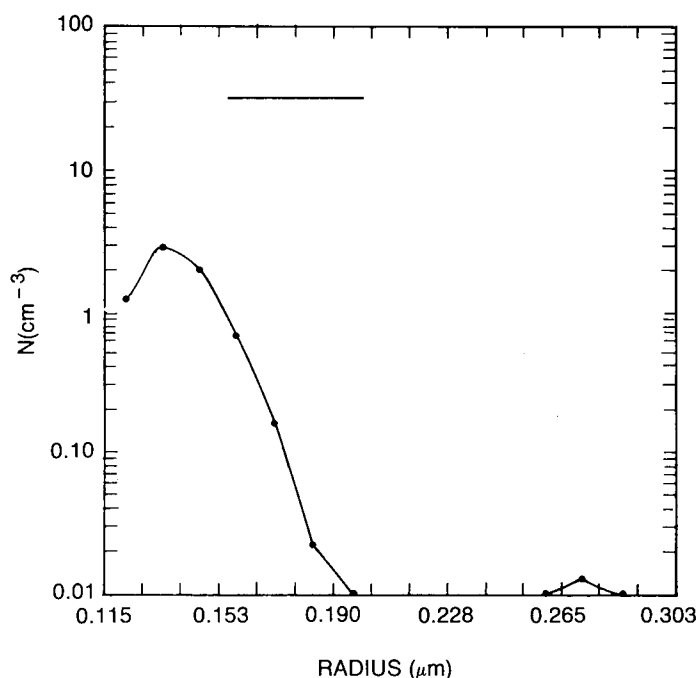


Fig. B1 — Intercomparison of NRL DMA (above) and PMS ASAS (below), which show the size intervals and relative concentrations

The PMS ASAS probe exhibits a strong dependence of concentration on relative wind velocity. This is not surprising, since the sample flow is controlled by a small muffin fan. Any change in wind speed changes the sample flow, resulting in an incorrect measure of the aerosol concentrations. This relative wind effect was observed when making shipboard measurements during which the ship was alternately turned into and against the wind. When the wind was directed into the sampling horn the ASAS data would overshoot that of the DMA; when the wind was to the rear of the instrument, the data were below that of the DMA.

A calibration of the wind dependence of the sample flow in the PMS ASAS was made in a NRL wind tunnel. A measurement of the sample flow velocity measured with a hot probe anemometer was made at the center of the sampling horn and plotted vs the tunnel wind speed (Fig B2). A curve fit was applied and the following expression was used to correct the PMS data.

$$U_p = U_o + .23 U_a + .0062 U_a^2,$$

where:

$U_o$  is sample flow velocity for zero wind, and is  $= 18.27 \text{ ft s}^{-1}$

$U_a$  is the ambient wind speed ( $\text{ft s}^{-1}$ ), and

$U_p$  is the net flow velocity ( $\text{ft s}^{-1}$ ) at the center of the horn.

Figure B2 shows that a  $30 \text{ ft s}^{-1}$  relative wind speed will produce an error of approximately 100%. It is not unusual to encounter relative wind speeds of this magnitude on board ships.

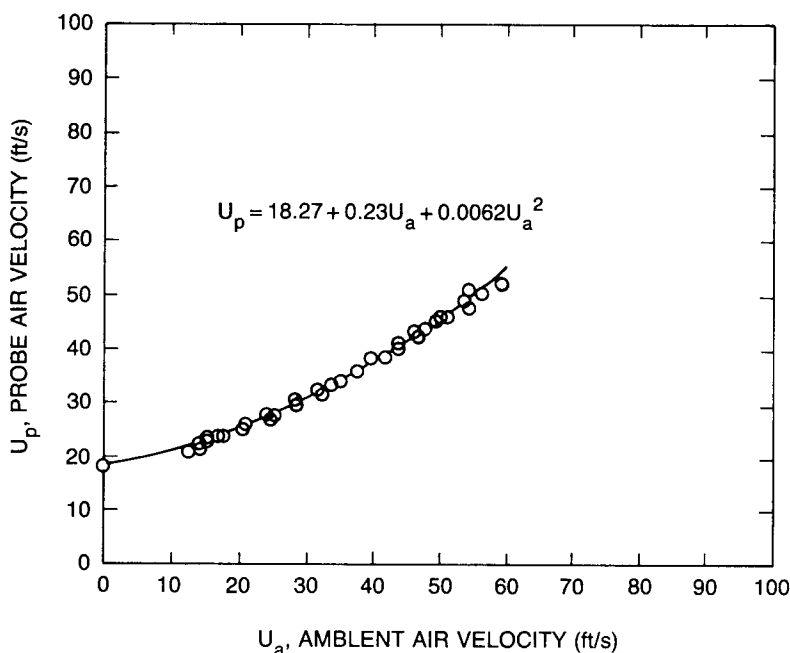


Fig. B2 — Dependence of the PMS probe sample airspeed vs ambient windspeed parallel to the sample flow axis

*Results* — Figure B3 is a representative example of the size distributions obtained with the DMA, ASAS, Royco, and impactor. The ASAS data (plotted after wind correction) tend to lie below the DMA within their overlap region except for the smallest channels of the smallest range, which give larger concentrations. If the smallest channels of the PMS ASAS were accepted as valid, then in many cases the total aerosol concentration implied would have been larger than the total condensation nucleus (CN) concentration. The low concentration of particles with  $r > 0.3 \mu\text{m}$  causes the scatter of these data points since there are only a few particles per channel; averaging over time or between adjacent channels reduces this effect. As stated above, the multivalued region of the calibration curve (Pinnick and Auvermann, 1979) at radii larger than  $0.5 \mu\text{m}$  may also contribute to the observed scatter.

The Calspan Royco data were consistently low, and we are not sure why this is so. This Royco was located inside the instrument shelter, and its sample was tapped off a larger tube with a high sample flow rate. The low count could be either a sampling or an instrument calibration problem.

The size distributions presented in Section 3 used only data from the NRL DMA and the Calspan impactor. As is evident from the above discussion, we view the NRL DMA data to be the most accurate data available for particles below  $0.5 \mu\text{m}$  radius. For the largest channel of the DMA ( $.30$  to  $.53 \mu\text{m}$ ) there is no correction for multiple charged particles of larger size (but the same mobility).

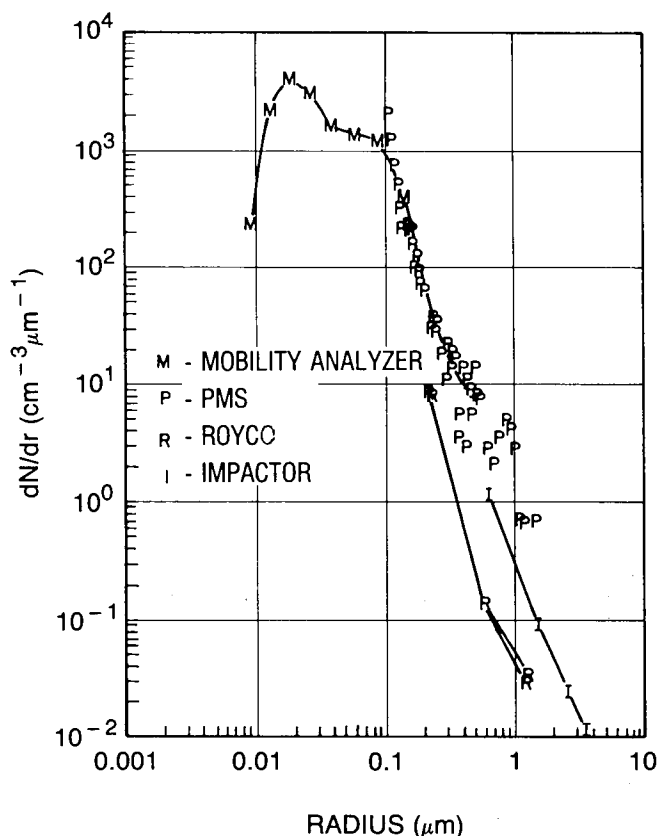


Fig. B3 — Size distributions obtained from NRL DMA (M), PMS ASAS (P), Impactor (I), and Royco (R) instruments

However in this size range, the distribution is decreasing so rapidly with increasing size that the number of multiple charged larger particles is negligible. For particles larger than 1  $\mu\text{m}$ , we consider the Calspan impactor data to give the most reliable results. For the reasons stated previously, there is a large uncertainty in the smallest impactor size range ( $r < 1 \mu\text{m}$ ). Despite this uncertainty, we have chosen to include the smallest impactor channel (plotted at .6  $\mu\text{m}$ ) in the presentation and to omit the Royco and the PMS ASAS data because of the problems discussed above.

## B.2 HSS and MRI Nephelometers

Throughout the cruise, measurements of the aerosol scattering coefficient were made with an MRI Integrating Nephelometer and an HSS Model VR-301 Visibility Meter. The MRI Model 1569 Integrating Nephelometer measures light scattered from aerosol as it is ventilated through an enclosed volume that is illuminated through a diffuser. A photomultiplier tube views the scattered light, and the geometry provides an integration of the scattering coefficient over a relatively wide scattering angle. An optical filter matches the spectral response of the instrument to that of the human eye. Absolute calibration of the instrument is accomplished by passing Freon-12 through the chamber. The absolute calibration was performed several times during the cruise. Checks of the *dark signal* zero and calibration provided on the control panel were done at least once a day.

The HSS Model VR-301 is a forward scattering instrument that measures the air in situ as it advects past the instrument. The light source is an infrared emitting diode with a peak at 880 nm. The scattering angle covers a range of 27° to 42°, and the sample volume is 400  $\text{cm}^3$ . The calibration of the instrument can be periodically checked by installing a plate containing a reference grid



(provided by HSS) in the active volume. It is our understanding that the primary calibration of the instrument was done by comparing the instrument's output voltage to an MRI integrating nephelometer in Calspan Corporation's 600-m<sup>3</sup> environmental chamber under a large number of controlled conditions. The MRI nephelometer used as a standard had a peak response at 474 nm. The justification for calibrating an instrument operating at one wavelength with another one operating at a different wavelength is not clear. Nevertheless, the tests "gave a linear response for the entire range of fogs and hazes which could be simulated in the test chamber" (HSS-TD-077, 5 October 1981). We therefore conclude that the HSS instrument, when using the recommended calibration, should give the same scattering coefficients as our MRI Model 1569 Integrating Nephelometer. This was our first experience with the HSS instrument; we calibrated it before and several times during the cruise. However, it became apparent that the windows on the instrument became dirty (most likely sea-salt deposit) and required frequent cleaning, especially during rough seas. Our procedure was to measure the signal with the calibration plate on, before and after cleaning the windows, and to apply a correction to the data between cleanings (assuming the windows degraded at a constant rate). A plot similar to that shown in Fig. B4, but with the HSS data offset (increased) by 0.11 km<sup>-1</sup>, was obtained when the HSS data were obtained by using the equation supplied by HSS. The source of this offset is unknown. It was not electronic because, when the light source and receiver were blocked off following the procedure specified by HSS, the reading obtained by the HSS-supplied equation was zero. We suspect that there may have been some reflection of the light off some nearby surface which caused an offset not related to aerosol scattering. During our stop in the Canary Islands, the HSS instrument was turned around so that the active volume was behind the supporting post instead of in front of the post. The rationale for this change was that the windows were then more protected from the incident winds and would require less cleaning. After this change was made, the offset was greatly reduced, thus leading us to the belief that the offset was caused by spurious reflections off nearby surfaces.

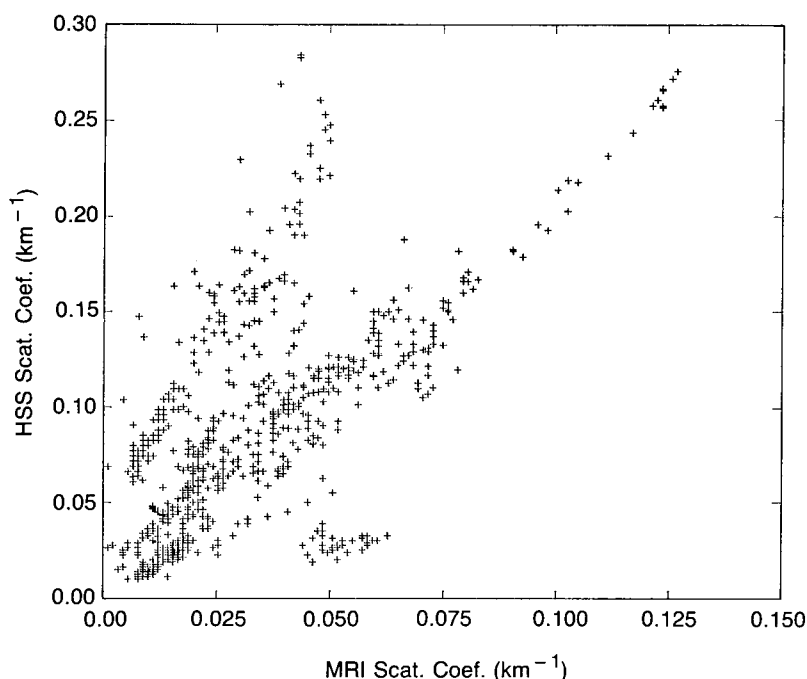


Fig. B4 — Correlation of scattering coefficients obtained simultaneously from MRI and HSS instruments

Figure B4 shows the scatter plot of the HSS readings vs the MRI readings obtained during the Charleston South Carolina to Canary Islands leg of the cruise after all known periods of rain and spray were removed. Rain and spray were seen by the HSS but not by the MRI. The plot appears to have two branches. The upper branch occurred during the period of 26 March to 29 March. On 26 March, there was a period of high seas and spray caused by the bow of the ship dipping into the waves. The windows of the HSS were not cleaned during this period, and when they were cleaned on 29 March, the calibration was more than 50% low. A correction was made to the data; however, the accuracy of this correction is doubtful, and the effect of sea-salt on the windows during this period of high and fluctuating relative humidity makes the validity of these readings questionable. If the data from 1200 GMT on 26 March until 1500 GMT on 29 March are removed, then the plot shown in Fig. B5 is obtained. The scatter is reduced but the slope is two instead of one. A slope of about two was also obtained during the Canary Islands to Scotland leg of the cruise.

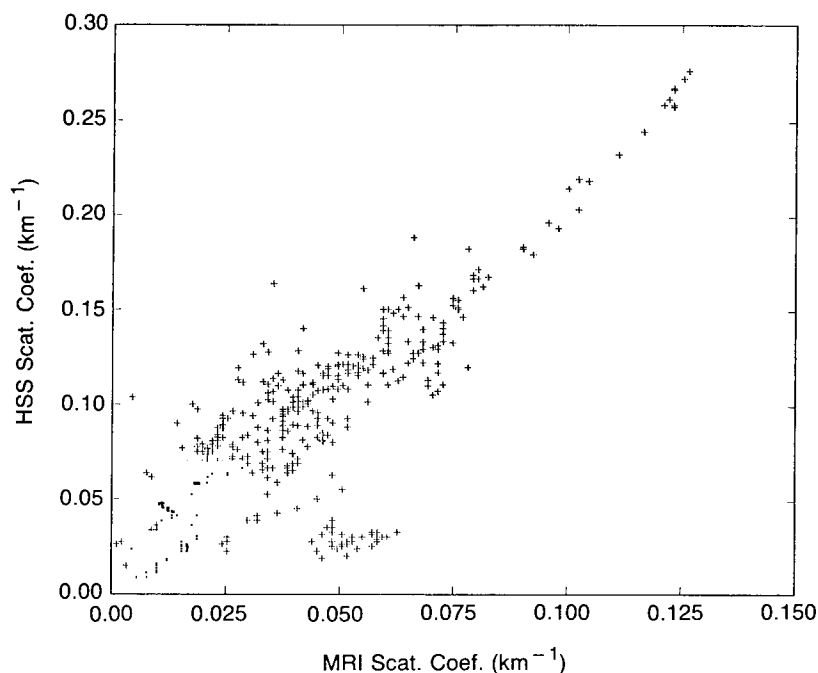


Fig. B5 — Scattering coefficient correlation of Fig. B4 after questionable data are removed

The large values of the scattering coefficient, (MRI values above about  $0.1 \text{ km}^{-1}$ ) occurred on 24 and 25 March, during the Saharan dust event. The cluster of points representing low HSS values at about  $0.05 \text{ km}^{-1}$  on the MRI scale occurred on 15 March during the period of low relative humidity.

*Evaluation* — Electronically the HSS is a very reliable instrument. Repairs were not required, even though we have now operated it on several field expeditions under adverse conditions. However, it does require almost daily calibration and window cleaning. Since its sample volume is external, it sees rain and other large particles as well as aerosols that are too large to negotiate the plumbing into the MRI nephelometer. However these advantages are of little value, since we have serious questions regarding the HSS calibration. We have more confidence in the accuracy of the MRI nephelometer, however, there is some question as to whether or not the measurement is made at ambient relative humidity since the light source has a warming effect on the optical cavity. In our experience, the

MRI Models 1567 and 1569 have not proved to be very reliable when used for extended periods in the field. We have seldom completed a field measurement program without having one of the MRI nephelometers fail.

An experience subsequent to this cruise, where visibility measured with the HSS was compared to the ability of humans to observe black targets in fogs with visibility between 10 and 100 m, showed that the HSS accurately predicted the observed visibilities in these dense fogs.

### B.3 Comparison of the Gardner Counter Concentrations with the Total Concentrations Obtained by Integrating the Size Distribution

Hourly readings of the CN concentrations were made with the Gardner counter. These readings taken during the first leg of the 1983 cruise are shown in Fig. B6 by the solid line. Also shown are the total aerosol concentrations obtained by integrating the size distribution taken with the DMA. The two measurements tracked fairly well. The agreement was quite good when the concentrations were above about 1000 particles  $\text{cm}^{-3}$ . However, when the concentration dropped below 500  $\text{cm}^{-3}$ , the DMA concentrations were about half those of the Gardner counter. Since the Gardner counter depends on the light scattered by the activated particles, its sensitivity and calibration have a lower limit of several hundred particles  $\text{cm}^{-3}$ . The DMA uses single-particle counting and has very good sensitivity at these low concentrations. We therefore accept the integrated DMA concentration as the most reliable absolute measurement of CN when the concentration is low. However the Gardner counter is very valuable for giving quick readings and detecting the existence of pollution from our ship or other ships in the area. The DMA requires about 15 min to obtain a size distribution.

The Gardner counter operates at a much higher supersaturation than does the detector of the DMA, and thus it will detect smaller particles than will the DMA. If periods when large numbers of very small particles exist, then the Gardner counter reading should be larger than the integrated DMA concentration. This was observed to occur off the Iberian coast and is discussed in Section 3.5.

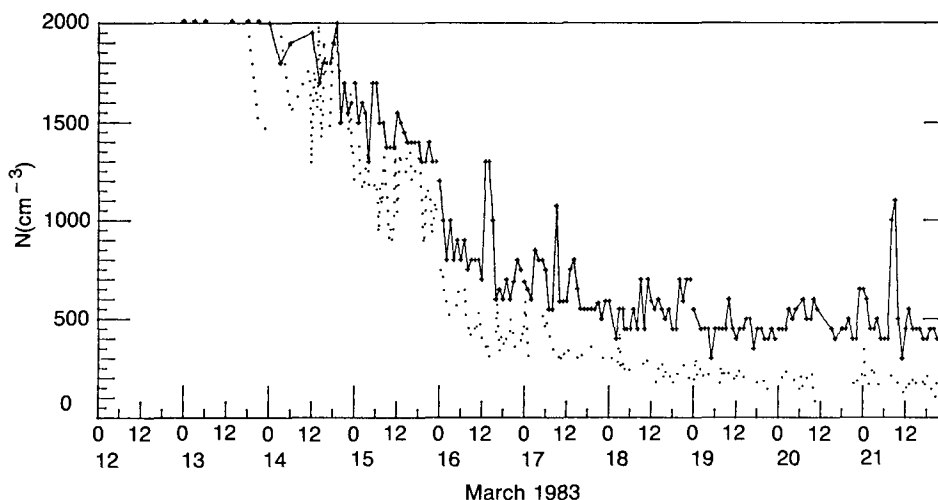


Fig. B6 — Aerosol particle concentrations obtained from Gardner counter (solid line) and NRL DMA (dots)



## Appendix C

### CCN SUPERSATURATION SPECTRA

The aerosol particles upon which cloud droplets form are called cloud condensation nuclei (CCN). Associated with each aerosol particle is a property called the critical supersaturation. When the environmental supersaturation reaches the critical supersaturation, the particle will be activated (heterogeneously nucleated) and grow rapidly to cloud droplet sizes. The concentration of particles as a function of their supersaturation is called the CCN supersaturation spectrum. The supersaturation spectrum is the aerosol description required when cloud microstructure (size and concentration of cloud droplets) is to be calculated. If all aerosol particles have the same chemical composition, then there is a unique relationship between the radius of the particle and its critical supersaturation.

For a particle composed of a pure electrolyte, the relationship between the dry radius  $r_o$  and critical supersaturation  $S$  can be written as [Fitzgerald and Hoppel, (1982) or Pruppacher and Klett, 1978]:

$$S = K r^{-3/2} \quad (C1)$$

where

$$K = \left[ \frac{4 A^3}{27 B} \right]^{1/2} \quad (C2)$$

and

$$A = \frac{4.33 \times 10^{-7} \sigma}{T} \quad (C3)$$

$$B = \nu \phi \left( \frac{M_w}{M_s} \right) \left( \frac{\rho_s}{\rho_w} \right), \quad (C4)$$

where  $\phi$  is the practical osmotic coefficient,  $\nu$  is the number of moles of ions formed by the dissociation of one mole of solute,  $M_w$  and  $M_s$  are the molecular weights of water and the solute, and  $\rho_w$  and  $\rho_s$  are the densities of water and the solute. If the particles are mixtures, then the expression for  $K$  is more complex. The case when the nuclei consists of insoluble material mixed with a single electrolyte has been considered by Fitzgerald (1973), where it is shown that if the particle is more than 50% soluble material, then using the value of  $K$  for the soluble material results in an error of about 40% in the derived value of the critical supersaturation. As the fraction of soluble material increases above 50%, this error decreases rapidly. Cases where the soluble component of the particles are a mixture of materials have been discussed by Hanel (1976) and Fitzgerald et al. (1982). Five different mixtures considered by Fitzgerald et al. had extreme values of  $K$  that differed by a factor of two. Since, in this report, we are dealing primarily with submicron particles that were formed over the ocean by gas to particle conversion, we would expect the particles to be fairly uniform in composition and not to contain insoluble material.

Direct measurements of  $K$  can be made by using the differential mobility analyzer as a classifier to transmit particles in a very small size range to a thermal gradient cloud chamber where the critical supersaturation can be measured. These measurements were first performed by Hoppel (1979) and later, 250 km off the east coast of the United States by [Fitzgerald and Hoppel (1982)]. The later measurements taken in air masses advecting off the east coast yielded values of  $K$  in the range of 2.08 to  $2.56 \times 10^{-11} \text{ cm}^{3/2}$ . These measured values are somewhat higher than we would expect for the remote oceanic regions where the chemical components of the submicron aerosol are most likely sulfur compounds. Sulfuric acid, ammonia sulfate, and MSA all have values of  $K$  that lie in the range of about 1.6 to  $2.0 \times 10^{-11} \text{ cm}^{3/2}$ .

Since the range of  $K$ s expected for the submicron part of the size distribution throughout the cruise is expected to be reasonably small (about  $\pm 20\%$  of the mean), converting the size distributions to supersaturation spectra using  $K = 1.9 \times 10^{-11} \text{ cm}^{3/2}$  should be quite acceptable for many purposes of evaluating the CCN activated at different cloud supersaturations. Converting the size distribution  $n(r)$  to a supersaturation spectrum  $n(S)$  by using Eq. (C1) yields

$$n(S) = - \frac{2}{3} \frac{r^{5/2}}{K} n(r). \quad (\text{C5})$$

The more commonly used supersaturation spectrum is the cumulative spectrum  $N(S)$  obtained by integrating Eq. (C5)

$$N(S) = \int_0^S n(S) dS. \quad (\text{C6})$$

The figures that appear in this appendix give the supersaturation spectra for all size distributions given in the Section 3 of this report. The supersaturation spectrum is calculated from the differential mobility analyzer data by using the equation

$$n(S) = \frac{\Delta n_i}{S_{i+1} - S_i}, \quad (\text{C7})$$

where  $\Delta n_i$  is the number of particles in the radius interval between  $r_i$  and  $r_{i+1}$ ; the corresponding critical supersaturations  $S_i$  and  $S_{i+1}$  are obtained using Eq. (C1). The exact meteorological conditions corresponding to each supersaturation spectrum can be obtained by reference to the corresponding size distribution, whose figure number is given in the caption. Figure C1 shows the correspondence between critical radius and supersaturation.

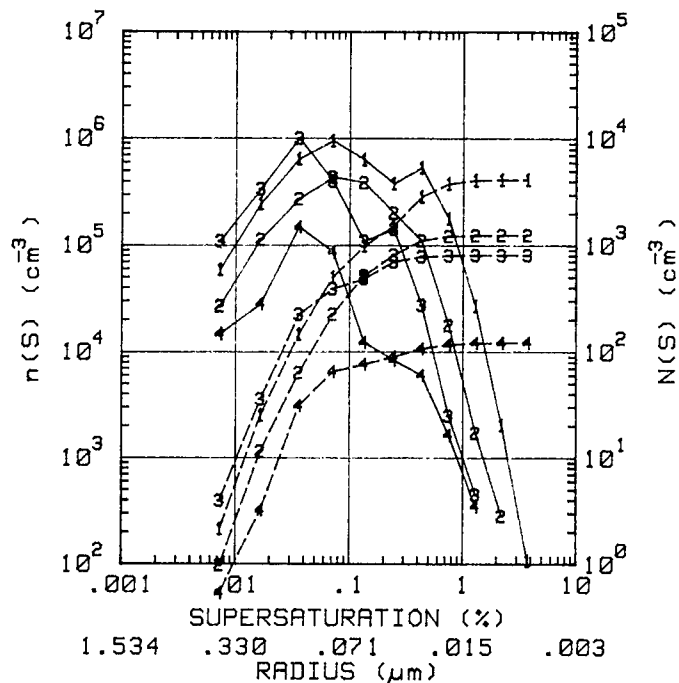


Fig. C1 — Supersaturation spectra for the size distributions of Fig. 7 solid lines are  $n(s)$ ; dashed lines are  $N(s)$ .

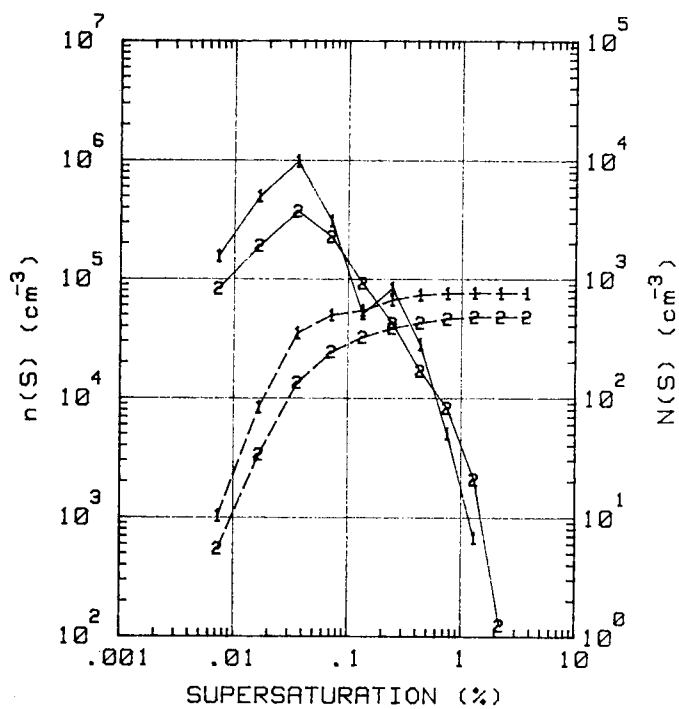


Fig. C2 — Supersaturation spectra for the size distributions of Fig. 11

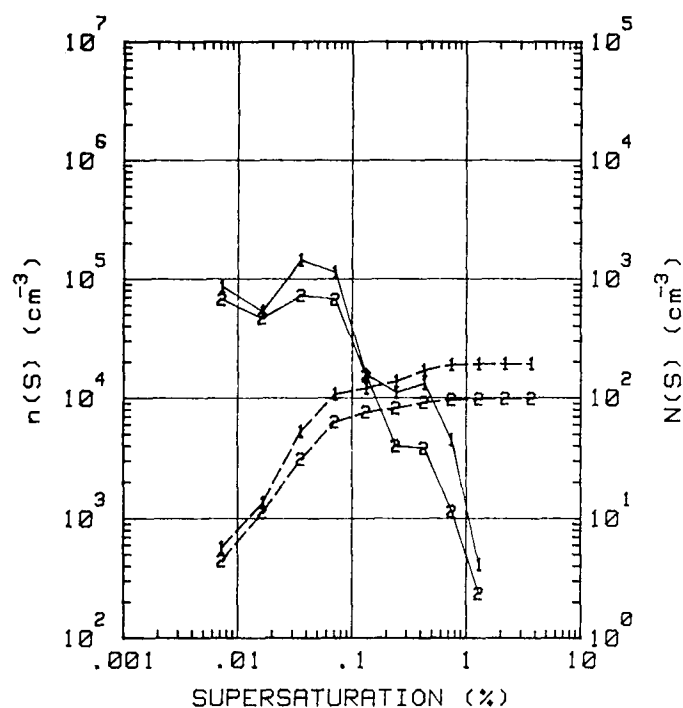


Fig. C3 — Supersaturation spectra for the size distributions of Fig. 12

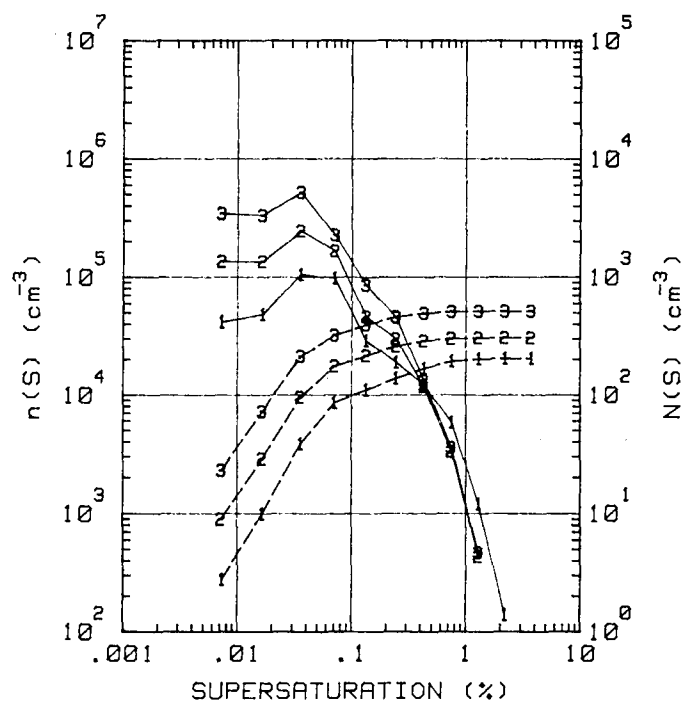


Fig. C4 — Supersaturation spectra for the size distributions of Fig. 13



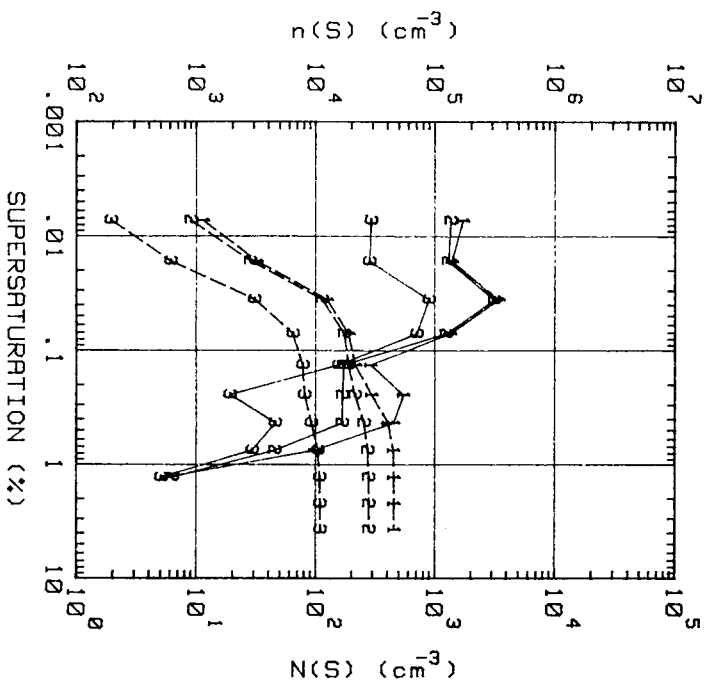


Fig. C5 — Supersaturation spectra for the size distributions of Fig. 15

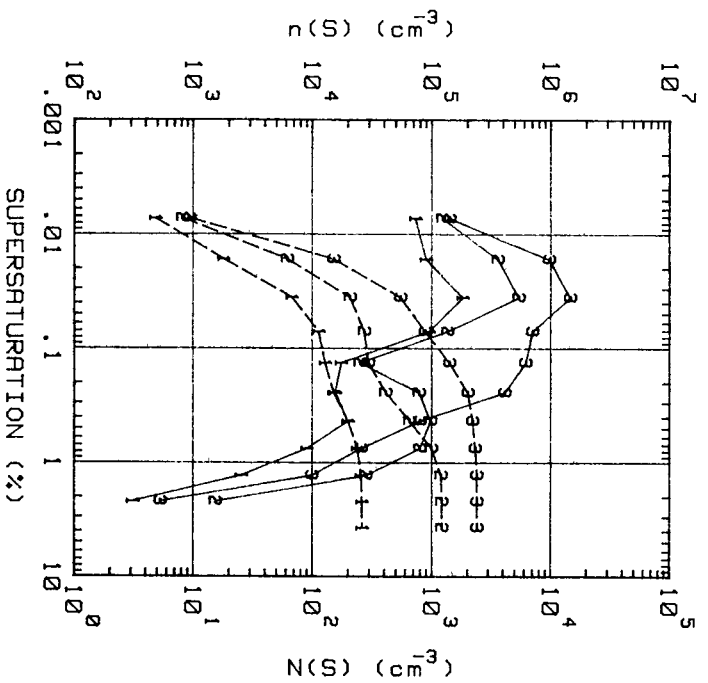


Fig. C6 — Supersaturation spectra for the size distributions of Fig. 19

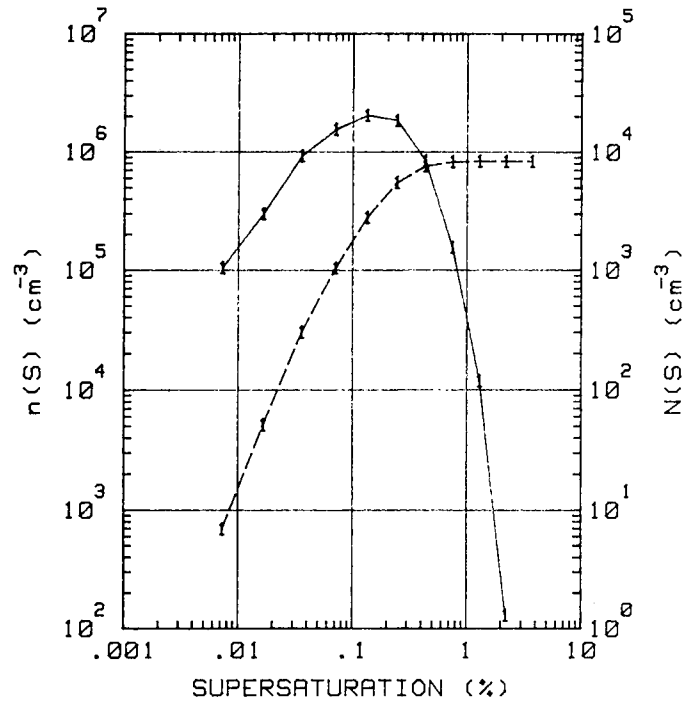


Fig. C7 — Supersaturation spectra for the size distributions of Fig. 21

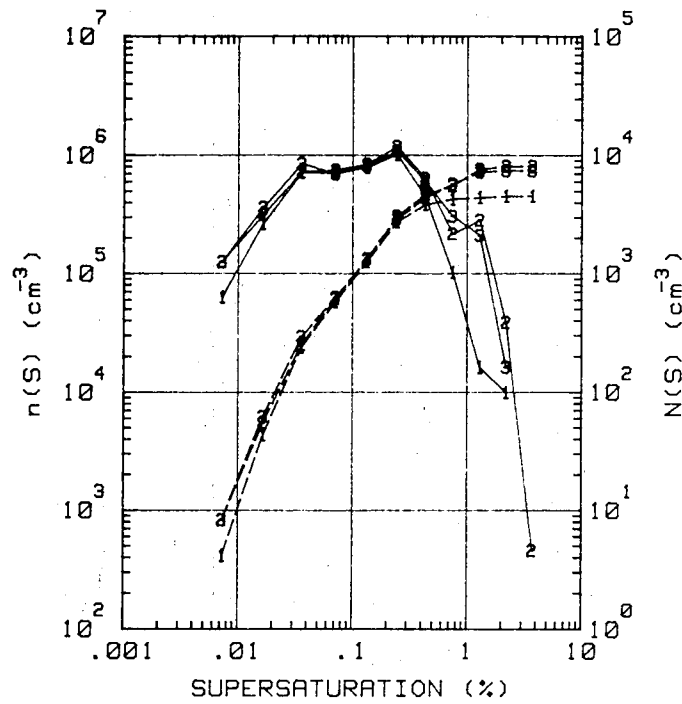


Fig. C8 — Supersaturation spectra for the size distributions of Fig. 22

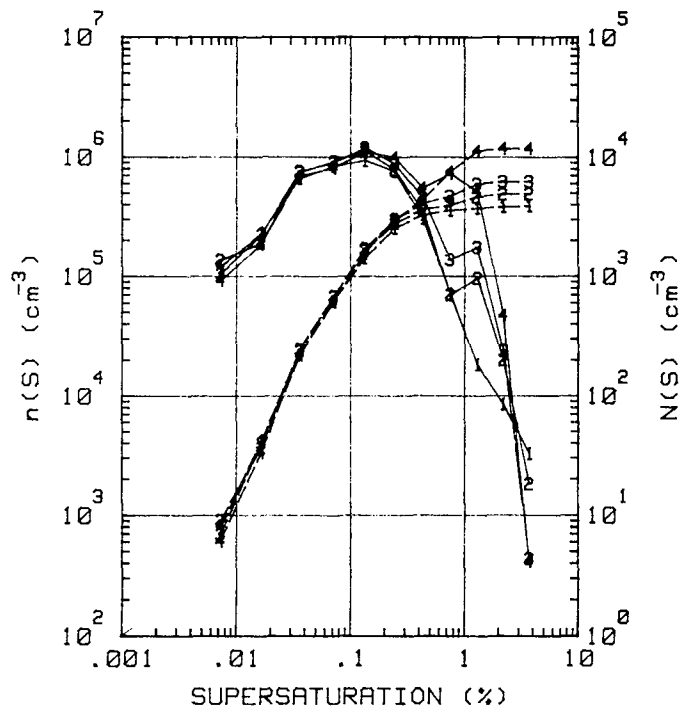


Fig. C9 — Supersaturation spectra of the size distributions of Fig. 23

